Production and characterisation by scanning transmission electron microscopy of size-selected noble metal nanoclusters

by

Dawn Michelle Foster

A thesis submitted to The University of Birmingham for the degree of

Doctor of Philosophy

Nanoscale Physics Research Laboratory

School of Physics and Astronomy

The University of Birmingham

2017

Abstract

In this thesis aberration corrected scanning transmission electron microscopy (ac-STEM) is employed to study the atomic structure of size-selected nanoclusters. The nanoclusters are produced using a magnetron sputtering gas aggregation cluster source with lateral time of flight mass filter, which enables the deposition of high precision samples. For Au nanoclusters, the combination of these techniques is used to determine atomic structure as a function of size, elucidate cluster growth mechanisms, determine the lowest energy structural isomers and investigate control of atomic structure through formation conditions. To further investigate the atomic structure of Au nanoclusters, an in-situ heating holder for the ac-STEM is used to extract a quantitative value for the energy difference between competing structural isomers. A study of surface melting of Au clusters on amorphous-carbon is also presented and the results are discussed with reference to several models for nanoscale melting. Finally, ac-STEM and STEM electron energy loss spectroscopy are used to study the atomic structure and ageing in air of size-selected Ag nanoclusters. It is shown that exposure to air induces a change in both atomic structure and chemical composition.

Acknowledgements

I thank Professor Richard Palmer for the opportunity to work in the NPRL lab and for supervision throughout my experimental work. I also thank Dr Wolfgang Theis for supervision over the past 6 months and for help with corrections to my thesis. I thank Eva Valsami-Jones for supervision and for arranging financial support from the NanoMILE project.

A special thank you to all of my fellow colleagues at NPRL for their friendship and for many useful scientific discussions. In particular, I thank Dr Simon Plant, Ray Hu and Caroline Blackmore for their patient training on the cluster source and electron microscope.

Most importantly, I thank my family for their continued support and encouragement. Especially Andrew for putting up with me over these last few years.

Author's Contribution

All of the work presented in this thesis was carried out by the author under the supervision of Prof Richard Palmer and Dr Wolfgang Theis. Where there is a contribution from a collaborator, it is described at the beginning of the chapter and during the text.

Author's Publications

Metastability of the atomic structures of size-selected gold nanoparticles. Dawn M. Wells, Giulia Rossi, Riccardo Ferrando and Richard E. Palmer. *Nanoscale*, 2015, **7**, 6498

In preparation:

Experimental determination of the energy difference between competing isomers of deposited, size-selected gold nanoclusters. Dawn M. Foster and Richard E. Palmer.

Direct real-space imaging of surface melting in supported, size-selected Au nanoclusters below 5nm. Dawn M. Foster and Richard E. Palmer.

Contents

List of Figures

List of Tables

Abbreviations

HOMO	Highest energy occupied molecular orbital
LUMO	Lowest energy unoccupied molecular orbital
fcc	Face-centered-cubic
Dh	Decahedron
Ih	Icosahedron
HRTEM	High resolution transmission electron microscopy
ac-STEM	Aberration corrected scanning transmission electron microscopy
STM	Scanning tunnelling microscopy
TEM	Transmission electron microscopy
STEM	Scanning transmission electron microscopy
MTP's	Multiply twinned particles
HAADF	High angle annular dark field
UI/A	Unidentified/ amorphous
RGL	Rosato-Guillope-Legrand
EAM	Embedded atom model
MEAM	Modified embedded atom model
MD	Molecular dynamics
DFT	Density functional theory
LNG	Liquid nucleation and growth
FFT	Fast Fourier Transform
T-Oh	Truncated-octahedron

T-Dh	Truncated-decahedron
M-Dh	Marks-decahedron
M-Ih	Mackay-icosahedron
C_s	Spherical aberration
BF	Bright field
ADF	Annular dark field
EDX	Energy-dispersive X-ray spectroscopy
EELS	Electron Energy Loss Spectroscopy
UHV	Ultra high vacuum
LTOF	Lateral time of flight
FWHM	Full width half maximum
a-carbon	Amorphous-carbon
MEMS	Micro-electro-mechanical systems
HWHM	Half width half maximum
p-Ih	Partial-icosahedron

Chapter 1

Introduction and Background

1.1 Nanoclusters Overview

Nanoclusters are aggregates of between 10 and 10^6 constituent atoms or molecules [1] that can be formed from a wide variety of materials, such as metals [2], semiconductors [3], and noble gases [4]. They may consist of a single element or molecule, or of multiple elements, as is the case for bimetallic clusters [5, 6]. Depending on the constituent material, nanoclusters may be bound by ionic bonding (e.g.$(NaCl)_N$), metallic bonding (e.g.Co), covalent bonding (e.g.Si) or by Van der Waals forces (e.g.(Ar_N))[7]. In this thesis, the term nanocluster refers to particles that are well defined (size, composition) and are small enough for size-dependent properties to be apparent. The term nanoparticle is used more generally to describe particles between 1 and 100nm in size. All of the experimental results in this thesis are focused specifically on nanoclusters.

The properties of nanoclusters differ widely from those of the bulk material. Reasons for this include the large surface to volume ratio of clusters, and changes to the HOMO-LUMO gap compared with the bulk material for metals. The gap between the HOMO and the LUMO controls electronic, optical and reactive properties. For individual atoms, electron energy levels are discrete, whereas for a nanocluster the wave functions of the numerous atoms overlap and the energy levels are split (hybridisation), this changes the HOMO-LUMO gap. For bulk material the large

number of atoms means that the split energy levels form quasi-continuous bands. Changing the coating, composition or size of a nanocluster can change the HOMO-LUMO gap and thus its optical properties [8]. For example a blue shift in the absorption peaks with decreasing core size has been reported for glutathione-protected gold nanoclusters [9]. The large surface to volume ratio of nanoclusters can dramatically increase their reactive properties; gold, which is inert in bulk form, is a catalyst in nano-form. The large surface to volume ratio also causes the melting point of many materials to be suppressed and to become highly size dependent at the nanoscale [10] due to the reduced cohesive energy of surface atoms. Contrary to this, it has been discovered that small tin clusters (10-30 atoms respectively) have a melting point higher than the bulk material [11]. The reason for this is unknown, however it is suggested that it may be attributed to differing atomic structure (with higher cohesive energy) compared with the bulk.

Nanoparticles (clusters) have a wide range of uses across multiple disciplines due to their size dependent properties. Numerous types of nanoparticles can be used to catalyse reactions [12, 13]; for example Ni-Ga nanoparticles are a catalyst for carbon dioxide reduction to methanol [14] and small gold nanoparticles made from 55 atom clusters have been shown to catalyse the oxidation of styrene by dioxygen [15]. The high biocompatibility of gold nanoparticles has led to their use in a variety of medical and bio applications such as for drug delivery [16] and sensing of biomolecules [17]. In sensing, when the target substance binds to the nanoparticle (or its ligands) there is a detectable change in one of its properties (e.g. plasmon resonance, conductivity, fluorescence). For drug delivery, the drug to be used is attached to the nanoparticle (or its ligands) and its release is stimulated (e.g.by light, pH, etc.) in the targeted area. An example of this is in targeted cancer therapy research [18]. Silver nanoparticles, which have antibacterial properties [19], are used in wound dressings and clothing [20], and titanium dioxide nanoparticles can be found in products such as toothpaste and sun cream [21]. As well as direct contact with people (through cosmetics etc.), inevitably a proportion of these nanoparticles

are released into the environment. Consequently, there is a great deal of interest in the potential toxic effects of these nanoparticles on living organisms, plants and the environment [22].

1.1.1 Magic Electronic and Geometric Numbers

Nanoclusters present numerous different structures, both single crystalline (octahedra) and twinned (decahedra and icosahedra). Single crystalline structures consist of a continuous crystal lattice (e.g. face-centred-cubic) across the entire cluster, whereas twinned structures contain multiple orientations of a crystalline lattice. For a given size there are a number of different geometric arrangements (structural isomers) that are possible. The structure that has the lowest energy, the ground state structure, is most favourable at T=0K. However, multiple structures (for a given size) are observed experimentally as a result of kinetic trapping [1] and the appreciable Boltzmann weight at room temperature of multiple structures that lie close to the ground state. Certain sizes, corresponding to either closed geometric or closed electronic shells, are more energetically favourable; these sizes are called magic numbers.

Electronic magic numbers were demonstrated experimentally in 1984 by Knight et al [23]. Peaks in mass spectra of Na clusters were observed at 8, 20, 40, 58 and 92 atoms, this can be seen in figure 1.1. These peaks were explained by electron shell closures. Metallic clusters can be modelled as spheres with positive charge distributed throughout and valence electrons filling electronic shells, closing of electronic shells corresponds to the most stable sizes, called magic numbers. It is most likely that the effect of electronic shell closure will be seen for alkali metals (followed by noble metals) because their valence electrons are weakly bound.[1]

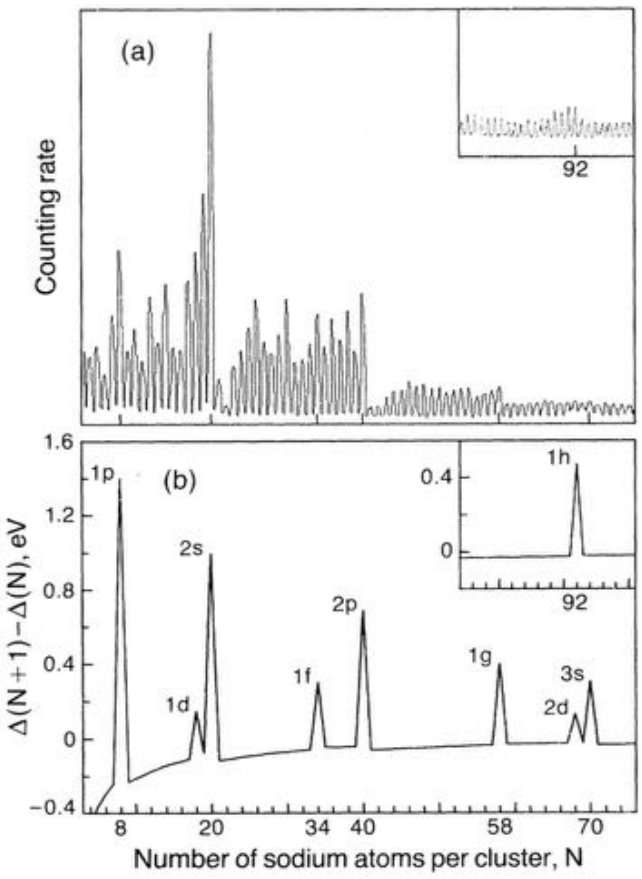

Figure 1.1: a) Mass spectrum of sodium clusters N=4-75. Insert corresponds to N=75-100. b) The calculated change in the electronic energy difference Δ(N+1)-Δ(N), vs N, where Δ(N) is the difference in electronic energy between adjacent clusters. Figure and adapted caption from reference 23.

Mass spectra of sodium clusters produced in a gas aggregation source and ionised using lasers showed that for clusters with more than 2000 atoms certain sizes had higher ionisation potentials, hence were more stable (see figure 1.2) [24]. These sizes corresponded to geometric shell closing of the Mackay icosahedron and cuboctahedron. For smaller sizes of Na clusters it was shown that the magic numbers are still dominated by electronic shell closing. The crossover size from electronic shell magic numbers at small sizes to geometric shell magic numbers at larger sizes varies depending on material [25]. Temperature has also been shown to affect the crossover size between electronic and geometric magic numbers [26]; for higher temperatures, when clusters are liquid, electronic structures are expected to dominate whereas at lower temperatures, when clusters are solid, geometric shell closures are expected to

dominate.

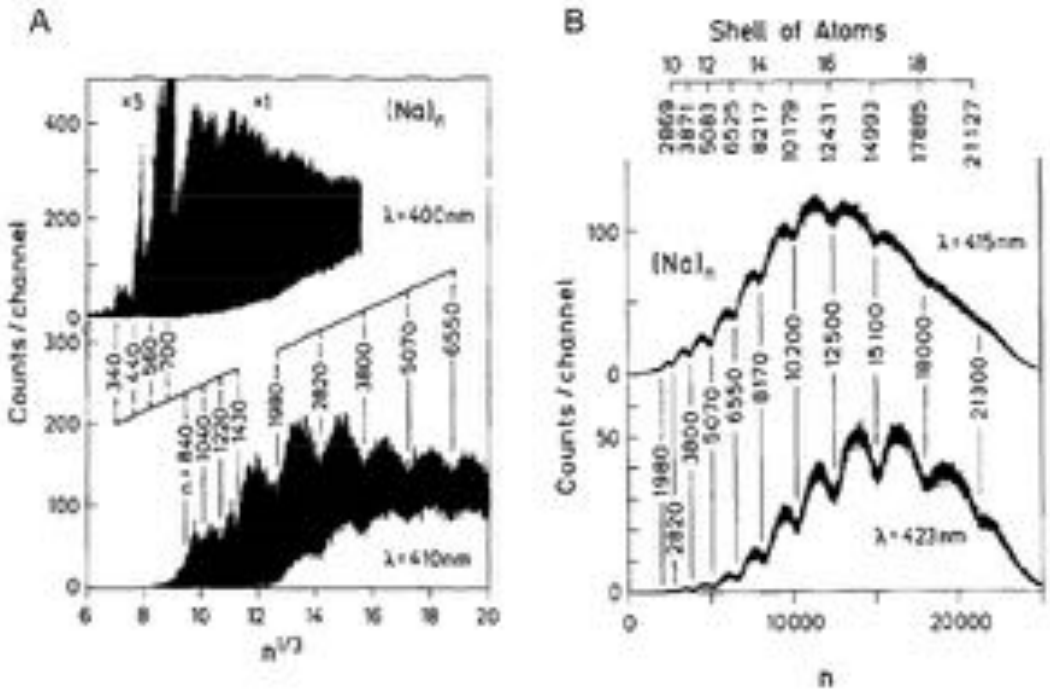

Figure 1.2: a) Mass spectra of Na, clusters photoionized with 400 and 410 nm light. The y axis denotes the total number of counts accumulated in a 40 ns time channel after about 10^5 laser shots. Two sequences of structures are observed at equally spaced intervals on the $n^{1/3}$ scale. b) Averaged mass spectra of Na. clusters photoionized with 415 and 423 nm light. Minima indicated correspond to cluster sizes with higher ionisation potentials - more stable sizes. Adapted figures and caption from reference 24.

1.1.2 Geometric Structures

For single crystalline face-centred-cubic (fcc) clusters, potential geometric structures are the octahedron and truncated octahedron (TO), both of which are shown in figure 1.3. The octahedron consists of two square pyramids sharing a base. The truncated octahedron is an octahedron with cuts at the vertices. The truncated octahedron can be described by the length of the edge of the corresponding complete octahedron, n_l, and the depth of the cut at the vertices in number in layers, n_c. The total number of atoms in any truncated octahedron is given by [1]:

$$N(n_l, n_{cut}) = \frac{2n_l^3 + n_l}{3} - 2n_{cut}^3 - 3n_{cut}^3 - n_{cut}. \quad (1.1)$$

The cuboctahedron (as shown in figure 1.3B) is a specific type of truncated octahedron, for which n_l=2n_{cut}+1 [1].

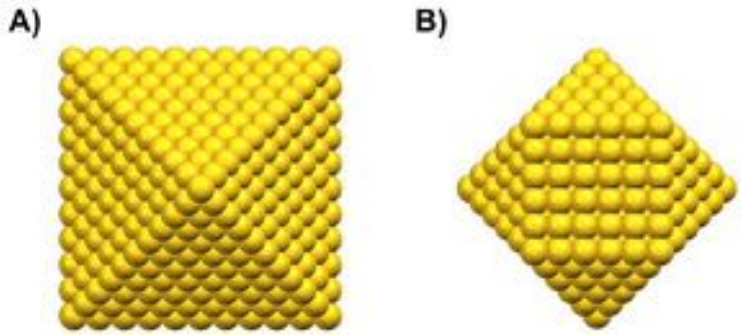

Figure 1.3: A) Octahedron. B) Cuboctahedron, 561 atoms

The decahedron (Dh) is a non-crystalline structure formed of two five-sided pyramids sharing a common base. A decahedron can also be described as multiply twinned fcc because it consists of five fcc tetrahedra.There are two possible truncations that make the cluster more spherical, hence more stable: 1) truncation of the edges of the shared base to expose (100) facets yielding the Ino-decahedron [27], 2) cutting re-entrances between the (100) facets of the Ino-Dh yielding the Marks decahedron [28]. The three decahedron variants are shown in figure 1.4. Decahedra can be described by the lengths of the sides of the (100) facets (m,n), and the number of layers cut by the Marks re-entrance, p. The total number of atoms is given by [1]:

$$N(m,n,p) = (30p^3 - 135p^2 + 207p - 102)/6 + (5m^3 + (30p - 45)m^2$$
$$+(60(p^2 - 3p) + 136)m)/6 + (n(15m^2 + (60p - 75) + 3(10p^2 - 30p) + 66))/6 - 1. \quad (1.2)$$

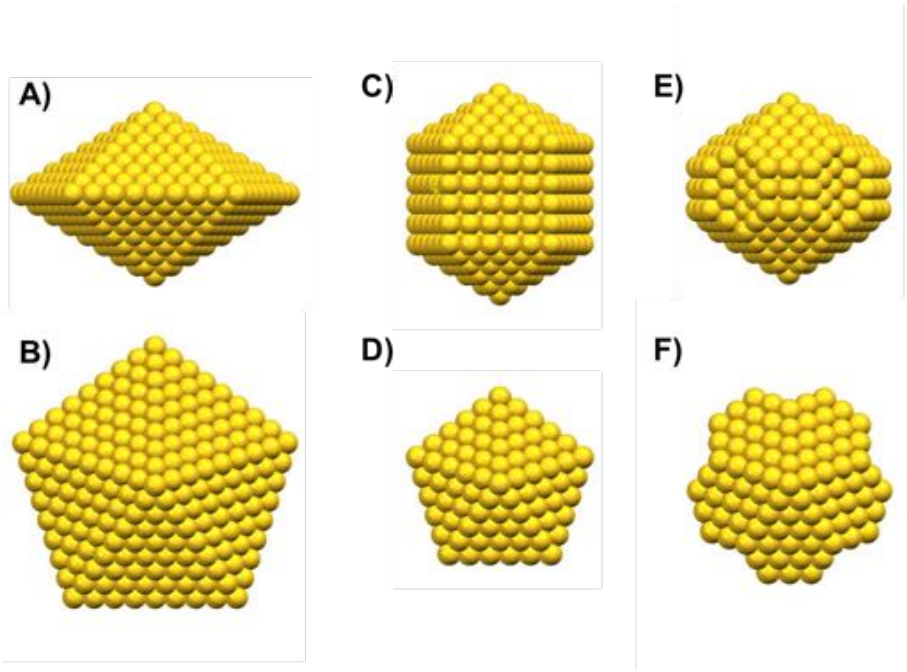

Figure 1.4: A) Decahedron side view, 609 atoms. B) Decahedron front view, 609 atoms. C) Ino-Decahedron side view, 561 atoms. D) Ino-Decahedron front view, 561 atoms. E) Marks-Decahedron side view, 434 atoms. F) Marks-Decahedron front view, 434 atoms.

The other non-crystalline structure is the Mackay icosahedron (Ih), shown in figure 1.5. This structure is formed from 20 fcc tetrahedra, all positioned around a central point, hence it can also be considered a multiply twinned fcc structure. The total number of atoms in a Mackay icosahedron is given by:

$$N(k) = \frac{10}{3}k^3 - 5k^2 + \frac{11}{3}k - 1 \tag{1.3}$$

where k is the number of atomic shells [1]. For the cuboctahedron, icosahedron and Ino-decahedron (with m=n) the series of magic numbers corresponding to closed atomic shells is: 13, 55, 147, 309, 561, 923, ...

For each structural isomer there is a competition between the surface energy and the internal strain. To minimise the surface energy, close-packed facets and a spherical shape are needed, however to minimise the internal strain an fcc bulk-like crystalline structure is required [1]. The truncations discussed above act to lower the surface energy by making the structures more spherical (and in some cases

Figure 1.5: Icosahedron containing 561 atoms

exposing close packed facets). Non-crystalline structures (Ih, Dh) will always have high internal strain but this may be balanced by a lower surface energy compared to single crystalline structures at certain sizes. For metal nanoclusters it is generally expected that the lowest energy structure will be the icosahedron at small sizes, the decahedron at intermediate sizes and fcc at larger sizes [1]. This is because the icosahedron has a large volume contribution (due to the displacement of atoms from the bulk) but a low surface energy, therefore as cluster size is increased the volume contribution increases rapidly making the structure unfavourable. The decahedron has higher surface energy than the icosahedron (less spherical shape) but lower internal strain; hence the volume contribution as size increases is lower compared with the Ih. The fcc structure has lower internal strain than the Ih or the Dh but it has the highest surface energy, this makes it unfavourable at small sizes but most favourable at larger sizes when the volume contribution dominates.

1.2 Atomic Structure of Au Clusters

The use of gold clusters has been reported in multiple applications, including catalysis [15], drug delivery [16], and biological sensing [17]. Determination of the structure of nanoclusters (of different sizes, compositions, formation conditions) is an important step towards understanding, and tuning, their properties. For instance it is thought that establishing the structure of catalyitically active sites is important for understanding how catalysts work and thus designing new, more efficient catalysts [29]. Indeed, new catalysts for H_2O_2 production have been designed and synthesised

based on an understanding of the structure at the active site [30].

All cases discussed below are for bare (not ligated) clusters that are freestanding or on a carbon support - for which the interaction with the cluster is low. Another area of study is that of Au clusters on different supports, Au clusters on metal oxides are catalyst systems and it is important to understand the interface between the support and the cluster to understand the active site [31]. Similarly, the study of the structure of ligated clusters is an import field of research because of their use in catalysis [32] and bio-applications [16, 17, 33, 34]. These topics will not be discussed further here - the report will concentrate on freestanding clusters and clusters deposited on carbon - the subject of results presented in this thesis.

1.2.1 Experimental Studies

The atomic structure of nanoclusters can be determined by trapped ion electron diffraction [35], scanning tunnelling microscopy (STM) [36], HRTEM and ac-STEM. The advantage of trapped ion electron diffraction is that the structure of free clusters can be investigated without any possible distortion that may be caused by a substrate. However, this method is limited by the size range of clusters that can be trapped and also looks at the entire collection of cluster ions (10^5) meaning that if multiple structural isomers exist, or if structures that are not predicted by models exist, they may not be recognised. STM with a Cl functionalised tip can be used to determine the structure of individual clusters and also to gather information on electrical properties [36]. The disadvantage of this method is that the clusters must be supported on a conducting or semiconducting substrate and this may disrupt the cluster's structure. Also the method is very time consuming in comparison to TEM making statistical analysis unrealistic. The most direct method for determining atomic structure is by TEM (either HRTEM or ac-STEM). The limitations of this method are that it requires the nanoclusters to be deposited on a surface and the electron beam can cause damage to the sample. However, the method allows atomic resolution imaging of an extensive range of sizes and materials on an indi-

vidual particle basis. This literature review will concentrate on (S)TEM studies of Au nanoclusters.

The first direct measurements of the atomic structure of Au clusters were made in the 1960's by Ino et al and Ogawa et al [37, 38, 39] using TEM. Since then there have been many TEM investigations of Au clusters, most of these early studies concentrated only on determining the structures presented by Au clusters that had been produced by evaporation of Au on to an a-carbon substrate [40, 41, 42, 43]. For example in 1991 Borel et al used HRTEM and multislice image simulation to study the structures of Au clusters, and reported that Dh, Ih and multiply twinned particles (MTP's) were observed commonly whilst fcc single crystals were not [42]. Similarly another HRTEM study in 1992 by Yacaman et al reported that Dh clusters matched well with model structures whilst Ih clusters appeared distorted [43]. More recent studies tend to use cluster beam sources to soft land clusters on to a carbon support and concentrate on determining the ground state structure of clusters, size-selected studies, and resolving the atomic structure of ultra-small clusters using aberration-corrected (S)TEM.

Patil et al [44] performed an experiment designed to determine the ground state structure of Au clusters in the 1-20 nm size range. The clusters were created in a gas aggregation cluster beam source and soft-landed onto carbon films. In some cases the clusters were annealed in the gas phase before deposition. They found that in the samples that had not been annealed, the clusters had multiply twinned polycrystalline structures. In contrast, when they were annealed to a temperature higher than their melting point (1400K for largest sizes), for clusters in the correct orientation, (111) lattice fringes were observed. The smallest size clusters for which fringes could be observed were approximately 400 atoms. Based on this result they concluded that fcc is the ground state structure for Au clusters in this size range. This result has the disadvantage that the atomic structure of small size clusters could not be resolved and off-axis clusters could not be identified. These problems are solved in many of the following studies due to the invention of aberration-corrected

(S)TEM and comparison of images with multislice (S)TEM simulations for different cluster orientations.

In a study by Ajayan et al [45] experimental HRTEM results on the phenomenon of quasi-melting under the electron beam are reported. Small gold particles deposited on MgO were found to 'decouple' from the substrate under electron beam irradiation and to fluctuate continually between different structural motifs. This is called a quasi-molten state. The frequency of fluctuations was found to increase as the interaction with the substrate decreased. Whilst a large amount of energy (high electron beam dose) was needed to initiate the quasimolten state, only a very small amount of energy (low electron beam dose) was needed to maintain the fluctuations. It is even suggested that these fluctuations may continue at room temperature with no additional energy from the electron beam. Based on this result, it is suggested that these small particles become trapped in deep potential energy wells corresponding to stable structures and that intense electron beam irradiation enables them to access a 'shallow potential energy surface' with multiple local minima resulting in a quasimolten state. Van Huis et al [46] also observed this rapid fluctuation between structural motifs in large (5nm, 9nm) colloidal Au particles at elevated temperatures ($\geq$1000K), just below the melting point, noting that the particles are 'hopping between various local minima'.

In a separate study by Doraiswamy et al [47] the mechanism of quasimelting was investigated by HRTEM for Au, Ag and Pd particles. Ag is known to sublimate at temperatures $\geq$600°C and the melting point of Pd is 327.5°C, this was used to set an upper limit on the temperature that the electron beam heats the sample. No melting of Pd, or sublimation of Ag, was observed during electron beam irradiation with the same dose required for quasimelting of Au particles. This demonstrated that the electron beam dose required for observation of quasimelting corresponds to a temperature much lower than the melting point of Au. Hence it is concluded that quasimelting is not a result of the electron beam causing a temporary molten state (through thermal-spikes) and that the energy barriers between structures must be

relatively low.

Koga et al [48, 49] have studied the atomic structure of 3-18nm gold nanoparticles as a function of size and also investigated temperature dependent structural transformations. The gold nanoparticles used in this study were produced using an inert gas aggregation cluster source and deposited onto amorphous carbon. The structures were determined using high-resolution-TEM tilt series; sets of 20 images were taken for each cluster at different angles to obtain 3D structural information. The structures were then identified by comparison with multi-slice simulated images for Ih, Dh and fcc structures.

In the 3-18nm size range it was reported that the majority of structures were Ih, Dh were the second most abundant and there were very few fcc structures observed. The Dh structures had what is described as 'pancake' (truncated pentagonal bipyramid) structure. Neither the icosahedron nor the 'pancake' decahedron is expected to be the lowest energy structure in this size range. It is proposed that these clusters are grown kinetically on small Ih and pancake Dh seeds via shell-by-shell growth and that they cannot overcome the energy barrier to transform into the more stable Marks-Dh (M-Dh) structure. For larger clusters there was a slight decrease in the proportion of Ih and a corresponding increase in the proportion of Dh. This is thought to be a result of the higher absorption cross-section, and hence faster growth, of Dh compared to Ih. [48]

In a separate study by Koga [49], gold nanoclusters were annealed at successively higher temperatures (1173K, 1225K, 1273K) just below their melting points. It was reported that for smaller clusters the Ih transform into Dh and that with higher annealing temperatures larger sized clusters (up to 14nm) transform as well. The clusters were also annealed at 1373K, above the bulk melting point temperature. This process of melting then freezing resulted in the formation of fcc structures, indicating that the energy barrier between fcc and Dh structures in this size range is very high. In the annealed sample, the proportion of fcc structures observed increased with the size of the clusters (from 6-18nm) and the proportion of Dh

structures decreased correspondingly; this result implies that the fcc structures have the lowest energy at larger sizes.

In the TEM studies discussed above the exact size of the clusters in number of atoms was not known, the clusters were not mass selected and only diameters were used to describe the cluster sizes, it has been suggested that the ground state structure can be altered by the addition of just a few atoms [50] and for this reason it is important to know the exact size of the clusters. In the NPRL group the atomic structure of size-selected Au nanoclusters ($\Delta m/m \approx 20$) has been widely reported [51, 52, 53, 54, 55].

In 2008 Li et al demonstrated that the 3D atomic structure of size-selected gold clusters can be determined using HAADF ac-STEM [51]. Au clusters containing 309±6 atoms were produced by a magnetron sputtering gas aggregation cluster beam source. The clusters were then imaged by HAADF STEM. This enabled Z-contrast images of the clusters to be acquired, in which the intensity of an atomic column is proportional to the number of atoms it contains, hence 3D structural information was obtained. The images were then compared with simulated HAADF STEM images of the cuboctahedron, Ino-decahedron and icosahedron to determine the atomic structure. Both the shape of, and the variation in intensity across the imaged clusters was used to compare the experimental and simulated images. It was found that 32% were Ino-decahedral, 25% cuboctahedral, and 8% icosahedral; the remaining proportion was not identified either because they had irregular facets that did not match to a simulated model or there was no ordered arrangement of the atoms. It was reported that during imaging the clusters often rotated under the electron-beam and that occasionally structural transformations were observed. Intensity profiles were taken across the images and compared against the simulations; it was seen that the intensity of the outer atomic columns was lower experimentally than theoretically and an extra shoulder was seen at the edge in all cases. This deviation from the model was attributed to movement of surface atoms on a faster timescale than the image acquisition.

In the same study the intensity of size-selected clusters ranging from 55 atoms to 1500 atoms was also measured and it was found that the relationship between size and intensity is linear in this size range. This confirmed that each atom contributes equally to the electron scattering signal detected and validates the method of using HAADF STEM for determination of 3D atomic structure information in Au clusters with up to 1500 atoms. Indeed, it was later determined that this method is valid for clusters containing up to 6500 atoms [56].

Subsequently, the NPRL group has also reported on the atomic structure of deposited (carbon substrate), size-selected Au clusters containing 20, 55 and 923 atoms [52, 53, 54, 55].

For Au_{20} a tetrahedral structure was reported [52]. However, other lower symmetry structures were seen more frequently. Continuous sequences of images were taken for individual clusters, from these it was seen that the clusters continually transform between different atomic arrangements. Structural changes to a lower energy atomic arrangement were also seen under the electron beam; clusters tended to stabilise with either the tetrahedral arrangement or more commonly a circular structure. In this particular study a low dose was used for imaging ($8.8x10^3$ e^-/Angstrom^2/frame, 13.3x13.3nm field of view) to limit damage to the clusters and it was confirmed (by measuring cluster intensity across images series) that under these condition knock-on-damage did not cause atoms to be sputtered from the clusters.

Similarly, for Au_{55} [53] it was shown that the structures of the clusters fluctuate continually under the e-beam. Predicted chiral structures and amorphous structures were often seen in the image sequences. However, none of the high symmetry fcc, Ih or Dh motifs were observed. To identify the chiral structures multi-slice STEM simulations were performed on predicted chiral geometries at different angles of rotation, creating a 'simulation atlas'. This method is used in several studies [53, 54, 55] and is explained in more detail in chapter 2.

In the case of Au_{923} clusters, Wang et al [54] deliberately induced structural

transformations. Experiments were performed by taking a continuous series of images (at a dose of 2.4×10^4 e^-/Angstrom^2/frame for up to 500 frames, field of view 10.5×10.5nm) of individual Au_{923} clusters and observing changes in the atomic structure. The structures were assigned as Ih, Dh, or fcc by comparison with a simulation atlas for the Au_{923} icosahedron, Ino-decahedron and cuboctahedron as shown in figure 1.6. It was reported that nearly all the Ih (41/42) convert into Dh (29/41) or fcc (12/41), only one case (1/18) of an fcc to Dh transformation was observed and all Dh structures stayed Dh over the 500 frames. Based on the structural transformations, the proposed order of stability for this size is from Dh-fcc-Ih. However it is noted that the preference for the Ih-Dh transitions could be due to the potential energy barrier from Ih-Dh being lower than for Ih-fcc, and that it is not necessarily true that the Dh structure has a lower energy than the fcc. MacArthur et al [57] reported a similar result for large (6-20nm) colloidal gold particles. They found that ex-situ annealing to 100°C and 250°C resulted in an increase in Dh isomers and a corresponding decrease in Ih isomers. Moreover it was found that the transition from Ih to Dh is initiated at ≈100°C.

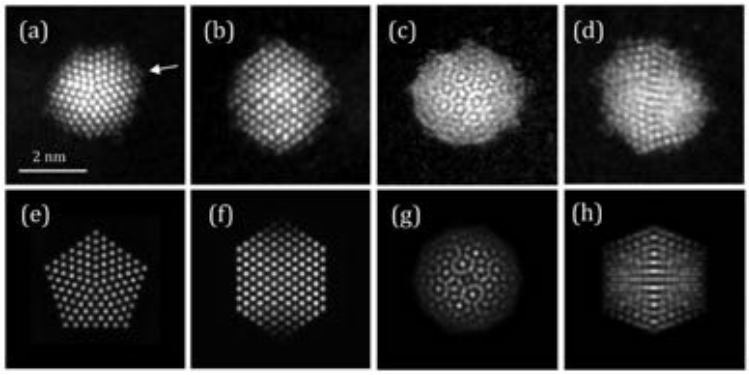

Figure 1.6: Typical HAADF-STEM images of Au_{923} clusters and corresponding simulations. (a)-(d) the HAADF images for (a) a decahedron along a fivefold axis (<110> axis); (b) fcc polyhedron along the <110> axis; (c) icosahedron along a fivefold axis; and (d) icosahedron along a twofold axis (<112> axis), respectively. (e)-(h) the simulated images obtained from the standard atomic models of the Ino-decahedron, cuboctahedron, and icosahedron, respectively. The arrow in (a) marks the edge where no reentrant structure is observed. Figure and caption from reference 54.

The most recent work on Au_{923} [55] has shown that by varying formation conditions, the atomic structure of the nanoclusters can be controlled. The relative proportions of Ih, Dh, fcc and unidentified/amorphous (UI/A) structures were identified (as above) for samples produced with a range of magnetron powers and condensation lengths. In all cases Dh were most commonly observed, followed by fcc with Ih being least abundant in all cases. It was found that as the magnetron power is increased the proportion of Ih increase monotonically and the proportion of Dh decrease. This is explained by the increased density of sputtered material at high magnetron power resulting in rapid growth conditions far from equilibrium; hence Ih structures are kinetically trapped, having grown from small Ih seeds. Similarly, as condensation length is decreased the proportion of Ih increases, this is explained by the increased growth time at long condensation lengths leading to a reduction in kinetic trapping of Ih structures. Both of these results are accounted for by the metastability of the Ih structure at this size, which was shown in the previous Au_{923} study. As before [54] the relationship between the Ih and Dh structure was also seen (i.e. as the Ih portion increased the Dh portion decreased).

Outside of NPRL, Li et al [58] have also used ac-HAADF STEM imaging to obtain the 3D atomic structure of clusters. Ultra-small gold clusters containing 25 atoms (calculated from measuring the HAADF intensity of single Au atoms) were prepared by evaporation of Au onto amorphous carbon films. They used HAADF images of the ultra-small clusters to create basic model structures that were then relaxed by DFT and used to create mulitslice STEM simulations. From a sequence of HAADF STEM images a structural transition (caused by the e-beam irradiation) from a square shape to an elongated shape was observed. By comparing the same images to the multislice simulations they identified that the transition was from a 2D square structure to 3D elongated structure. This example shows how HAADF STEM images can be used to work back to a structure. While this is possible for smaller clusters, it presents a much larger challenge for larger clusters (several hundreds of atoms) for which there would be a huge number of possible atom arrangements.

The above studies show that although static studies of nanoclusters have merit for determining possible low lying isomers, dynamical or temperature dependent experiments are needed to obtain information on the order of stability of structural isomers. Both the study by Plant et al on Au_{923} structure control [55] and the observation of energetically unfavourable structures by Koga et al [48] show that the proportion of structural isomers observed is not necessarily representative of the ground state.

1.2.2 Theoretical Studies

The general trend expected for metal nanoclusters, based on the competition between surface energy and internal strain, is that the Ih will be most stable at small sizes, the Dh at intermediate sizes and fcc structures at larger sizes. This trend is supported by many theoretical studies [59, 60, 61, 62], however the predicted sizes at which these structural transitions occur varies widely and in some cases variations from this trend are reported [50, 51, 62, 63].

Baletto et al [60] calculated the structural crossover sizes for a range of metal nanoclusters by molecular dynamic simulations using both Rosato Guillope and Legrand (RGL) and embedded atom model (EAM) potentials. The general trend for metals from Ih→Dh→fcc with increasing size is reported, although for gold the Ih region is virtually non-existent and the Dh region is also very small meaning that fcc structures are already lowest in energy at 600 atoms. This is explained by the fact that for gold, changing the interatomic spacing (as is the case for the non-crystalline Ih and Dh structures) results in a large increase in energy. For other metals the effect is not so large and as a result the Ih and Dh regions are present up to much larger sizes.

In contradiction to this Barnard et al [59] predicted a wide Ih region, at 250K the Ih was predicted to be the lowest energy structure for clusters < 5nm in diameter, the Dh between 5 and 15 nm and fcc (including fcc twins) >15nm. At 0K the Ih region was reported to be even larger; Ih being the lowest energy structure for

clusters <11nm in diameter, the Dh between 11 and 14nm and fcc structures at >14nm. These calculations were made using a thermodynamic model [64].

Chen et al [63] used Ino's theory [27] to determine the most stable structures at different sizes, however parameters used were determined from the Sutton-Chen potential (rather than using experimental values). They reported that for N<200 the Ih has the lowest energy and for N>200 the truncated octahedron has the lowest energy. This corresponds to a crossover size of 2nm, much lower than the 10nm crossover predicted by Ino's theory. In this study the energy of numerous perfect geometries were minimised to confirm the trend. It was found that for N<500 the Ih is the lowest energy structure, for 500<N<2000 the octahedron, for 2000<N<10000 truncated Dh, truncated octahedra and octahedra are all lowest and for 10000<N<15000 the octahedron and truncated octahedron are lowest. There was not a clear intermediate Dh region, however the energy of the truncated decahedron, although not lowest, is also reported to be very low in the intermediate size ranges.

The melting and freezing behaviour of nanoclusters in the 2-5nm size range was calculated from molecular dynamics simulations (MEAM potential) by Kuo and Clancy [61]. All clusters were initially created as fcc, melted then cooled again. It was found that the clusters transform from fcc to Ih at high temperatures ($\sim$ 100K below melting point). As the temperature is increased further, near to their melting point, the clusters take on a quasi-molten state where the structure fluctuates continuously. The general trend at low temperatures is reported as being from Ih$\rightarrow$Dh$\rightarrow$fcc with increasing size. However, as the temperature is increased Dh and smaller sized fcc structures were found to transform into Ih before melting, and larger fcc transformed into Dh before melting. For freezing the reverse of this behaviour is reported.

In a study on the atomic structure of Au_{309}, Curley et al [65] performed simulations to determine low energy structural isomers for comparison with experimental results. Initially using the Gupta many body potential to determine the energy of perfect Ih, Dh and cuboctahedron (fcc) structures, they found that Ih is most stable,

followed by Dh, then fcc. However, all isomers were found to be within 4meV of each other, meaning that experimentally all are likely to be observed. A global optimisation was then undertaken to determine further low lying isomers in the size range 294-324 atoms; local minima were found for incomplete and distorted Ih structures, and interestingly for size 309 a distorted Ih was found to be more stable than the perfect Ih geometry. The average energy difference between structures in the two lowest energy minima was on average only 0.3meV, this means that experimentally many different distorted structures should be observed.

Goedecker et al [50] used a minima hopping global optimisation method (RGL potential) to determine low energy isomers in Au clusters with <318 atoms. They reported that the addition of just a single atom completely changes the lowest energy atomic structure - this is in contrast to the MD simulations discussed above in which Ih, Dh and fcc regions are predicted. It is also reported that the energy difference between low-lying isomers is very small and that practically this means many different geometries would be observed experimentally at room temperature, not only because of kinetic trapping but also because of their Boltzmann weight at non T=0K temperatures. Additionally for these small sized clusters most of the structures were found to be more complex than the perfect Ih, Dh and octahedral magic number geometries.

Li et al [62] have performed DFT studies on 1.1-3.5nm diameter Au clusters (Au_{55}-Au_{923}). For high symmetry (Ih, Ino-Dh, cuboctahedron) magic number clusters the order of stability is reported to be Ih>Dh>fcc. However, several low symmetry structures were also determined by global optimisation and several of these were lower than their high symmetry counterparts. For example, for cluster sizes >549 atoms lower symmetry fcc-type isomers were more favourable than the perfect Ih and for cluster sizes <561 atoms reconstructed, lower symmetry Ih and Dh structures were lower in energy than the perfect Ih.

Several molecular dynamics studies have been conducted on the freezing of gold nanoclusters. These types of simulation can give insight in to how metastable struc-

tures are produced under experimental conditions. All simulations in references 66-69, reported that a metastable Ih structure is most commonly formed when a liquid gold cluster is frozen. Using the EAM potential Yoon et al [66] reported that for a liquid Au_{561} cluster, crystallisation initiates at the surface, not at the core as would be expected from nucleation theory. They found that five-fold Ih symmetry regions nucleate on the surface, which then acts as a seed for the crystallisation of the core - this is said to be due to the low kinetic barrier to Ih structure at the surface. Similarly Bowles et al [68] found that the surfaces of liquid clusters often have regions similar to (111) Ih facets and this is why Ih structures are favoured upon freezing. Ferrando et al [67] also investigated the effect of the freezing rate on the structures that are formed in 2-4nm Au clusters; they report that at fast cooling rates Ih are preferentially formed but at slower cooling rates there are more Dh, p-Dh and fcc structures. The poly-decahedral structures are formed by the simultaneous nucleation of multiple five-fold axis and are more common at faster freezing rates.

Several factors should be taken in to consideration when comparing experimental data to theoretical studies. 1. Kinetic trapping of structures in experimentally produced clusters meaning that systems are not at equilibrium. 2. The effect of non-zero temperature must be taken into account. Most experiments are performed at room temperature or above (and many theoretical studies at T=0K) meaning that, assuming equilibrium, the Boltzmann weight of lower-lying isomers will be appreciable. This will be particularly important if isomers are in close competition as is reported in many cases (e.g. Dh and fcc). 3. The size distribution of samples - the addition of a few atoms may impact the ground state structure.

1.3 Melting of Nanoclusters

It is well known that the melting point of materials is suppressed at the nanoscale. Generally, this can be explained by the increased surface to volume ratio at the nanoscale in combination with the reduced cohesive energy of surface atoms. In this

section, several models of melting point suppression at the nanoscale are explained and studies on the melting of gold nanoparticles discussed. This section is relevant to results presented in chapter 5, in which the melting of size-selected gold clusters is investigated.

1.3.1 Models of Melting Point Suppression

Pawlow derived the first model of melting point suppression for nanoparticles in 1909 using thermodynamic principles - the triple point model [70]. The model is based on the assumption that at the melting point the chemical potentials of solid and liquid spherical nanoparticles (with the same radius) are equal (μ_s(p,T)=μ_l(p,T)). By expanding the chemical potential at the triple point to the first order (in 1/r), the equation below is obtained for melting point suppression [71]:

$$T_m = T_0 \left(1 - \frac{2V_s}{Lr}\left(\sigma_s - \sigma_l \left(\frac{\rho_s}{\rho_l}\right)^{2/3}\right)\right). \tag{1.4}$$

Where T_m is the suppressed melting temperature, T_0 is the bulk melting

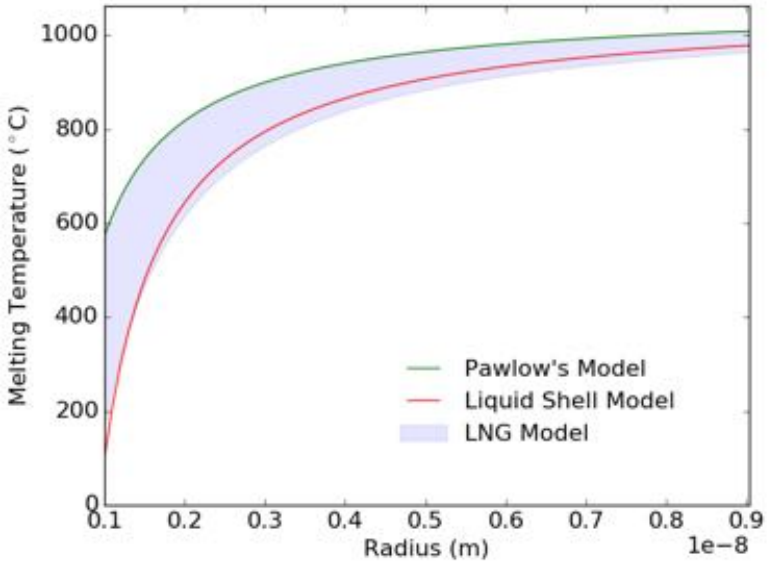

Figure 1.7: Models of melting point suppression. The green line is Pawlow's triple point model, the red line the liquid shell model (0.25nm shell thickness) and the blue region the liquid nucleation and growth model. Table 1.1 shows the parameters used for plotting these models.

Table 1.1: Parameters used to produce figure 1.7

Symbol	Value	Reference
T_0	1336 K	[71]
V_s	$10.7109\times10^{-6}m^3$/mol	[70]
L	12362 J/mol	[71]
σ_s	1.4 J/m^2	[71]
σ_l	1.13 J/m^2	[71]
σ_{sl}	σ_s- σ_l	[71]
ρ_s	18400 kg/m^3	[71]
ρ_l	17280 kg/m^3	[71]

temperature, V_s is the molar volume of the solid, L is the molar latent heat, r is the particle radius, $\sigma_{s/l}$ is the surface tension of the solid and liquid particle respectively and $\rho_{s/l}$ is the mass density of the solid and liquid respectively. The full derivation can be found in reference [1]. This model is plotted in figure 1.7, the result is a 1/r dependence on the melting point.

The liquid shell model was devised by Reiss and Wilson in 1948 [72] and reworked by Hanzen [73] and Sambles [74]. Similarly to Pawlow's model it is based on thermodynamics. The model assumes that melting is initiated at the surface and that close to the melting point a liquid shell, of thickness t, exists around the edge of the particle. The thickness of the liquid shell is independent of temperature. A schematic of this is shown in figure 1.8. The melting point for a particle of radius r and liquid shell thickness t is given by: [71]

$$T_m = T_0\left(1-\frac{2V_s}{L}\left(\frac{\sigma_{sl}}{r-t}+\frac{\sigma_l}{r}\left(1-\left(\frac{\rho_s}{\rho_l}\right)^{2/3}\right)\right)\right) \tag{1.5}$$

where σ_{sl} is σ_s-σ_l and t is the thickness of the liquid shell. The $\frac{1}{r-t}$ term in liquid shell model results in lower melting temperatures for smaller particles compared with Pawlow's model (greater melting point suppression). Equation 1.5 is plotted

in figure 1.7 for a shell thickness of 0.25nm. Figure 1.9 shows the effect of increasing the shell thickness.

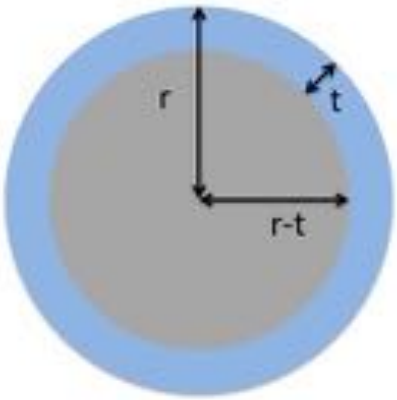

Figure 1.8: A schematic of the liquid shell model. The solid core, radius r-t, is shown in grey, and the liquid shell, thickness t, is shown in blue.

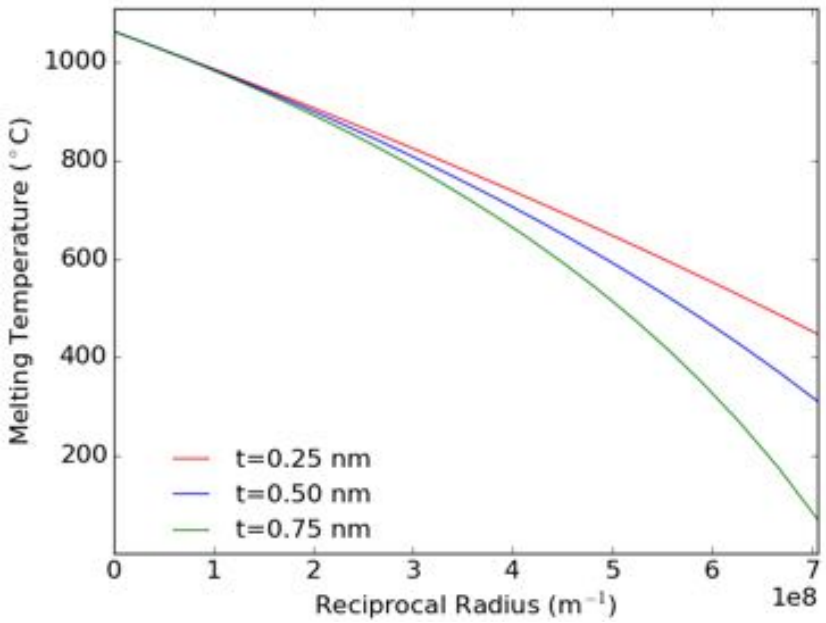

Figure 1.9: The liquid shell model is plotted for three different shell thicknesses: 0.25nm, 0.5nm and 0.75nm.

The liquid nucleation and growth model is a thermodynamic model based on nucleation theory that also provides an explanation for the process of melting. In this model the liquid nucleates on the surface of the particle and spreads inwards

over time, until, at a certain solid core radius, the particle completely melts [70]. Couchman and Jesser [75] determined a lower boundary on the melting temperature by considering that the Helmholz free energy of solid and liquid particles must be equal for melting to occur. The lower boundary was given by:

$$T_m = T_0 \left(1 - \frac{3}{L}\left(\frac{V_s\sigma_s}{r_s} - \frac{V_l\sigma_l}{r_l}\right)\right) \tag{1.6}$$

where $V_{s/l}$ is the molar volume of the solid/ liquid and $r_{s/l}$ is radius of the solid/liquid particle. Assuming the radii of the solid and liquid particles are equal and that the difference between V_m and V_s is also negligible, equation 1.7 is obtained [70].

$$T_m = T_0 \left(1 - \frac{3\sigma_{sl}V_s}{Lr}\right). \tag{1.7}$$

At the upper limit a critical core radius, r_c, exists; for a core radius r_c the criterion that the chemical potential of the solid and liquid particles are equal is met and therefore the particle must be molten. The critical radius is given by [70]:

$$r_c = \frac{2\sigma_{sl}V_sT_0}{L(T_0 - T)}. \tag{1.8}$$

The upper boundary is given by Pawlow's model (considering μ(s)=μ(l)). According to this theory the particle may melt at any point between the lower and upper boundaries, but melting becomes more probable as the upper boundary is approached. The melting region predicted by the liquid nucleation and growth model is shown in fig 1.7.

1.3.2 Melting of Au Nanoparticles

Sambles performed an electron microscope study of the melting temperature of 5-50nm Au nanoparticles by measuring their evaporation rates [76]. For particles in the temperature range 1150-1300K, two regions with different evaporation rates were observed. The change in evaporation rate was used to determine the melting temperature of the particle. Sambles experimental results are shown in figure 1.10.

In 1976 Buffat and Borel furthered the experimental results of Sambles by performing scanning electron diffraction experiments to determine the melting points of Au particles with diameters of 2-25nm [10]. They used a heating stage in an electron diffractometer and measured the diffracted intensity of the (220) ring until it was no longer identifiable (using loss of atomic lattice structure as the indicator for melting). The size distribution of the sample was then measured using HRTEM. Quantitative analysis of the diffraction ring intensities alongside the measured size distribution enabled the melting point to be determined for a given particle diameter. Their experimental results are shown in figure 1.11. A comparison was made with the second order approximation of the triple point model and the liquid shell model (see section 1.3.1 for model details), both of which provided a good fit to the data. In the case of the liquid shell model a shell thickness of 0.6nm was optimal.

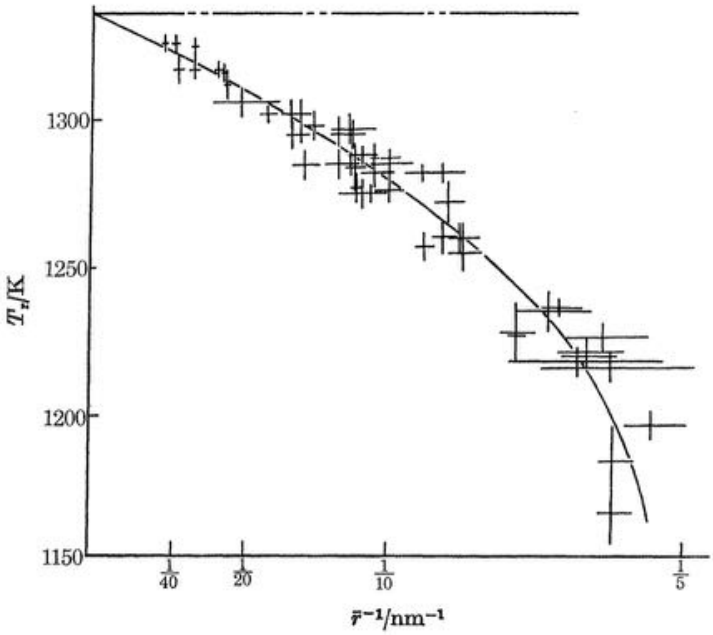

Figure 1.10: Sambles' experimental data of gold particle melting. Variation of the melting temperature with the reciprocal radius for gold particles, determined by measuring the change in evaporation rate. Figure and adapted caption from reference 76.

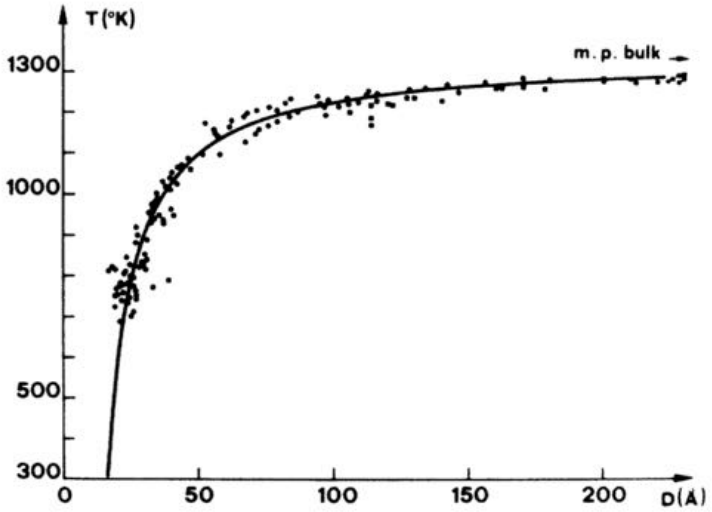

Figure 1.11: Buffat and Borel's experimental data of gold particle melting. Experimental and theoretical values of the melting-point temperature of gold particles determined from diffraction: circles, present work; squares, Sambles; the solid line results from a least-squares fit to the second-order relations of the triple point model, using the experimental data and an estimated value of the Debye-Waller factor. Figure and adapted caption from reference 10.

Castro et al [77] used the change in field emission current of a cluster during heating to determine its melting point. Size-controlled clusters were deposited on to tungsten field emitters and the field emissions of individual clusters were measured as the temperature was increased. At a temperature just below the bulk melting point, there was a sudden change in the field emission current that was interpreted to be due to a sudden shape change caused by the melting of the particle. A dependence on the melting temperature with size was reported for particles with diameters greater then 2nm.

In section 1.2.1 a study by Koga et al [49] was discussed in which the effect of annealing on the atomic structure of gold nanoparticles was investigated. They found that Dh-fcc transitions were only observed when the particles were heated above their melting point. This property was used to determine the melting point of two different sizes by observing the lowest temperature that Dh-fcc transitions were observed for particles of that size. Figure 1.12 shows their results plotted alongside Pawlow's model, the liquid shell model and several molecular dynamics calculations

of Au nanoparticle melting (their measured temperature for Ih-Dh transitions is also shown).

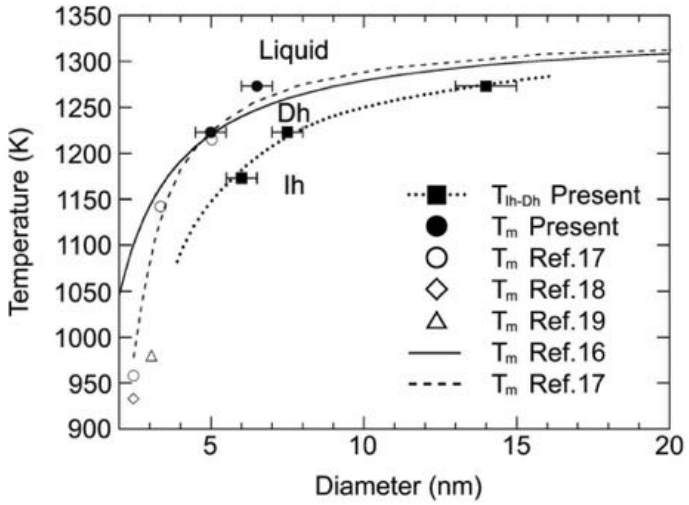

Figure 1.12: A size-temperature structural stability diagram of Ih gold nanoparticles. Melting points (T_m) and Ih-to-Dh transition points (T_{Ih-Dh}) determined in this study are denoted by solid squares (with dashed line fit) and solid circles, respectively. The solid and dashed curves are melting temperatures predicted by Pawlow's theory [78] and the liquid shell model [71]], respectively. Melting points by previous simulation works are plotted by circles [71]], diamonds [79], and triangles [80], where each value is normalised by the bulk melting temperature. Figure and adapted caption from reference 49.

The development of in-situ heating holders for (S)TEM has enabled direct imaging of nanoparticle melting, with atomic resolution. Lee et al [81] used a high temperature holder alongside HRTEM to directly observe melting point suppression in Au. An 8nm Au particle on graphite was heated to 1100K and imaged whilst the particle size gradually decreased. Originally the particle was a single crystal (fcc), when the size of the particle decreased to 5nm a transition to liquid (loss of atomic structures) was observed. This process can be seen in figure 1.13. The measured melting temperature of 1100K for a 5nm Au particle was reported to be in good agreement with previous experimental studies by Buffat and Borel and Sambles.

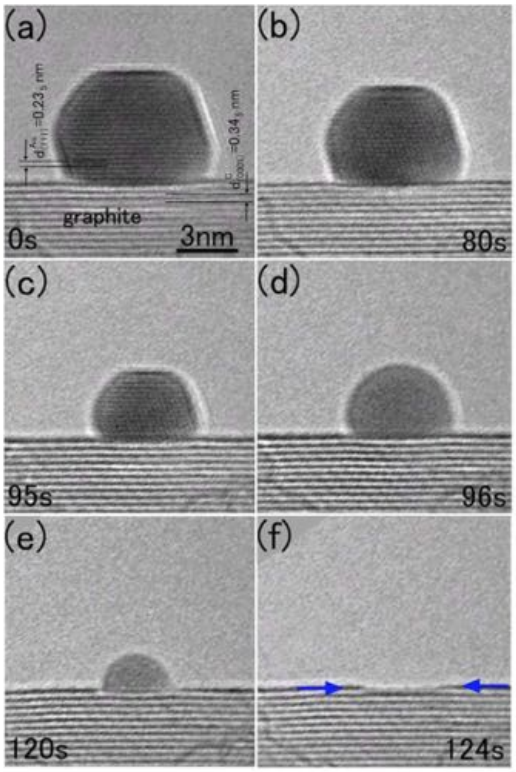

Figure 1.13: A typical example showing successive stages of diminution of a Au particle on a graphite substrate maintained at 1100 K. The numbers inserted in each micrograph indicate relative times in seconds. During the diminution, a crystalline-to-liquid phase transition (i.e., melting) occurred at the particle size of approximately 5nm (d). Figure and caption from reference 80.

Marijn et al [46] reported a similar result using an in-situ heating holder in the TEM. They found that by oscillating the temperature of a 5.5nm Au particle between 990 K and 1000 K, the particle melted and recrystallized repeatedly. A study by the same group [82] investigated the effect of high temperature on the surface of Au nanoparticles, giving some insight into the mechanism of melting. It was reported that a 10nm Dh particle showed loss of atomic structure around the edges at 600°C and loss of atomic structure in half the particle at 700°C. For larger particles (20-30nm) at high temperatures (>600°C) amorphous regions were also observed at the surface, which were attributed to the formation of liquid regions and the coexistence of solid and liquid phases.

There are numerous molecular dynamics simulations of Au nanocluster melting [59, 61, 71, 79, 80, 83, 84, 85, 86, 87, 88, 89]. Several of these studies [80, 84, 86,

88, 89] have calculated melting temperatures for specific cluster sizes, these results are plotted in figure 1.14. The general trend of melting point suppression can be seen, however different studies predict a different degree of suppression. As well as size, atomic structure has also been predicted to play a role in cluster melting; Chen et al [84] calculated that for a gold cluster with 309 atoms, the Octahedron will melt at 635 K, the decahedron at 646 K and the Ih at 647 K. They suggest that the Ih melts at the highest temperature because it's energy is lowered by surface reconstruction prior to melting. In this study surface premelting is also discovered for the Octahedron and decahedron Au_{309} clusters before complete (core) melting.

More generally, surface melting (sometimes referred to as premelting) is a widely predicted phenomenon in theoretical studies [59, 80, 83, 86, 88, 89]. For example, Lewis et al [86] observed that for Au clusters with diameters of <3nm, melting initiates at the surface and spread inwards. Similarly, Shim et al [88] reported that the surface atoms in Au clusters (1.6-6nm in diameter) premelt before complete (core) melting. However, not all studies observe premelting [61, 79, 84]. Cleveland et al [85, 85] did not observe the formation of a liquid layer prior to melting, instead structural transformation to an icosahedron was reported before complete melting. Kuo et al [61] also report structural transformation to Ih, followed by a quasimolten state prior to melting. Whilst in the quasimolten state the clusters are reported to continually transform between different structural isomers. Size dependence of surface melting as a mechanism has also been published. Ercolessi et al [80] found that for particles with N>350 atoms a liquid shell formed prior to melting, whereas in smaller particles (N=100-350 atoms) no liquid shell was formed. Wang et al [89] reported a similar effect; the formation of a liquid shell (premelting) was observed for a cluster with N=7164 atoms, but not for a cluster with N=456 atoms, which only formed a partial liquid surface layer.

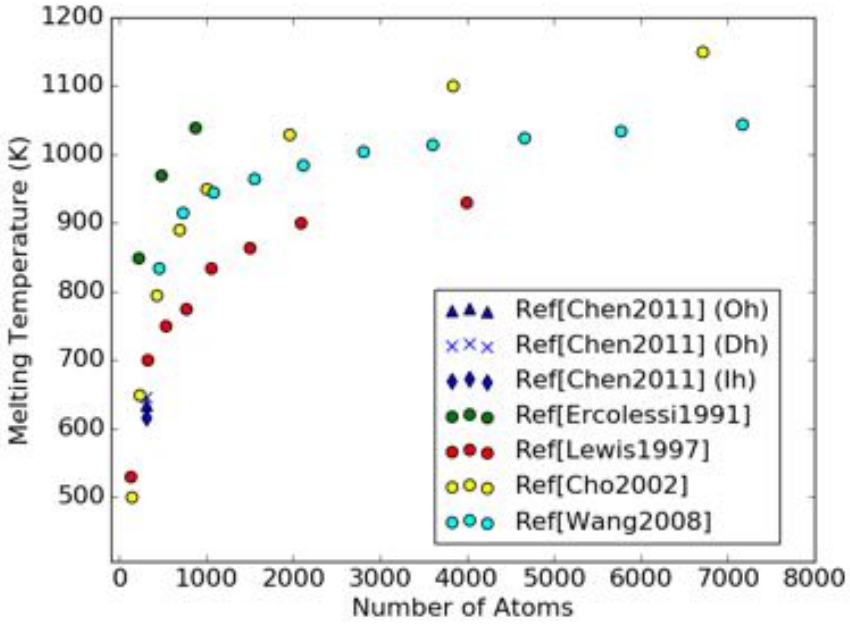

Figure 1.14: Molecular dynamic simulations results. The calculated melting temperature is plotted versus the number of atoms. Where a specific atomic structure is investigated, it is stated in the figure legend. Data reproduced from references 79, 83, 85, 87 and 88 .

The majority of theoretical studies concentrate on calculations of free Au clusters. However, the majority of experimental studies, in particular (S)TEM studies, are of Au clusters supported on a surface. Therefore, it is important to consider the effect of the surface to be able to interpret experimental results. Molecular dynamics simulations performed by Kuo et al [61] found that the addition of a silicon substrate improved the stability of clusters at high temperature, stopping the cluster from forming a quasiliquid state. Lee et al [87] investigated the effect of a graphite, alumina and tungsten substrate on melting, using a thermodynamic model. They found that for Au clusters on a graphite or alumina substrate the melting temperature was hardly altered compared to that an unsupported cluster, whereas on a tungsten substrate the melting temperature was much higher.

1.4 Atomic Structure of Ag Nanoclusters

There is a great deal of interest in the toxicity of Ag nanoparticles, partially due to their abundant use as an antibacterial. The atomic structure and stability of these nanoparticles may ultimately influence their toxicity; for example, a shape dependence of the toxicity of Ag nanoparticles to human alveolar epithelial cells has been shown [90]. Another area of research for which atomic structure is expected to be important is catalysis. Ag nanoparticles are catalysts for ethylene expoxidation and it has be shown that their catalytic activity is dependent on both size and shape [91]. Ethylene expoxidation produces ethylene oxide which is used as an intermediate to produce many other chemicals, for example antifreeze. In regard to shape dependence, the packing of surface facets was considered to be a key factor, highlighting the importance of an understanding of atomic structure.

In this section, only results for bare Ag clusters that are free or supported by carbon will be discussed. This is for comparison with the experimental results presented in chapter 6.

1.4.1 Experimental Studies

Reinhard et al [92] studied the atomic structure of Ag clusters produced in a gas aggregation cluster beam source by performing electron diffraction experiments on the cluster beam. (HR)TEM was also used to determine the size distributions of the clusters. The results show the presence of large Ih clusters that are not expected to be energetically favourable. This is explained in terms of cluster growth in the cluster beam source; large clusters were formed far from the evaporation source where there was a decrease in the temperature, this led to rapid growth of the clusters, hence trapping (or freezing) of metastable icosahedra. It was also found that the large Ih are distorted in contrast to a perfect Mackay icosahedron. Formation parameters in the gas aggregation source were varied and the result on the atomic structure of the clusters was determined. Higher evaporation temperatures resulted in more fcc (expected to be low energy) structures. This is explained by the fact that at higher

temperatures, larger clusters also have enough energy to transform to lower energy fcc structures.

Trapped ion electron diffraction was used by Schooss et al [93] to determine the atomic structure of Ag_{55} cluster ions. The clusters were produced in a magnetron sputtering gas aggregation source and trapped in a quadrupole ion trap for electron diffraction experiments. Potential low energy structures (the cuboctahedron, truncated, decahedron and mackay icosahedron) were optimized using DFT and used for comparison with the experimental results. It was found that for Ag_{55+} clusters the structure was the Mackay Icosahedron and for Ag_{55-} clusters a Jahn-Teller distorted icosahedron.

Barke et al [94] used soft x-ray free electron laser pulses to obtain single shot wide angle scattering diffraction patterns of individual Ag particles. The Ag particles were produced with a magnetron sputtering gas aggregation cluster beam source and diffraction patterns for individual particles in the beam were collected as the nanoparticle beam experienced a perpendicular free electron laser photon beam. The nanoparticle geometries were then identified by comparison with simulated diffraction patterns for different geometries. They found truncated octahedra, icosahedra, decahedra and flat hexagonal structures for particles 10's of nanometers in diameter. The presence of large ($\approx$100nm) metastable (Ih, flat hexagonal, Dh) structures in the beam is noted and it suggested that this might be due to growth on smaller seed structures.

FFT analysis of HRTEM images was used by Gracia-Pinilla et al [95] to determine to atomic structure of size-controlled silver clusters. The Ag clusters were produced in a magnetron sputtering, gas aggregation cluster beam source, size-selected, and soft-landed (<0.1ev/atom) to preserve their structure. They found that for 3.7-5.5 nm clusters, the structures were either Ih or Dh and for 1.3 and 2.5 nm clusters the structure was crystalline. The presence of Ih structures is explained by small Ih clusters acting as seeds for growth of larger clusters.

Volk et al [96] found that, similarly to in gas aggregation sources, kinetics (growth

rate) determines the proportion of atomic structures observed for Ag clusters produced in superfluid helium droplets. Ag clusters were grown in superfluid helium droplets and deposited on to amorphous carbon films for HRTEM imaging. The atomic structure of the clusters was determined by comparison with simulated fcc, Dh and Ih structures. The size distribution of the clusters was also determined, and fractionated according to the structural assignments. Their results are shown in figure 1.15.

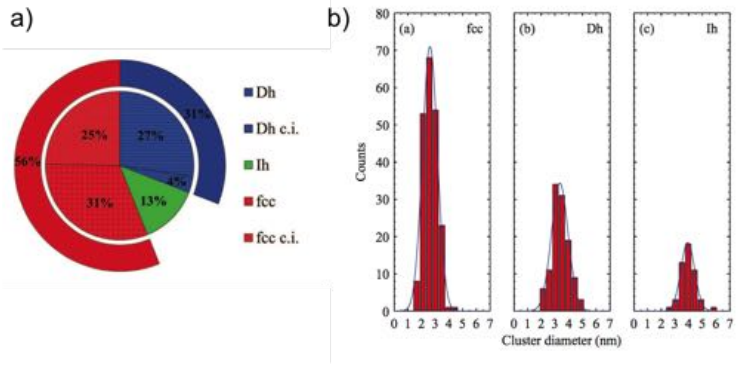

Figure 1.15: a) Relative abundances of the observed cluster morphologies. Fractions labelled with c.i. in the legend belong to clusters which were subject to deeper investigation before being classified. b) Histograms of cluster diameters with fitted Gaussian curves for (a) fcc ($\bar{d}$ = 2.62(5) nm, n≈550 atoms), (b) Dh ($\bar{d}$ = 3.34(7) nm, n≈1150 atoms), and (c) Ih clusters ($\bar{d}$ = 3.93(2) nm, n≈1870 atoms).Figure and adapted caption from reference 95 .

The Ih clusters had the largest mean diameter, Dh intermediate and fcc smallest. This is in contradiction to what would be expected based on energetics, it is attributed to the low temperature formation conditions and fast cooling rates. It is suggested that for small clusters the addition of an atom greatly increases its temperature so it can transform to a low energy structure (Ih for small sizes, Dh slightly larger), once a certain size is reached the cluster no longer has enough energy to transform between structures and the cluster grow on these Ih and Dh seeds. It was also reported that molecular dynamics simulations show that small Ag clusters may transform to fcc structures upon deposition, which explains the abundance of fcc structures at small sizes.

1.4.2 Theoretical Studies

Baletto et al [60] investigated the general trend of structure vs size in Ag clusters containing up to 40,000 atoms. The RGL potential was used to calculate the energies of truncated-octahedra, truncated-decahedra and icosahedra for clusters up to 40,000 atoms and the EAM potential was then used to check the validity of structural crossover sizes for clusters with up to 1000 atoms. Figure 1.16 shows the excess energy divided by the number of surface atoms (Δ) for different cluster structures, plotted against the number of atoms. For the RGL potential it was found that the Ih is lowest, and decreasing, in energy up to 147 atoms, the Dh is lowest between 300 and 20,000 atoms and fcc structures are most stable at larger sizes. This result was confirmed by comparison with the Ih-Dh crossover size calculated using the EAM potential.

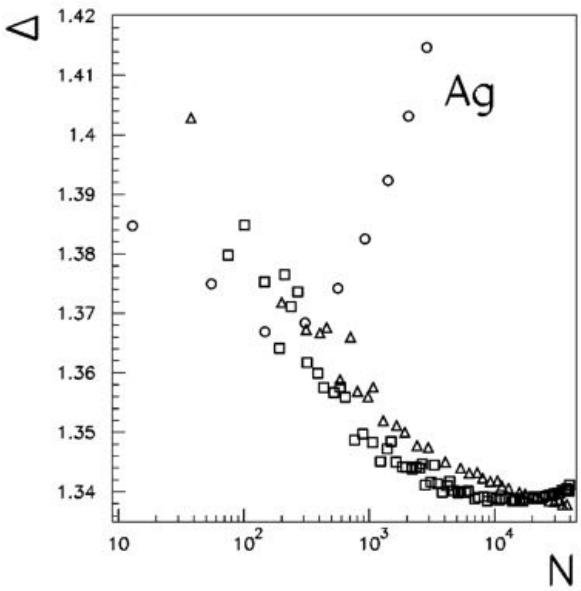

Figure 1.16: The quantity Δ=(E_{tot}-NE_{coh})/$N^{2/3}$ as a function of the size N, calculated by means of RGL potentials for silver clusters. Circles, squares, and triangles refer to icosahedra, decahedra, and truncated octahedra, respectively. Figure and caption from reference 60.

The general trend of structure vs size for Ag clusters was also investigated by Wang et al [63]. Their results are shown in figure 1.17. Analytical calculations of cluster energies were performed using Ino's theory, but with parameters determined

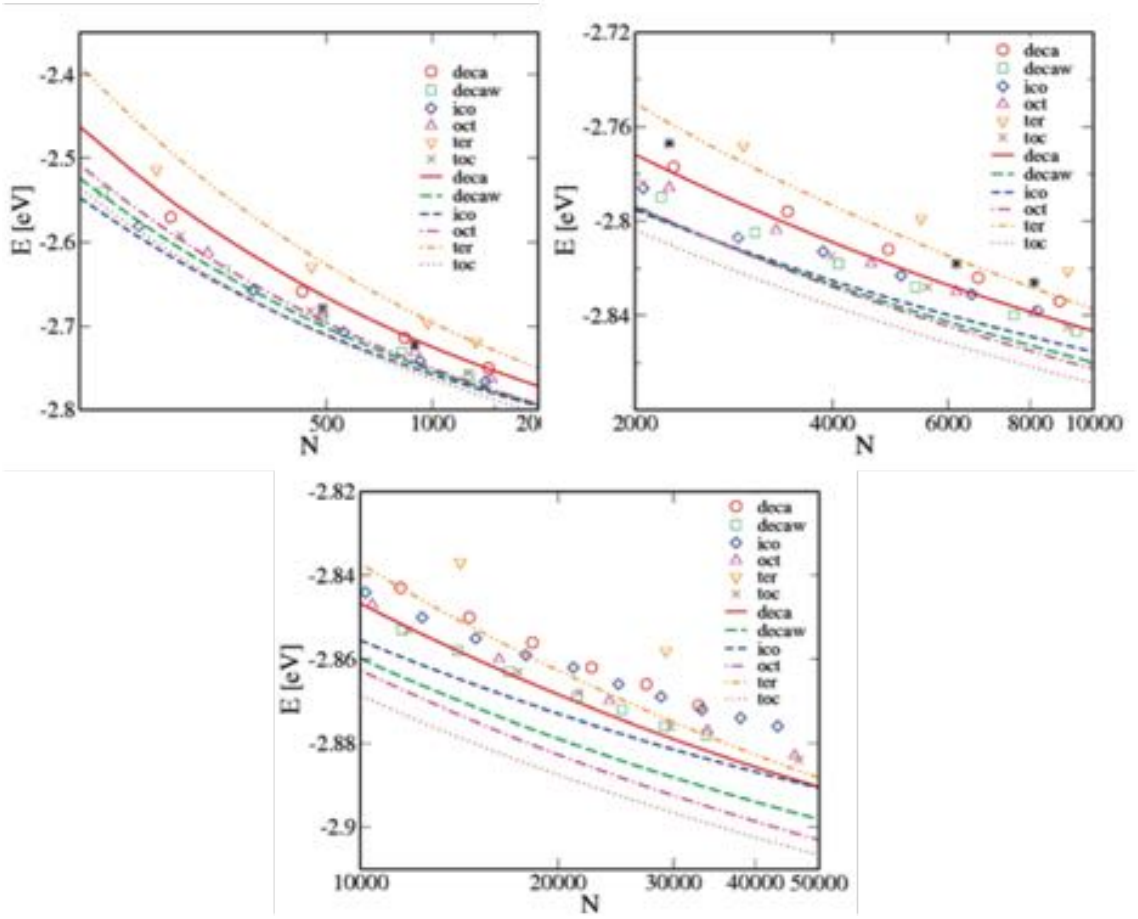

Figure 1.17: Average potential energies per atom for different structures of Ag nanoparticles with N< 2000 (left), 2000<N<10000 (right), and 10000<N<50 000 (bottom), calculated with the Sutton-Chen potential. Analytical results calculated with Ino's theory are plotted in lines: red solid, decahedron; green dashed, truncated decahedron; blue short dashed, icosahedron; magenta dot dashed, octahedron; orange double dot dashed, tetrahedron; grey dot, truncated octahedron. Those for perfect structures are shown in symbols: circle, decahedron; square, truncated decahedron; diamond, icosahedron; triangle up, octahedron; triangle down, tetrahedron; cross, truncated octahedron. Potential energies per atom at T=100 K after simulated annealing are shown in black stars. Adapted figure and caption from reference 63 .

using the Sutton-Chen potential. From this analysis it was found that the Ih was lowest in energy for clusters containing less than 300 atoms and the truncated-octahedron was lowest for sizes greater than 300 atoms. The energy of perfect geometric structures (Oh, Dh, Ih,T-Oh,T-Dh, tetrahedron) was also calculated by performing energy minimisation using the Sutton-Chen potential. It was found that

the Ih is lowest in energy for sizes up to 3000 atoms, the truncated-Dh for sizes between 3000 and 30,000 atoms and the truncated-Oh for sizes greater than 30,000 atoms. These results showed that the assumptions made when using Ino's theory led to inaccurate results for smaller cluster sizes. The results reported by Wang et al predict very different crossover sizes to those of Baletto et al, which is likely due to the different choice of potential. However both predict that Ih is stable at small sizes, Dh at intermediate and fcc at larger sizes.

For smaller sized clusters there have been several molecular dynamic studies that search for low energy, global minima structures [97, 98, 99, 100, 101, 102]. The majority of studies report that in general, at very small sizes, the icosahedron is lowest in energy and the decahedron lowest at intermediate sizes. For example, Doye et al [98] reported that the most stable structures are 13 and 55 atom Mackay-icosahedra, whilst generally Ih are most stable up to 63 atoms, and Dh between 63 and 80 atoms. Similarly, Angulo et al [101] reported that for Ag clusters ranging in size from 7 to 561 atoms the majority of clusters have Dh and Ih structures; principally Ih at small sizes and Dh at larger sizes. For magic sizes (13, 55, 147, 309 and 561), they found that the Ih is always lowest in energy.

References 97-99 show very good agreement; all predict a truncated octahedral global minima for Ag_{38}, a Mackay-icosahedron global minima at Ag_{55} and a Marks-decahedron global minima for Ag_{75}. Similarly to the result of Angulo, Huang et al [102] found that, for clusters containing 141-310 atoms, the decahedron is the generally the lowest energy structure, with only a few local fcc global minima. However, in contrast the only Ih global minimum was for Ag_{147}.

Ab initio calculations were performed by Jennison et al [97] of Ag_{55}, Ag_{135} and Ag_{140}. For Ag_{55} and Ag_{135} it is reported that Ih is the preferred structure, in agreement with many of the studies above. However, at size 140 an fcc structure was found to be lowest in energy and it is suggested that this represents a crossover size from Ih to fcc.

Molecular dynamic studies of growth and freezing of Ag clusters can give some

insight in to the experimental observation of large Ih and Dh structures that are expected to be unstable. Baletto et al have performed several molecular dynamic simulations relating to the growth and freezing of silver nanoparticles [103, 104, 105]. In a study of the growth of small (<150 atoms) clusters it was reported that a combination of growth conditions and the lowest energy structures contribute to the final structures obtained [103]. The simulations were performed starting with a 7 atom cluster, atoms were added one by one for a range of different deposition rates and temperatures (similar to those in a gas aggregation cluster source) and the resultant structures were investigated. The result of their simulations can be explained with reference to figure 1.18, which shows the excess energy per surface atom of different structures up to 150 atoms. For all temperatures and growth rates

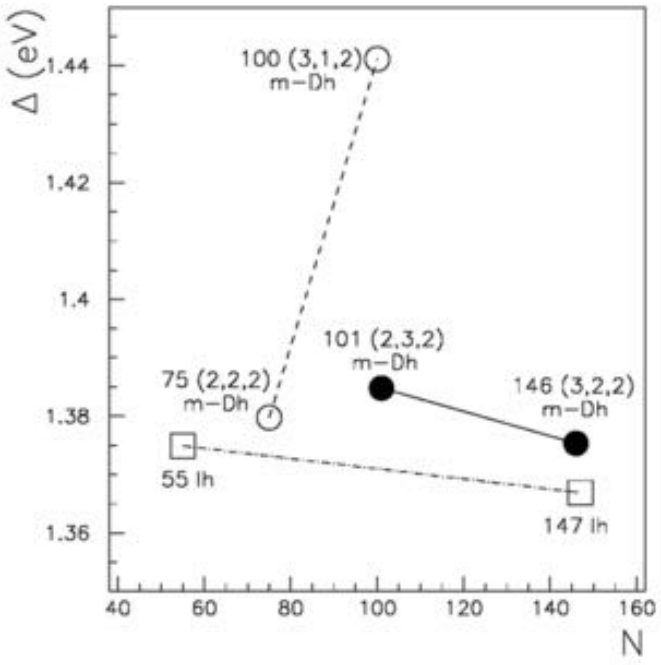

Figure 1.18: Δ, excess energy per surface atom as a function of the cluster size N for some structures corresponding to magic numbers. The squares correspond to Ih structures, and the circles to M-Dh structures. Figure and adapted caption from reference 102.

investigated it was found that the M-Ih at 55 atoms and M-Dh(2,2,2) at 75 atoms is formed. At lower temperatures the 75 atom M-Dh(2,2,2) grows into the similar 100 atom M-Dh(3,1,2). It does not have enough energy to rearrange to the lower energy

101 atom M-Dh(2,3,2). Ih islands grow on the 100 atom M-Dh(3,1,2) and the 147 atom M-Ih is formed. For T=450-550K the cluster has enough energy to rearrange in to the stable 101 atom M-Dh(2,3,2) and from this structure the metastable 146 atom M-Dh(3,2,2) is grown. At even higher temperatures (550-600K) the cluster still has enough energy to rearrange at larger sizes (N=130 atoms) and so the lowest energy structure, the 147 atom M-Ih is obtained.

Similar growth simulations were performed for Ag clusters with up to 600 atoms [104]. In this study the deposition rate was kept constant and the temperature was varied between 350 and 650K. Conditions were chosen to match experimental conditions in gas aggregation cluster sources. It was found that at high temperatures (650K) the growth of clusters follows the low energy structures as they have enough energy to transform, this leads to the growth of energetically favourable fcc structures. At low temperatures (400K), layer-by-layer growth occurs on seed 147-Ih clusters, resulting in the growth of large Ih. At 600K Dh structures are formed by growth of Ih islands on a 147 Ih and rearrangement to form a stable 318 atoms m-Dh. At slightly lower temperatures (450K) another mechanism for the growth of large Ih was found. Island growth on the 146 atom m-Dh leads to the formation of an Ih facet and new 5-fold axis resulting in transformation to an Ih. Because of the low temperature, there is not enough energy for rearrangement to the 318 atom m-Dh. The fact that there are two routes to the growth of large metastable Ih explains why they are seen more frequently than large metastable Dh in experimental studies of Ag clusters produced using a gas aggregation cluster source, see reference 91.

In a later study, Baletto et al [105] report the result of a different growth mechanism: freezing of Ag nanodroplets. Molecular dynamics simulations were performed to determine the structure of Ag clusters formed by the freezing of liquid clusters consisting of N=130-310, 561 and 923 atoms. It was found that for 147 atom clusters, Ih structures form 100% of the time, and generally at small sizes (130-310 atoms), Ih and Dh are likely to be formed. In contrast, at larger sizes Dh and fcc

structures are more likely, with only 10% of Ag_{923} clusters producing Ih. The results of this study do not agree with the experimental results of Reinhard [92] and so it was concluded that in gas aggregation sources clusters do not grow as liquid droplets but from small seed structures.

It has also been shown that landing conditions can alter the final distribution of structures in deposited Ag clusters. Thaler et al [106] performed molecular dynamics simulations of the landing of Ag clusters designed to replicate conditions found in a helium droplet cluster source [96]; the temperature of the clusters was 0.37 K, whilst the substrate temperature was 300 K. They found that upon landing many smaller Ih and Dh clusters (2-3nm) transformed to fcc structures, whilst larger clusters (4nm) were more likely to retain their starting structure. The increase in temperature of the clusters upon landing was a key factor in their rearrangement to fcc structures; for soft landing conditions where the temperature of the cluster increased less, structural transitions were less likely.

In summary, for both Au and Ag nanoclusters the literature supports the general trend of Ih→Dh→fcc with increasing particle size. However, there is little agreement (from experiment or theory) on the crossover sizes of the ground state structures. Theoretical predictions of the crossover-sizes and ground state structure for a given size vary dramatically depending on the choice of potential, and experimental studies have not been able to clarify this due to kinetic trapping during growth and the non-negligible Boltzmann weight of higher energy structures at room temperature. Moreover, many of the experimental studies do not have the level of size control required to address the issue of structure versus cluster size. The work presented in this thesis aims to address the issue of determining the ground state structure for a specific cluster size (concentrating on the catalytically active size regime). This is achieved through the production of highly controlled cluster samples (specific size and growth conditions), and the use of electron-beam manipulation and in-situ heating in the aberration corrected STEM. It is the combination of these techniques that allows the ground state structure for a specific size cluster to be determined

both qualitatively and quantitatively. In particular, the quantitative determination of the energy difference between structural isomers may act as a bench-mark for future theoretical calculations.

1.5 Scanning Transmission Electron Microscopy

It is well known the resolution of a microscope is diffraction limited. The Rayleigh criterion gives that for a wave with wavelength λ in a material with refractive index n, with convergence angle θ the distance below which two points cannot be distinguished, d, is [107]:

$$d = \frac{0.612\lambda}{\sin\theta} \tag{1.9}$$

Hence, for light microscopes, the wavelength of light ultimately limits the resolution and atomic resolution is not possible. A solution to this problem is to use electrons, which have a much smaller wavelength than light. The de Broglie equation states that the wavelength of an electron is given by

$$\lambda = \frac{h}{mv}. \tag{1.10}$$

Where m is the mass of the particle and v is the velocity of the particle. By accelerating electrons to high speeds, wavelengths in the order of 1pm are obtained making atomic resolution imaging possible [108] (note: in a (S)TEM electrons are accelerated to close to the speed of light ($\approx$ 90% for 200kV accelerating voltage) meaning that relativistic effects should also be accounted for).

The first TEM was developed in 1931 by Ernst Ruska and he was subsequently awarded the 1986 Nobel prize in physics for his contribution [109]. Ardenne developed the STEM shortly afterwards, in 1938 [108]. The basic principle of the TEM is that a beam of high-energy electrons illuminates a thin specimen and the transmitted beam is detected to form an image. By comparison, in a STEM a high-energy electron beam is focused to form a small probe that is rastered across the sample scan

area. Various detectors then collect the transmitted and scattered electrons and the signal intensity at each raster point forms the image. A schematic of an ac-STEM is shown in figure 1.19. Magnification is not achieved directly through the use of lenses; however, the electron beam probe is formed by electron lenses. This means that the probe will have aberrations that limit the resolution (size of probe). These aberrations can now be corrected for and modern ac-STEM's routinely achieve <1Å resolution.

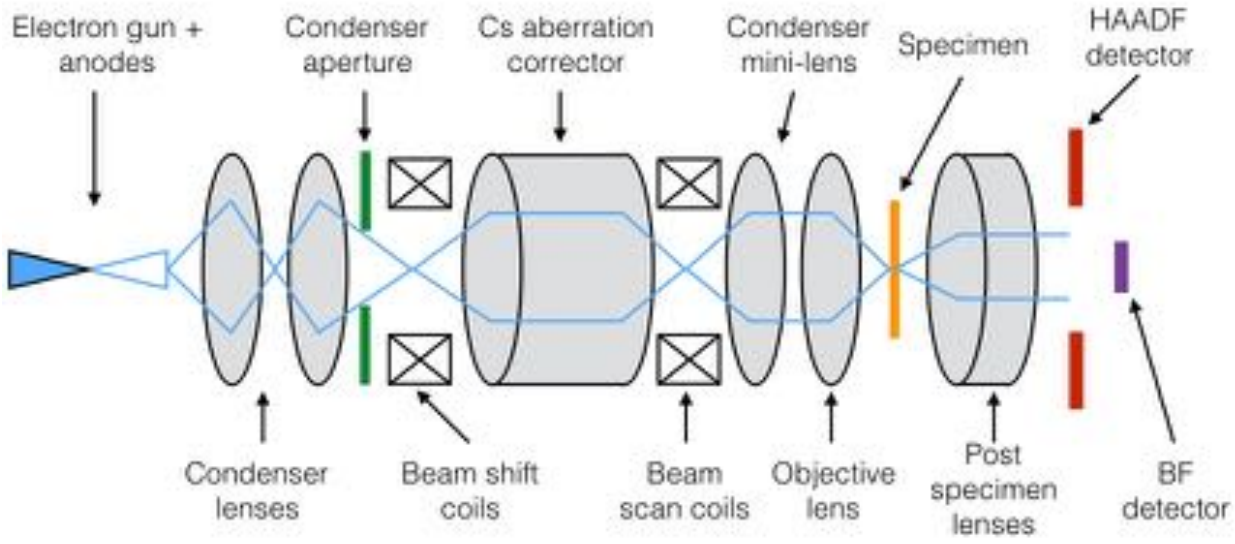

Figure 1.19: Schematic of an aberration corrected STEM.

A benefit of the STEM is that multiple signals can be obtained simultaneously; the direct beam can be collected by a bright field (BF) detector, electrons scattered at low angles by an annular dark field (ADF) detector, and those electrons scattered through high angles by a high angle annular dark field (HAADF) detector. Analytical information on chemical composition can also be obtained by analysis of characteristic x-rays produced when the electron beam interacts with the sample (EDX) and electron energy loss spectra (EELS).

1.5.1 Electron Guns

Electron guns are comprised of an electron source (a cathode) followed by an anode to accelerate the electrons to high energies. There are several different variations

used in (S)TEM's; thermionic emission sources, Schottky emission sources and field emission sources.

Thermionic electron guns are made of either W or LaB_6 crystals filaments. When heated they produce electrons because the increase in temperature provides enough energy for electrons to overcome the material work function and leave the surface. Following the filament there is an annular metal electrode with a negative potential (called a Whenelt cylinder) that controls the beam current via the aperture size and negative bias voltage. A variation on this design is to apply an electric field to a tungsten filament to lower the potential barrier at the surface so that the temperature required for electrons to escape is lowered. Often a ZrO film coats the tip to further lower the work function of the tip. This is called a Schottky type gun. For both of these designs the high temperature results in a spread in the electron energies, increasing the effect of chromatic aberration. For cold field emission electron guns the energy spread is much narrower. This type of gun is made from a thin tungsten needle and relies on the principle that the electric field strength is larger at a sharp point; if a tip of radius r has a voltage, V, applied to it then the electric field $E = V/r$, so a smaller radius leads to a larger electric field. When a strong electric field is applied between the tungsten needle and an anode, as long as the potential barrier is narrow enough, the electrons tunnel from the tip to the vacuum. The surface must be free of contaminants for tunnelling to occur, this means that the electron gun must be in UHV. [107] [108]

1.5.2 Electron Lenses

The electron beam in a STEM (and TEM) is focused using magnetic lenses. The basic design of a magnetic lens is shown in figure 1.20, taken from reference 106. The lens consists of a current carrying copper coil surrounded by soft iron to contain the magnetic field. In the centre of the coil, the bore, there is a gap where the magnetic field is strongest. Polepieces (ferromagnetic soft iron with a small diameter hole) either side of the gap confine the field to a smaller region in the bore, creating a thin

lens with a radial change in magnetic field. The electron trajectories are determined by the strength of the magnetic field, which is weakest at the axis and stronger further towards the polepieces. It should be noted that electrons actually follow a helical trajectory, not straight lines as shown in figure 1.20. [107, 108].

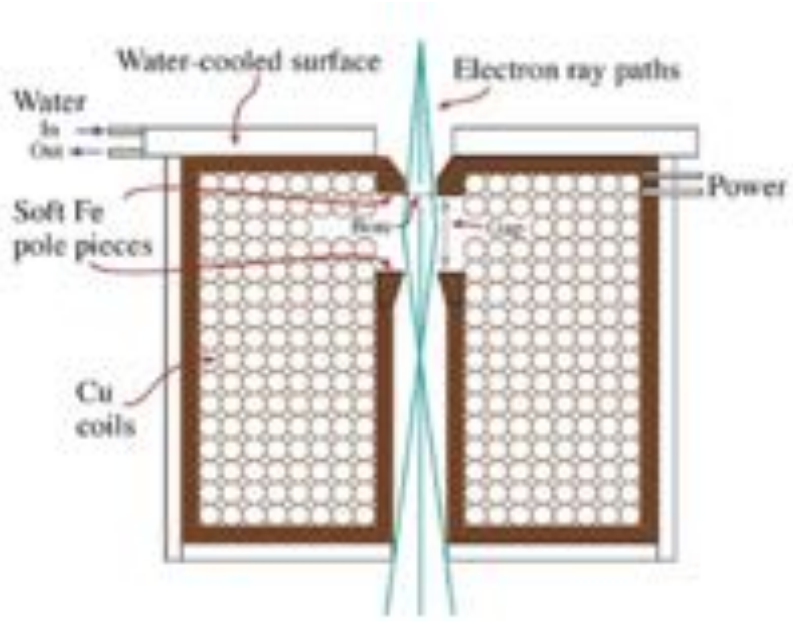

Figure 1.20: A cross-sectional diagram of a magnetic lens. Diagram taken from reference 106 .

1.5.3 Electron Lens Aberrations

Electron lenses suffer from several aberrations; as a result the resolution of the microscope is reduced. In the case of the STEM, the image is formed by the probe and so it is the probe-forming lenses that introduce these aberrations. Three of the main aberrations: spherical, chromatic, and astigmatism will be discussed here, along with methods for correction.

Spherical Aberration

Spherical aberration occurs when electrons towards the edge of the lens are refracted more than those at the lens axis. As a consequence of this, the electrons do not converge at the same point (see figure 1.21). In a STEM the electron beam is focused to a small probe by electron lenses, the effect of aberrations in the lenses is

to increase the probe size (the beam is focused to a finite sized disk rather than a point), resulting in a decrease in image resolution. Spherical aberration in STEM's can be corrected by using a system of either quadrapole and hexapole or quadrapole and octupole lenses, controlled by computer, to re-converge the beam to a point. It has been shown that a probe size of 0.74Å can be achieved by using an aberration correction system consisting of four quadrapoles separated by three octupoles [110].

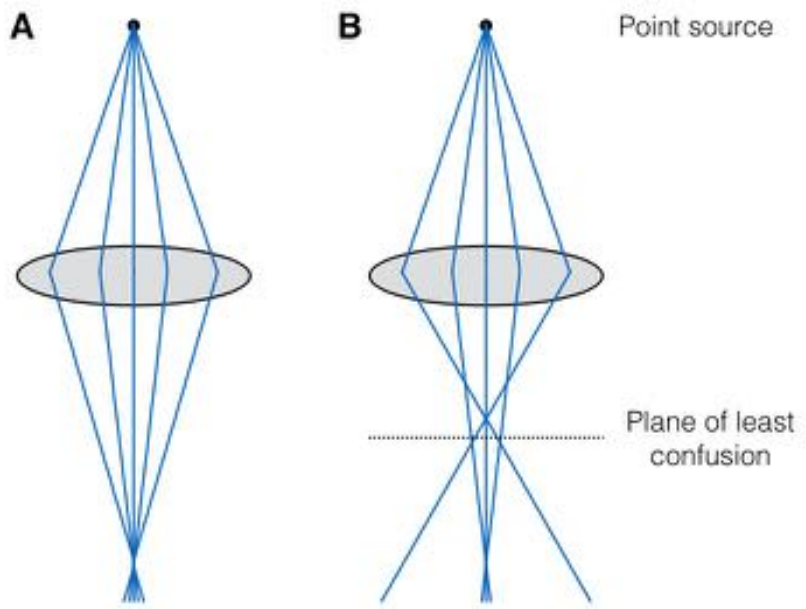

Figure 1.21: a) a schematic of a perfect lens and b) a schematic of a lens with spherical aberration. The plane of least confusion is the location where the smallest image of the source is formed.

Chromatic Aberration

Chromatic aberration results from the energy spread of the electrons in the beam; the electron lenses deflect the electrons with lower energy more than those with higher energy. This leads to a point object being imaged as a finite sized disk. This effect is largely reduced by using a field emission electron gun because the electrons emitted are more monochromatic.

Astigmatism

The electron lenses used to deflect the electron beam create a non-uniform magnetic field, this is because it is not possible to create completely spherical and symmetric polepieces. As a result, the focal length of the beam changes depending on the location around the lens axis. This defect can be corrected for using octupoles to balance out the field inhomogeneities. [107]

1.5.4 HAADF Z-contrast imaging

Z-contrast imaging is achieved in the STEM by only collecting the electrons scattered at high angles (>50 mrad), using a HAADF detector as shown in figure 1.22. Generally, when electrons are scattered from the nucleus, high angle scattering occurs, whereas when electrons are scattered by other electrons (the electron cloud) low angle scattering is more likely. The scattering cross section, σ_R, for electron scattering by the nucleus is given by the Rutherford equation, in which $\sigma_R \propto Z^2$ if electron screening is ignored. Equation 1.11 shows the Rutherford equation, corrected to include electron screening and relativistic effects.

$$\sigma_R(\theta) = \frac{Z^2\lambda_R^4}{64\pi^4 a_0^2} \frac{d\Omega}{\left(sin^2\frac{\theta}{2} + \frac{\theta_0^2}{4}\right)^2} \tag{1.11}$$

E_0 is the energy of the electrons (in keV), λ_R is the relativistically corrected electron wavelength, a_0 is the Bohr radius, θ is the scattering angle of the electrons, Ω is the solid angle and the screening parameter $\theta_0 = 0.117Z^{1/3}/E_0^{1/2}$ [107]. At lower electron scattering angles the electron screening effect is larger and Bragg diffraction (coherent elastic scattering) of electrons dominates over Rutherford scattering (incoherent elastic). It is the incoherent nature of the high-angle scattered electrons that enables Z-contrast imaging. Each electron scattered by the nucleus (Rutherford scattering) can be considered as a single scattering event, hence electrons scattered through high angles have no phase relationship with the incident electron beam - they are incoherent. This means that the intensity in HAADF STEM images is only

dependent on the atomic number, and not on the orientation or crystalline structure of the sample. Using an annular detector that only collects electrons scattered at very high angles (>50 mrad) means that coherent scattering (Bragg scattering) does not contribute to the image, instead incoherent scattering (Rutherford scattering) dominates and Z-contrast imaging is achieved.

The value of n in the relationship $I \propto Z^n$ for HAADF STEM imaging has been determined experimentally in reference 110. The calibration was performed by measuring the HAADF intensity of size selected Au_{923} and Pd_{923} nanoclusters. The relationship $I_{Au}/I_{Pd} = (Z_{Au}/Z_{Pd})^n$ was then used to calculate the value of the exponent n. It was found that for an inner collection angle of 62 mrad and outer collection angle of 164mrad, n = 1.46±0.18. This value increased to ≈1.8 when the inner collection angle was increased to 103mrad. It is noted that this value for the exponent is much less than the expected n=2 for solely Rutherford scattering and that electron screening is likely the reason for this.

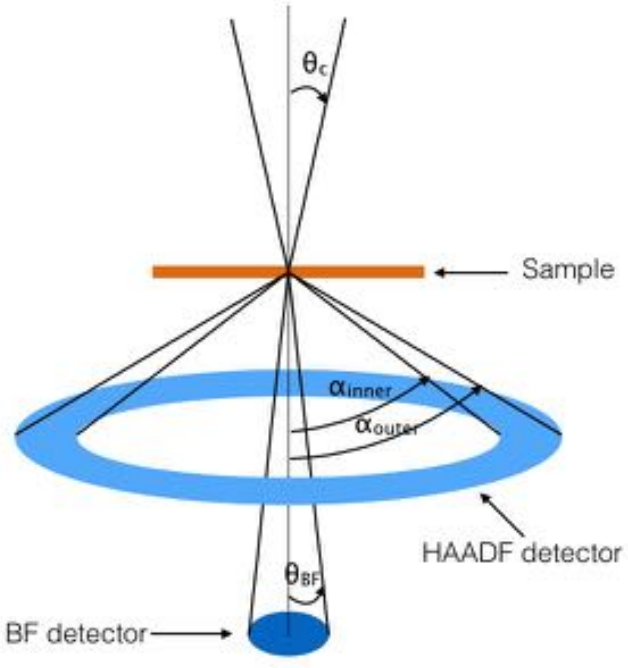

Figure 1.22: Schematic of HAADF and BF detector collection angles. θ_c is the beam convergence semi-angle, θ_{BF} is the collection semi-angle of the bright field detector, α_{inner} is the inner collection semi-angle of the HAADF detector and α_{outer} is the outer collection semi-angle of the HAADF detector. Generally, θ_{BF} is <10mrad and α_{inner} is > 50mrad.

As explained above, the HAADF intensity is proportional to the atomic number, Z ($I \propto Z^n$). Using a range (55-1500 atoms) of size-selected gold nanoclusters it has been shown that the relationship between cluster size and HAADF intensity is linear [51]. Therefore, if a cluster is made of a single chemical element, the HAADF intensity of an atomic column will be proportional to the number of atoms in that atomic column. In this sense the 3D atomic structure can be determined [51].

Generally, HAADF STEM is only used to study high-Z materials because of the higher electron scattering signal for these materials. However, it has been shown by Krivanek et al [112] that, using a low voltage (60kV) form of aberration corrected ADF STEM, the chemical identity and position of boron and nitrogen atoms in a hexagonal boron nitride monolayer can be determined. With this method, despite the low atomic number, the intensity difference between boron and nitrogen atoms could easily be distinguished.

1.5.5 Energy-Dispersive X-ray Spectroscopy

EDX provides analytical information on the chemical composition of a sample. When a high-energy electron beam of particles is incident on a material characteristic x-rays are produced. Figure 1.23 shows a schematic of characteristic x-ray production for a single atom. A high-energy electron excites an inner shell electron and it is ejected from the atom, an electron in a higher energy level then de-excites, dropping down to fill the gap and emits an x-ray photon with energy equal to the gap between the two energy levels. The difference between electron energy levels is specific to a particular chemical element; hence the energy of emitted x-ray photons gives information on chemical composition.

In the STEM, it is the high-energy electrons from the beam probe that excite inner-shell electrons in the sample resulting in characteristics x-ray emission. Because the beam probe is focused to a small point on the sample, spatial information is gained. The small probe size of aberration corrected machines means that it is possible to achieve atomic resolution with STEM-EDX, although this has only been

demonstrated using multiple detector set-ups to optimize the signal alongside simulation [113]. Different modes can be employed such that the beam rests on a single point of the sample, to obtain a point spectra or rasters across an area to produce a spectral map containing chemical and spatial information. EDX mapping can be particularly useful for determining the chemical composition of core shell bimetallic and oxide particles [113, 114].

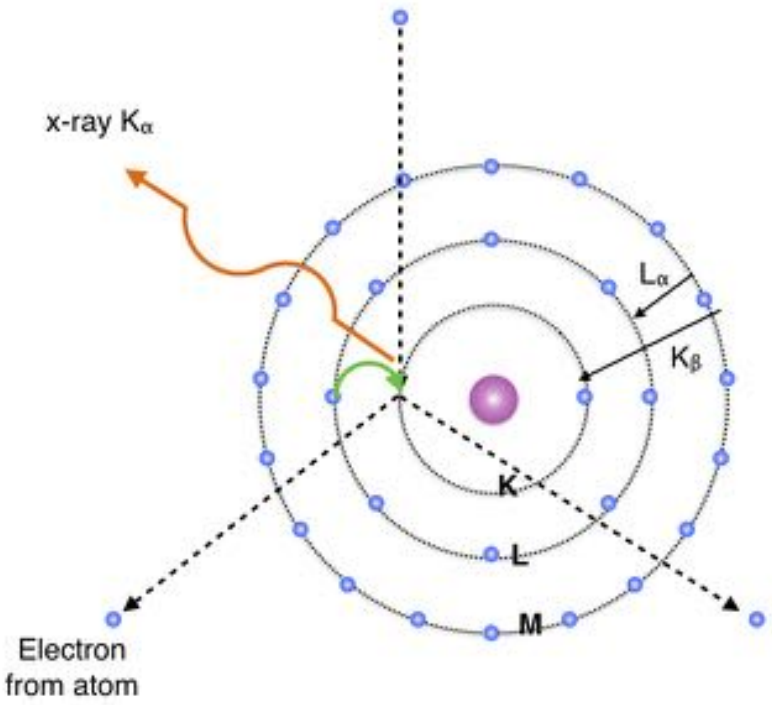

Figure 1.23: Characteristic x-ray production. Schematic shows an electron from the beam displacing an electron from the K-shell and a L-shell electron filling the vacancy and emitting a K_α x-ray.

1.5.6 Electron Energy Loss Spectroscopy

In EELS the energy lost by a beam of electrons that interacts with a sample is measured, this gives information on the electronic structure of the sample. Electrons that are inelastically scattered by inner-shell electrons will lose a certain amount of energy, given by the inner shell ionization energy. The energy lost is specific to a particular element. This creates energy edges in the EELS spectra that are

characteristic of a certain element. As well as elemental composition, information on valence states can be extracted from the fine structure of spectra, related to inter and intra band transitions, whilst inelastic scattering from outer shell electrons means that plasmons can also be detected in the low energy (<50eV) region of the EELS spectra [108]. Figure 1.24 shows a typical EELS spectra with various regions labelled.

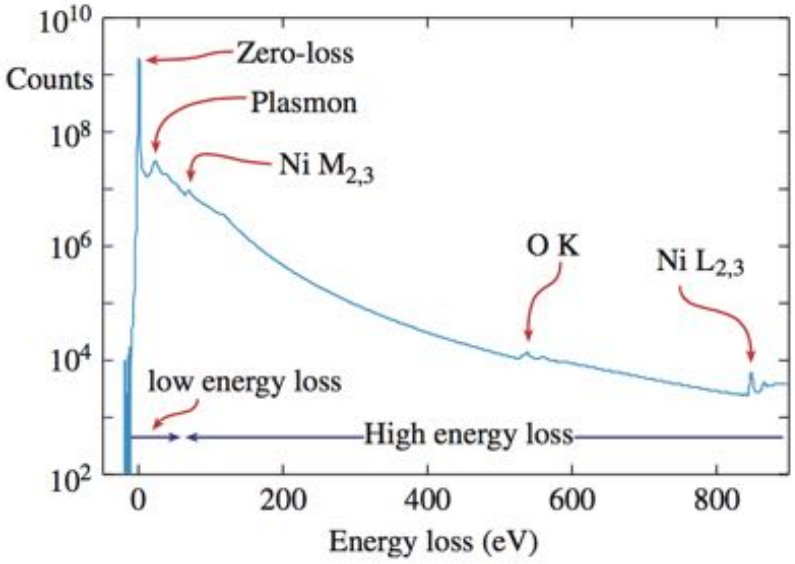

Figure 1.24: A typical EELS spectra indicating the zero-loss peak, low energy loss region and high energy loss region. The low energy loss region contains the plasmon signal and the high energy region contains core-loss ionisation edges. Figure from reference 106.

In the STEM the beam probe can be used as the beam of electrons for EELS measurements. A schematic of a STEM-EELS system is shown in figure 1.25. After the electrons are transmitted through the sample, they enter a spectrometer. The spectrometer uses a magnetic field to spatially separate electrons with different energies. Once separated according to energy the electrons are then focused on to a detector and their energies determined according to position. A narrower spread in energy will result in higher energy resolution; therefore cold field emission electron sources are preferable. Monochromators can also be used to reduce the energy spread but this results in loss of signal.

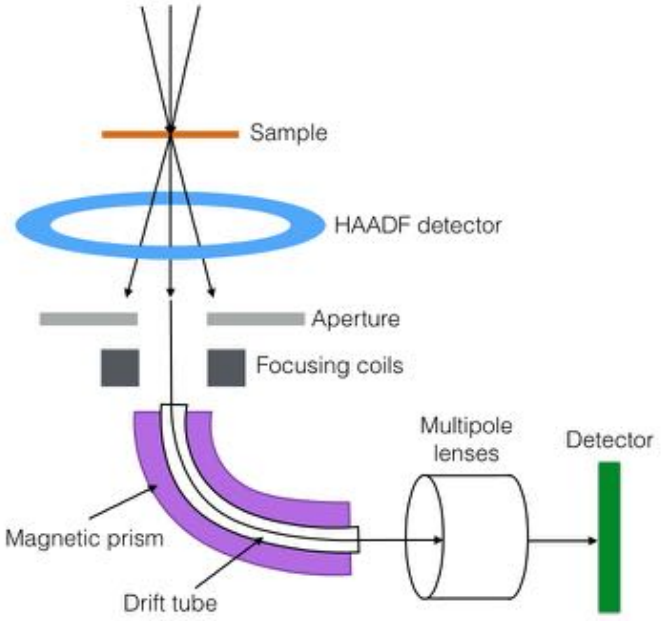

Figure 1.25: Schematic of EELS spectrometer in the STEM.

References

[1] F Baletto and R Ferrando. Structural properties of nanoclusters : Energetic, thermodynamic, and kinetic effects. *Reviews of Modern Physics*, 77:371–417, 2005.

[2] W de Heer. The physics of simple metal clusters: experimental aspects and simple models. *Reviews of Modern Physics*, 65(3):611–676, jul 1993.

[3] S Bals, S Van Aert, C P Romero, K Lauwaet, M J Van Bael, B Schoeters, B Partoens, E Yücelen, P Lievens, and G Van Tendeloo. Atomic scale dynamics of ultrasmall germanium clusters. *Nature Communications*, 3(May):897, jan 2012.

[4] B W van de Waal and G Torchet. Structure of large argon clusters Ar_N, 10^3<N<10^5: experiments and simulations. *Chemical Physics Letters*, 331:57–63, 2000.

[5] F Yin, Z W Wang, and R E Palmer. Controlled formation of mass-selected Cu-Au core-shell cluster beams. *Journal of the American Chemical Society*, 133:10325–10327, 2011.

[6] V Ortalan, A Uzun, B C Gates, and N D Browning. Towards full-structure determination of bimetallic nanoparticles with an aberration-corrected electron microscope. *Nature nanotechnology*, 5(12):843–7, dec 2010.

[7] J A Alonso. *Structure and properties of atomic nanoclusters*. Imperial College Press, 2 edition, 2012.

[8] P Jena and A W Castleman. Introduction to atomic clusters. In *Nanoclusters - A Bridge across Disciplines*, number 10 in Science and Technology of Atomic, Molecular, Condensed Matter & Biological Systems, chapter 1, pages 1–36. Elsevier, 1 edition, 2010.

[9] Y Negishi, K Nobusada, and T Tsukuda. Glutathione-protected gold clusters revisited : bridging the gap between gold (I) - thiolate complexes and thiolate-protected gold nanocrystals. *Journal of the American Chemical Society*, 127:5261–5270, 2005.

[10] Ph Buffat and J P Borel. Size effect on the melting temperature of gold particles. *Physical Review A*, 13(6):2287–2298, 1976.

[11] A Shvartsburg and M Jarrold. Solid clusters above the bulk melting point. *Physical Review Letters*, 85:2530–2532, 2000.

[12] P Hernandez-Fernandez, F Masini, D N McCarthy, C E Strebel, D Friebel, D Deiana, P Malacrida, A Nierhoff, A Bodin, A M Wise, J H Neilsen, T W Hansen, A Nilsson, I E L Stephens, and I Chorkendorff. Mass-selected nanoparticles of Pt_xY as model catalysts for oxygen electroreduction. *Nature Chemistry*, 6:732–738, 2014.

[13] Z Liu, X Y Ling, X Su, and J Y Lee. Carbon-supported Pt and PtRu nanoparticles as catalysts for a direct methanol fuel cell. *The Journal of Physical Chemistry B*, 108(24):8234–8240, jun 2004.

[14] F Studt, I Sharafutdinov, F Abild-Pedersen, Christian F Elkjaer, J S Hummelshoj, S Dahl, I Chorkendorff, and J K Norskov. Discovery of a Ni-Ga catalyst for carbon dioxide reduction to methanol. *Nature Chemistry*, 6:320–324, 2014.

[15] M Turner, V B Golovko, OP H Vaughan, P Abdulkin, A Berenguer-Murcia, M S Tikhov, B F G Johnson, and R M Lambert. Selective oxidation with dioxygen by gold nanoparticle catalysts derived from 55-atom clusters. *Nature*, 454(7207):981–3, 2008.

[16] C-K Kim, P Ghosh, and V M Rotello. Multimodal drug delivery using gold nanoparticles. *Nanoscale*, 1(1):61–7, oct 2009.

[17] K Saha, S Agasti, C Kim, X Li, and V M Rotello. Gold nanoparticles in chemical and biological sensing. *Chemical Reviews*, 112(5):2739–79, 2012.

[18] S S Agasti, A Chompoosor, C You, P Ghosh, C K Kim, and V M Rotello. Photoregulated release of caged anticancer drugs from gold nanoparticles. *Journal of the American Chemical Society*, 131:5728–5729, 2009.

[19] S Chernousova and M Epple. Silver as antibacterial agent: ion, nanoparticle, and metal. *Angewandte Chemie*, 52(6):1636–53, feb 2013.

[20] M Ahamed, M S Alsalhi, and M K J Siddiqui. Silver nanoparticle applications and human health. *Clinica Chimica Acta*, 411(23-24):1841–8, 2010.

[21] A Weir, P Westerhoff, L Fabricius, K Hristovski, and N von Goetz. Titanium dioxide nanoparticles in food and personal care products. *Environmental science & technology*, 46(4):2242–50, feb 2012.

[22] M Charles, E Scott, M Porterfield, and A Wei. Toxicological studies on silver nanoparticles : challenges and opportunities in assessment, monitoring and imaging. *Nanomedicine*, 6:879–898, 2011.

[23] W Knight, K Clemenger, W A De Heer, A Saunders, M Y Chou, and M L Cohen. Electronic shell strcuture and abundances of sodium clusters. *Physical Review Letters*, 52(24):2141–2143, 1984.

[24] T P Martin, T Bergmann, H Göhlich, and T Lange. Observation of electronic shells and shells of atoms in large Na clusters. *Chemical Physics Letters*, 172(3-4):209–213, 1990.

[25] P Stampfli and K H Bennemann. Unified model for the shell structure in the cohesive energy, ionisation potential, and photoyield of metallic clusters. *Physical Review Letters*, 69(24):3471–3474, 1992.

[26] B Baguenard, M Pellarin, J Lermé, J L Vialle, and M Broyer. Competition between atomic shell and electronic shell structures in aluminum clusters. *The Journal of Chemical Physics*, 100(1), 1994.

[27] S Ino. Stability of multiply-twinned particles. *Journal of the Physical Society of Japan*, 27(4):941–953, 1969.

[28] L D Marks. Surface structure and energetics of multiply twinned particles. *Philosophical Magazine A*, 49(1):81–93, 1984.

[29] C T Campbell. The active site in nanoparticle gold catalysis. *Science*, 306(5694):234–5, oct 2004.

[30] A Verdaguer-Casadevall, D Deiana, M Karamad, S Siahrostami, P Malacrida, T W Hansen, J Rossmeisl, I Chorkendor, and I E L Stephens. Trends in the electrochemical synthesis of H_2O_2: enhancing activity and selectivity by electrocatalytic site engineering. *Nano Letters*, 14:1603–1608, 2014.

[31] T Akita, M Kohyama, and M Haruta. Electron microscopy study of gold nanoparticles deposited on transition metal oxides. *Accounts of Chemical Research*, 46(8):1773–1782, 2013.

[32] A Corma and H Garcia. Supported gold nanoparticles as catalysts for organic reactions. *Chemical Society Reviews*, 37(9):2096–126, 2008.

[33] L Zhang and E Wang. Metal nanoclusters: new fluorescent probes for sensors and bioimaging. *Nano Today*, 9:132–157, feb 2014.

[34] S Huo, S Jin, X Xue, K Yang, A Kumar, P C Wang, J Zhang, Z Hu, and X-J Liang. Ultrasmall gold nanoparticles as carriers for nucleus-based gene therapy due to size-dependent nuclear entry. *ACS Nano*, 8(6):5852–5862, 2014.

[35] A Lechtken, C Neiss, M M Kappes, and D Schooss. Structure determination of gold clusters by trapped ion electron diffraction: Au_{14}^--Au_{19}^-. *Physical chemistry chemical physics*, 11(21):4344–50, jun 2009.

[36] K Schouteden, K Lauwaet, E Janssens, G Barcaro, A Fortunelli, C Van Haesendonck, and P Lievens. Probing the atomic structure of metallic nanoclusters with the tip of a scanning tunneling microscope. *Nanoscale*, 6(4):2170–6, feb 2014.

[37] S Ino. Epitaxial growth of metals on rocksalt faces cleaved in vacuum. II. Orientation and structure of gold particles formed in ultrahigh vacuum. *Journal of the Physical Society of Japan*, 21(2):346–362, 1966.

[38] S Ogawa, S Ino, T Kato, and H Ota. Epitaxial growth of face-centred cubic metals on alkalihalide crystals cleaved in ultrahigh vacuum. *Journal of the Physical Society of Japan*, 21(10):1963–1972, 1966.

[39] S Ino and S Ogawa. Multiply twinned particles at earlier stages of gold film formation on alkalihalide crystals. *Journal of the Physical Society of Japan*, 22(6):1365–1374, 1967.

[40] C Solliard, Ph Buffat, and F Faes. Equilibrium structure of small gold crystals. *Journal of Crystal Growth*, 32(1):123–125, 1976.

[41] M Flueli, R Spycher, P A Stadelma, P A Buffat, and J P Bore. High-resolution electron microscopy (HREM) on icosahedral gold small particles: image simulation and observations . *Europhysics Letters*, 6(4):349–352, 1988.

[42] P A Buffat, M Flueli, R Spycher, P Stadelmann, and J-P Borel. Crystallographic structure of small gold particles studied by high-resolution electron microscopy. *Faraday Discuss.*, 92:173–187, 1991.

[43] S Tehuacanero, R Herrera, M Avalos, and M Jose-Yacaman. High resolution TEM studies of gold and palladium nano-particles. *Acta metall, mater.*, 40(7):1663–1674, 1992.

[44] A N Patil, D Y Paithankar, N Otsuka, and R P Andres. The minimum-energy structure of nanometer-scale gold clusters. *Z. Phys. D*, 137:135–137, 1993.

[45] M P Ajayan and Marks. Experimental evidence for quasimelting in small particles. *Phys. Rev. Lett.*, 63(3), 1989.

[46] J F Creemer, M A Huis, N P Young, I Kirkland, and H W Zandbergen. Atomic imaging of phase transitions and morphology transformations in nanocrystals. *Advanced Materials*, 21:4992–4995, 2009.

[47] N Doraiswamy and L D Marks. Electron beam induced small particle transformations: temperature. *Surface Science*, 348(1-2):L67–L69, 1996.

[48] K Koga and K Sugawara. Population statistics of gold nanoparticle morphologies: direct determination by HREM observations. *Surface Science*, 529(1-2):23–35, apr 2003.

[49] K Koga, T Ikeshoji, and K Sugawara. Size-and temperature-dependent structural transitions in gold nanoparticles. *Physical Review Letters*, 92(11):115507, mar 2004.

[50] K Bao, S Goedecker, K Koga, F Lançon, and A Neelov. Structure of large gold clusters obtained by global optimization using the minima hopping method. *Physical Review B*, 79(041405(R)):1–4, 2009.

[51] Z Y Li, N P Young, M Di Vece, S Palomba, R E Palmer, A L Bleloch, B C Curley, R L Johnston, J Jiang, and J Yuan. Three-dimensional atomic-scale structure of size-selected gold nanoclusters. *Nature*, 451(7174):46–8, jan 2008.

[52] Z W Wang and R E Palmer. Direct atomic imaging and dynamical fluctuations of the tetrahedral Au_{20} cluster. *Nanoscale*, 4(16):4947–9, aug 2012.

[53] Z W Wang and R E Palmer. Experimental evidence for fluctuating, chiral-type Au_{55} clusters by direct atomic imaging. *Nano Letters*, 12:5510–5514, 2012.

[54] Z W Wang and R E Palmer. Determination of the ground-state atomic structures of size-selected Au nanoclusters by electron-beam-induced transformation. *Physical Review Letters*, 108(24):245502, jun 2012.

[55] S R Plant, L Cao, and R E Palmer. Atomic structure control of size-selected gold nanoclusters during formation. *Journal of the American Chemical Society*, 136(21):7559–7562, 2014.

[56] N Young, Z Li, Y Chen, S Palomba, M Di Vece, and R E Palmer. Weighing supported nanoparticles: size-selected clusters as mass standards in nanometrology. *Physical Review Letters*, 101(24):246103, dec 2008.

[57] K E MacArthur, N P Young, J W Critchell, and A I Kirkland. 'Ex - Situ' annealing and structural transformations in gold nanoparticles. *Jounal of Physics: conference series*, 371, 2012.

[58] J Li, D Yin, C Chen, Q Li, L Lin, R Sun, S Huang, and Z Wang. Atomic-scale observation of dynamical fluctuation and three-dimensional structure of gold clusters. *Journal of Applied Physics*, 085303(2015), 2016.

[59] A S Barnard, N P Young, A I Kirkland, M A Van Huis, and X Huifang. Nanogold: a quantitative phase map. *ACS Nano*, 3(6):1431–1436, 2009.

[60] F Baletto, R Ferrando, A Fortunelli, F Montalenti, and C Mottet. Crossover among structural motifs in transition and noble-metal clusters. *The Journal of Chemical Physics*, 116(9):3856–3863, 2002.

[61] C-L Kuo and P Clancy. Melting and freezing characteristics and structural properties of supported and unsupported gold nanoclusters. *Journal of Chemical Physics B*, 109:13743–13754, 2005.

[62] H Li, L Li, A Pedersen, Y Gao, N Khetrapal, H Jonsson, and X C Zeng. Magic-number gold nanoclusters with diameters from 1 to 3.5 nm: relative stability and catalytic activity for CO oxidation. *Nano Letters*, 15:682–688, 2015.

[63] B Wang, M Liu, Y Wang, and X Chen. Structures and energetics of silver and gold nanoparticles. *The Journal of Physical Chemistry C*, 115(23):11374–11381, jun 2011.

[64] A S Barnard. A thermodynamic model for the shape and stability of twinned nanostructures. *Journal of Physical Chemistry B*, 110(48):24498–24504, 2006.

[65] B C Curley, R L Johnston, NP Young, Z Y Li, M Di Vece, R E Palmer, and A L Bleloch. Combining theory and experiment to characterize the atomic structures of surface-deposited Au_{309} clusters. *Journal of Chemical Physics C*, 111:17846–17851, 2007.

[66] H Nam, N M Hwang, B D Yu, D Kim, and J Yoon. Free energy approach to the formation of an icosahedral structure during the freezing of gold nanoclusters. *Physical Review B*, pages 1–4, 2005.

[67] G Rossi and R Ferrando. Freezing of gold nanoclusters into poly-decahedral structures. *Nanotechnology*, 18(22):225706, jun 2007.

[68] C C Asuquo and R K Bowles. Molecular dynamics simulations of competitive freezing in gold nanoclusters. *The Journal of Physical Chemistry C*, 2012.

[69] Y Wang, S Teitel, C Dellago, Y Wang, and S Teitel. Melting of icosahedral gold nanoclusters from molecular dynamics simulations Melting of icosahedral gold nanoclusters from molecular dynamics simulations. *The Journal of chemical physics*, 214722(2005), 2007.

[70] G Guenther and O Guillon. Models of size-dependent nanoparticle melting tested on gold. *Journal of Materials Science*, 49(23):7915–7932, 2014.

[71] Y G Chushak and L S Bartell. Melting and freezing of gold nanoclusters. *J. Phys. Chem. B*, 105:11605–11614, 2001.

[72] H Reiss and I B Wilson. The effect of surface on melting point. *Journal of Colloid Science*, 3(6):551–561, 1948.

[73] K J Hanszen. Theoretische untersuchungen uber den schmelzpunkt kleiner kugelchen. *Zeitschrift fur Physik*, 157(5):523–553, 1960.

[74] N D Lisgarten, J R Sambles, and L M Skinner. Vapour pressure over curved surfaces-the Kelvin equation. *Contemporary Physics*, 12(6):575–593, 1971.

[75] P R Couchman and W A Jesser. Thermodynamic theory of size dependence of melting temperature in metals. *Nature*, 269(5628):481–483, 1977.

[76] J R Sambles. An electron microscope study of evaporating gold particles: the Kelvin equation for liquid gold and the lowering of the melting point of solid gold particles. *Proceedings of the Royal Society A: Mathematical, Physical and Engineering Sciences*, 324(1558):339–351, 1971.

[77] T Castro, R Reifenberger, E Choi, and R P Andres. Size-dependent melting temperature of individual nanometer-sized metallic cluster. *Physical Review B*, 42, 1990.

[78] P Pawlow. The dependency of the melting point on the surface energy of a solid body. *Z. Phys. Chemie*, 65:545–548, 1909.

[79] C L Cleveland, W D Luedtke, and U Landman. Melting of gold clusters. *Physical Review B*, 60(7), 1999.

[80] F Ercolessi, W Andreoni, and E Tosatti. Melting of small gold particles: mechanism and size effects. *Physical Review Letters*, 66(7), 1991.

[81] J Lee, J Lee, T Tanaka, and H Mori. In situ atomic-scale observation of melting point suppression in nanometer-sized gold particles. *Nanotechnology*, 20(47):475706, 2009.

[82] N P Young, M A van Huis, H W Zandbergen, H Xu, and A I Kirkland. Transformations of gold nanoparticles investigated using variable temperature high-resolution transmission electron microscopy. *Ultramicroscopy*, 110(5):506–516, 2010.

[83] S Ali, V S Myasnichenko, and E C Neyts. Size-dependent strain and surface energies of gold nanoclusters. *Physical Chemistry Chemical Physics*, 18(January 2016):792–800, 2015.

[84] F Chen, Z Y Li, and R L Johnston. Surface reconstruction precursor to melting in Au_{309} clusters. *AIP Advances*, 1(032105):1–8, 2011.

[85] C L Cleveland, W D Luedtke, and U Landman. Melting of gold clusters: icosahedral precursors. *Physical Review Letters*, 81(10):2036–2039, 1998.

[86] L J Lewis, P Jensen, and J-L Barrat. Melting, freezing, and coalescence of gold nanoclusters. *Physical Review B*, 56(4):2248–2257, 1997.

[87] J Lee, T Tanaka, J Lee, and H Mori. Effect of substrates on the melting temperature of gold nanoparticles. *Computer Coupling of Phase Diagrams and Thermochemistry*, 31:105–111, 2007.

[88] J-H Shim, B-J Lee, and Y W Cho. Thermal stability of unsupported gold nanoparticle: a molecular dynamics study. *Surface Science*, 512:262–268, 2002.

[89] N Wang, S I Rokhlin, and D F Farson. Nonhomogeneous surface premelting of Au nanoparticles. *Nanotechnology*, 19:415701, 2008.

[90] L C Stoehr, E Gonzalez, A Stampfl, E Casals, A Duschl, V Puntes, and G J Oostingh. Shape matters: effects of silver nanospheres and wires on human alveolar epithelial cells. *Particle and Fibre Toxicology*, 8:36, 2011.

[91] P Christopher and S Linic. Shape-and size-specific chemistry of Ag nanostructures in catalytic ethylene epoxidation. *ChemCatChem*, 2(1):78–83, 2010.

[92] D Reinhard, B D Hall, D Ugarte, and R Monot. Size-independent fcc-to-icosahedral structural transition in unsupported silver clusters: An electron diffraction study of clusters produced by inert-gas aggregation. *Physical Review B*, 55(12):7868–7881, 1997.

[93] D Schooss, M N Blom, J H Parks, B Issendorf, H Haberland, and M M Kappes. The structures of Ag_{55}^{+} and $Ag_{55}{}^{-}$: trapped ion electron diffraction and density functional theory. *Nano Letters*, 5(10):1972–1977, 2005.

[94] I Barke, H Hartmann, D Rupp, L Flu, M Sauppe, M Adolph, S Schorb, C Bostedt, R Treusch, C Peltz, S Bartling, and T Fennel. The 3D-architecture of individual free silver nanoparticles captured by X-ray scattering. *Nature Communications*, 6(6187):1–7, 2015.

[95] M A Gracia-pinilla, D Ferrer, S Mejia-Rosales, and E Perez-Tijerina. size-selected Ag nanoparticles with five-fold symmetry. *Nano Express*, 4:896–902, 2009.

[96] A Volk, P Thaler, M Koch, E Fisslthaler, W Grogger, and W E Ernst. High resolution electron microscopy of Ag-clusters in crystalline and non-crystalline morphologies grown inside superfluid helium nanodroplets. *The Journal of Chemical Physics*, 138(214312):1–7, 2013.

[97] D R Jennison, D R Jennison, P A Schultz, P A Schultz, M P Sears, and M P Sears. Ab initio calculations of Ru, Pd, and Ag cluster structure with 55, 135, and 140 atoms. *Journal of Chemical Physics*, 106(5):1856–1862, 1996.

[98] J Doye and D Wales. Global minima for transition metal clusters described by sutton-chen potentials. *New Journal of Chemistry*, 93(22):16, 1997.

[99] I L Garzo, K Michaelian, and N Rendon. Structure and energetics of Ni, Ag, and Au nanoclusters. *Physical Review B*, 60(3):2000–2010, 1999.

[100] D Alamanova, V G Grigoryan, and M Springborg. Theoretical study of the structure and energetics of silver clusters. *Journal of Physical Chemistry C*, 111:12577–12587, 2007.

[101] A M Angulo and C Noguez. Atomic structure of small and intermediate-size silver nanoclusters. *Journal of Physical Chemistry A*, 112:5834–5838, 2008.

[102] W Huang, X Lai, and R Xu. Structural optimization of silver clusters from to using a modified dynamic lattice searching method with constructed core. *Chemical Physics Letters*, 507(1–3):199–202, 2011.

[103] F Baletto, C Mottet, and R Ferrando. Reentrant morphology transition in the growth of free silver nanoclusters. *Physical Review Letters*, 84(24):5544–5547, jun 2000.

[104] F Baletto, C Mottet, and R Ferrando. Microscopic mechanisms of the growth of metastable silver icosahedra. *Physical Review B*, 63(15):155408, mar 2001.

[105] F Baletto, C Mottet, and R Ferrando. Freezing of silver nanodroplets. *Chemical Physics Letters*, 354:82–87, 2002.

[106] P Thaler, A Volk, M Ratschek, M Koch, and W E Ernst. Molecular dynamics simulation of the deposition process of cold Ag-clusters under different landing conditions. *Journal of Chemical Physics*, 140(4), 2014.

[107] D B Williams and C B Carter. *Transmission electron microscopy*. Springer, 2009.

[108] R F Egerton. *Physical principles of electron microscopy*. Springer, 2005.

[109] E Ruska. The development of the electron microscope and of electron microscopy. *Bioscience Reports*, 7(8):607–629, 1987.

[110] P E Batson, N Dellby, and O L Krivanek. Sub-angstrom resolution using aberration corrected electron optics. *Nature*, 418:617–620, 2002.

[111] Z W Wang and R E Palmer. Intensity calibration and atomic imaging of size-selected Au and Pd clusters in aberration-corrected HAADF-STEM. *Journal of Physics: Conference Series*, 371:012010, jul 2012.

[112] O L Krivanek, M F Chisholm, V Nicolosi, T J Pennycook, G J Corbin, N Dellby, M F Murfitt, C S Own, Z S Szilagyi, M P Oxley, S T Pantelides, and S J Pennycook. Atom-by-atom structural and chemical analysis by annular dark-field electron microscopy. *Nature*, 464(7288):571–4, mar 2010.

[113] P Lu, L Zhou, M J Kramer, and D J Smith. Atomic-scale chemical imaging and quantification of metallic alloy structures by energy-dispersive X-ray spectroscopy. *Scientific Reports*, 4:3945, 2014.

[114] E A Lewis, T J A Slater, E Prestat, A Macedo, P O Brien, P H C Camargo, and S J Haigh. Real-time imaging and elemental mapping of AgAu nanoparticle transformations. *Nanoscale*, 6:13598–13605, 2014.

Chapter 2

Experimental Methods

For all the results presented in this thesis, size-selected clusters were produced using a magnetron sputtering gas aggregation cluster beam source [1] with lateral time of flight mass filter [2], and characterised using aberration corrected STEM. For the in-situ heating of Au clusters a DENS Solutions Wildfire heating holder was used. Ag samples, due to their sensitivity to air, were transferred in inert gas, using a specially designed glove box. All of these pieces of apparatus and methods for their use are discussed in detail below. The method for characterisation of atomic structure, involving comparison of HAADF STEM images with multi-slice simulated images, is also described.

2.1 Cluster Beam Deposition

2.1.1 Magnetron Sputtering Gas Aggregation Cluster Beam Source

A schematic of the magnetron sputtering gas aggregation source used in this work is shown in figure 2.1. It consists of four regions: a condensation chamber for sputtering and cluster growth, ion optics for focusing of the cluster beam, a lateral time of flight mass filter, and a deposition chamber. Each region is pumped using turbomolecular pumps backed by rotary pumps to obtain a base pressure of $\approx 10^{-7}$mbar.

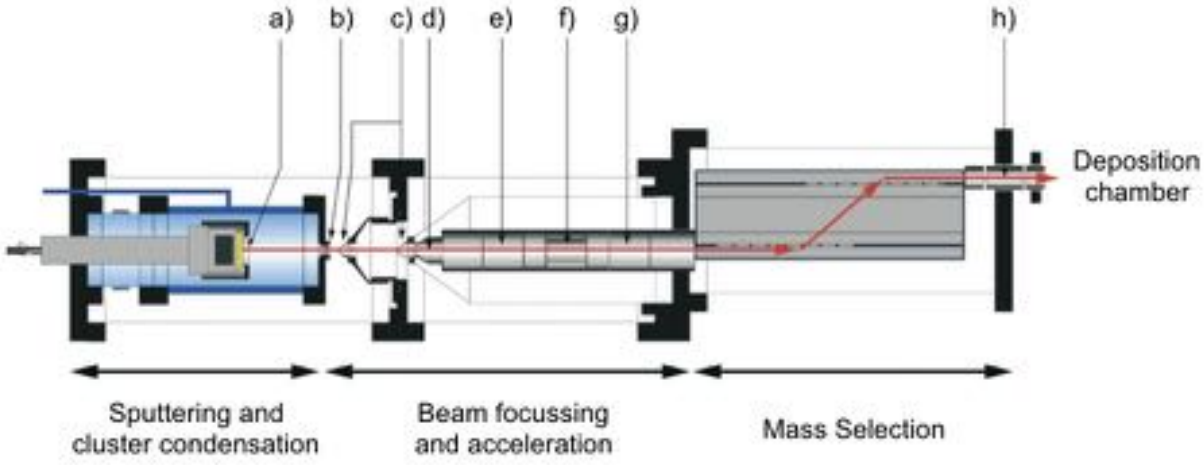

Figure 2.1: The magnetron sputtering, gas aggregation cluster source with lateral time-of flight mass filter. a) magnetron gun with target inserted, b) adjustable-diameter nozzle, c) electrostatic skimmer, d) high voltage lens, e) einzel lens, f) X-Y deflector plates, g) einzel lens h) post LTOF einzel lenses. The LTOF mass filter is shown in the mass selection region, with red arrows indicating cluster trajectories. The deposition chamber is located to the right hand side of the mass filter, directly after the post LTOF einzel lenses. Figure and adapted caption from reference 1.

The condensation chamber contains a magnetron gun with a 2-inch target of the required cluster material (e.g. Au, Ag) inserted. At the exit of the condensation chamber is a nozzle that can be adjusted from 0 to 10mm, to control the pressure in the chamber. The magnetron gun is mounted on a liner shift so that the distance from the gun to the nozzle can be varied between 150 and 250 mm. Argon gas is flowed into the chamber with the magnetron gun and an argon plasma is ignited by applying a high voltage to the sputter target. The potential of the plasma is more positive than ground due to screening effects, and the target is biased; hence an electric field is created between the plasma and the target. As a result Ar ions are accelerated towards the target and sputter atoms off the target material. Magnets in the magnetron gun further enhance the plasma. The injection of helium gas into the chamber gives rise to cluster condensation; sputtered material undergoes 3-body collisions with the He gas to form small cluster seeds and collisions of clusters with He atoms cool the clusters leading to condensation, hence growth, of larger clusters. The condensation chamber is also cooled by liquid nitrogen to further

cluster condensation. Two mass flow controllers allow for separate control of the Ar and He gas flow rates up to 200 sccm and the magnetron power can also be adjusted from 1-200W.

It has been shown in a previous study [1] that the size range of clusters produced by the source is dependent on the formation conditions; most important are the Ar and He gas pressures. The Ar gas pressure determines the sputter rate, and thus the amount of sputtered material. For a small cluster to form, a 3-body collision between two sputtered atoms and one helium atom must occur (to remove kinetic energy from the sputtered material), this is much more likely to happen if there is a higher density of sputtered material. By changing the He gas pressure it is possible to directly influence the size range of the clusters produced. At much larger He pressure the size distribution was found to be narrower and smaller clusters were produced; this is explained by the fact that increasing the amount of He, as well as increasing condensation of larger clusters, also increases the formation of small cluster seeds. When this process dominates, the cluster size will decrease as long as the amount of sputtered material remains constant. Other factors, such as gas flow rate and deformation of the target have also been shown to effect the size distribution. With increasing gas flow rate the mass of clusters produced also increases. This is explained in terms of clusters being more effectively removed from the chamber. When the target has been sputtered for a length of time a trench is formed due to the magnet that is used to increase the sputtering. Initially, this results in a higher sputter rate and increased cluster size because the magnetic field is stronger where the target has been depleted. However, after further deformation of the targets surface the plasma becomes distorted, less material is sputtered and thus the amount of clusters produced decreases.

The sputtering process results in approximately 30% of clusters being ionised in the plasma [1]. The ion optics which focus the beam are negatively biased, so it is the positive particles which are transmitted through the source to the deposition chamber. The ion optics consists of a variable voltage skimmer, a high voltage

extraction lens to accelerate the cluster beam, two variable einzel lenses to focus the beam and deflection plates to allow alignment of the beam position into the mass filter. The lateral time of flight filter allows for mass selection of the clusters and will be discussed in detail in the following section.

Following mass selection the cluster beam is guided into the deposition chamber. The deposition chamber contains a sample holder mounted on a linear shift, and a mask containing several apertures to ensure controlled cluster deposition. A negative bias voltage applied to the substrate determines the deposition energy of the clusters such that clusters can be soft landed or pinned to the substrate [3, 4, 5]. To measure the cluster current on the sample holder, a picoammeter is used, allowing for control of the deposited cluster density by knowledge of the beam current on the sample holder (through the mask) and subsequent alteration of the deposition time.

2.1.2 Lateral Time of Flight Mass Filter

A lateral time of flight mass filter, developed by Issendorf and Palmer [2], is attached to the cluster beam source, figure 2.2 shows a schematic of its design.

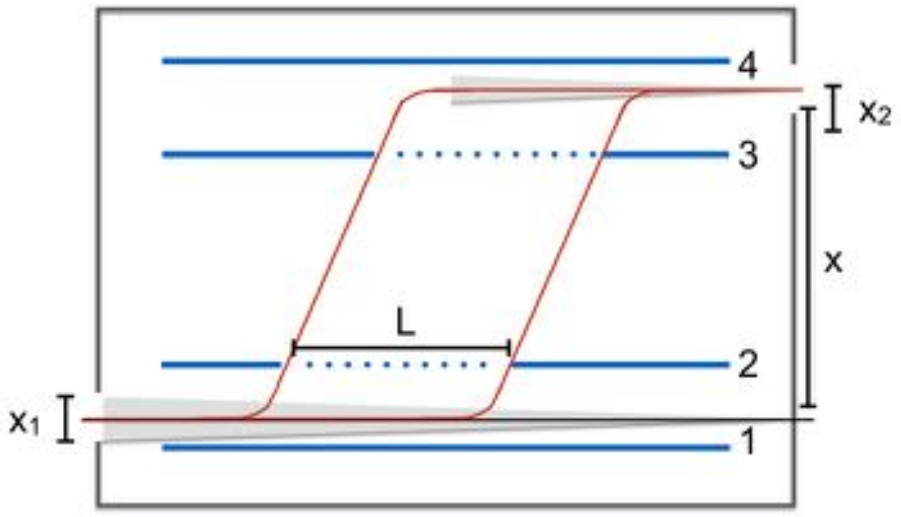

Figure 2.2: A schematic of the lateral time of flight mass filter. x is the lateral displacement of the cluster beam, L is the segment of the cluster beam used in each pulse series, x_1 is the size of the entrance aperture and x_2 is the size of the exit aperture.

The cluster beam enters the mass filter through an aperture at the bottom left, focused to a point opposite at the bottom right wall (this ensures the beam is focused when leaving the filter resulting in higher mass resolution). Initially the beam is accelerated upwards by a high voltage pulse applied to the bottom plate, the clusters then travel vertically through a field free region. The vertical displacement of the clusters is dependent on their mass (as well as pulse magnitude and timing), therefore clusters of different masses separate spatially into parallel beams. A second pulse is then applied to the top plate, identical to the first, to stop the vertical motion. Clusters of the selected size exit the filter through an aperture at the top right. By changing the timing of the pulses a particular mass can be selected, this is because the time a cluster takes to travel from the bottom to the top of the mass filter is dependent on its mass. If the cluster beam is well focused the theoretical mass resolution, R, is given by:

$$R = \frac{M}{\Delta M} = \frac{x}{\Delta x_2} \tag{2.1}$$

where M is the mass of the ion, ΔM is the width of masses that pass through the exit aperture, x is the lateral displacement of the selected mass and Δx_2 is the width of the exit aperture [2]. However, if the beam is not well focused then the size of the entrance aperture, x_1 will determine the beam size and the resolution is given by [6]:

$$R = \frac{M}{\Delta M} = \frac{x}{\sqrt{\Delta x_1 + \Delta x_2}}. \tag{2.2}$$

2.1.3 Practical Operation of the Cluster Beam Source

In preparation for cluster production the cluster beam source must be vented to change the target material and then pumped back down to 10^{-7}mbar. The condensation chamber must then be cooled by passing liquid nitrogen through its hollow outside, generally cooling takes approximately 2 hours and a temperature of $\approx$ -160°C is reached. A thermocouple is fitted inside of the condensation chamber so that the temperature can be monitored.

Once a stable temperature is reached, tuning for cluster production begins. To ignite the plasma and begin sputtering, the Ar gas flow into the condensation chamber is set to ≈100 sccm and a high voltage is applied to the target. Generally, for gold and silver, a magnetron power of 10W is used and the nozzle of the condensation chamber is fully open. Under these conditions it should be possible to detect a current of single atoms on the sample holder (using the picoammeter). To obtain larger clusters He gas is injected into the chamber, and gradually larger sizes of cluster are tuned for by adjusting the Ar and He gas flows, the condensation chamber pressure (via the nozzle size), and the ion optics voltages to obtain a maximum cluster current. Cluster currents in the order of 100pA are normal once tuning is complete.

The LTOF mass filter can be used for tuning either by selecting a specific size or by scanning over a size range to produce a mass spectrum. Figure 2.3 shows two mass spectra obtained for Au. A) shows a mass spectrum recorded between 100 and 500 amu, the Au_1 (197 amu) and Au_2 (394 amu) signal can be seen. A gaussian fit to the Au_1 signal gives a peak value of 196 ±11 amu. In this case the ion optics and formation conditions had been tuned to obtain a maximum Au_1 current. B) shows a mass spectrum recorded between 0 and 2000 amu. In this case the ion optics and formation conditions were tuned to obtain a maximum Au_{923} current. Table 2.1 shows the formation conditions corresponding to the mass spectra in figure 2.3.

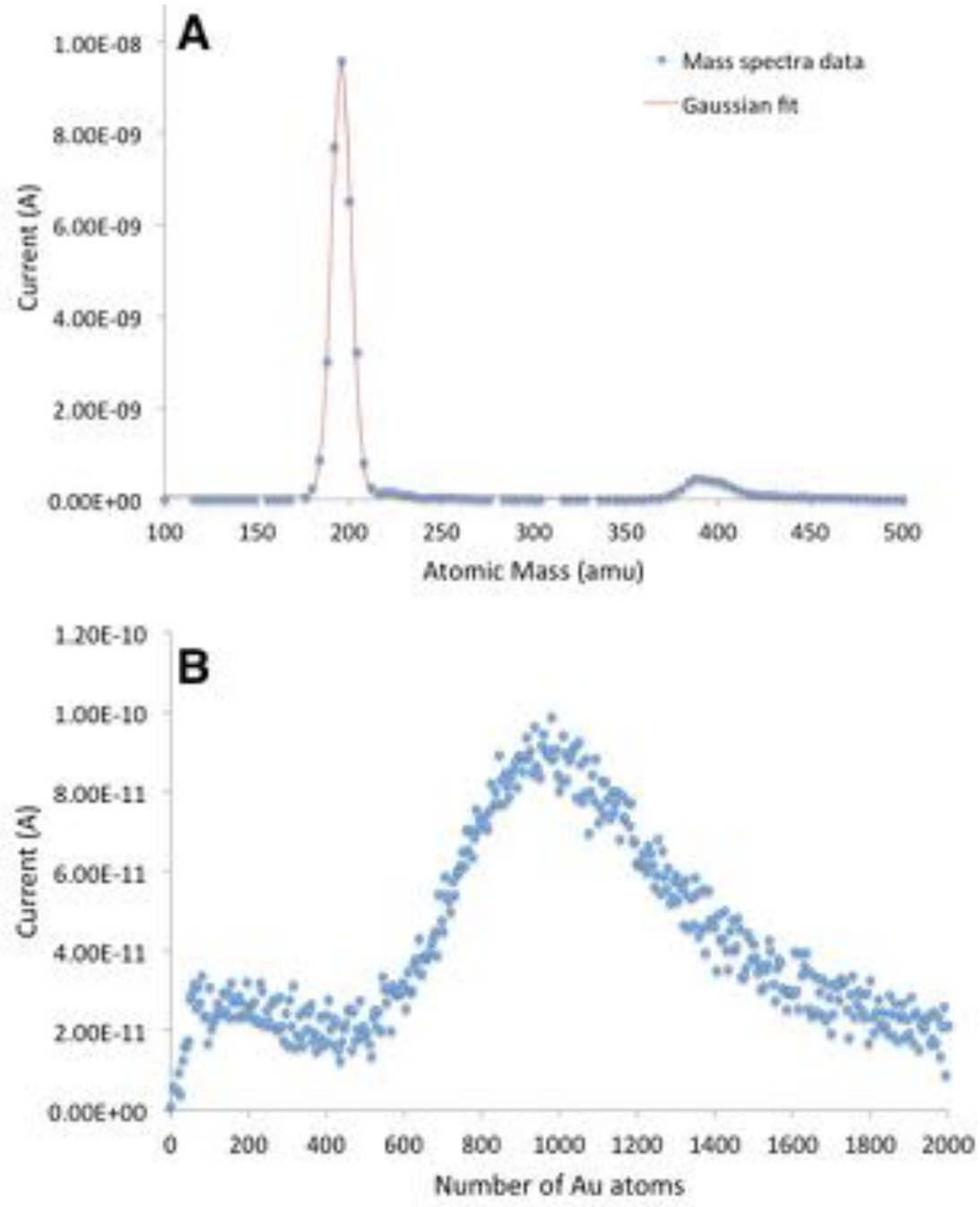

Figure 2.3: Mass spectra produced by the LTOF mass filter whilst a Au sputter target was inserted in the magnetron head. a) A mass spectra taken between 100 and 500 amu showing peaks for Au_1(197 amu) and Au_2(394 amu), in this case the ion optics and magnetron parameters were tuned for Au_1. b) A mass spectra taken between the amu of 0 and 2000 Au atoms, in this case the ion optics and magnetron source parameters were tuned for Au_{923}.

Formation parameter	Standard value
Magnetron power	10 W
Ar gas flow	100 sccm
He gas flow	0 sccm
Condensation chamber pressure	0.1 mbar
Condensation length	250 mm
Substrate voltage	1500 V

(a) Formation conditions used to obtain the mass spectra in 2.3A.

Formation parameter	Standard value
Magnetron power	10 W
Ar gas flow	200 sccm
He gas flow	180 sccm
Condensation chamber pressure	0.8 mbar
Condensation length	250 mm
Substrate voltage	1500 V

(b) Formation conditions used to obtain the mass spectra in 2.3B.

Table 2.1: Formation conditions corresponding to mass spectra in figure 2.3

Generally, to obtain larger sized clusters, higher Ar and He gas flows and higher pressures must be used. Typical conditions used for the production of Au_{561} clusters are shown in table 2.2.

Once the maximum cluster current has been tuned for, the resolution of the mass filter can be increased by inserting smaller entrance and exit apertures. For the majority of experiments the entrance aperture was kept fully open (8mm) and the exit aperture was 3mm, resulting in a mass resolution of $M/\Delta M = 21$. To deposit a sample, the pulses to the mass filter and the sample holder bias voltage are momentarily turned off while the sample is inserted. Sample substrates are attached to a sample plate and inserted on to a transfer arm in a load-lock chamber to be pumped down. Once the turbomolecular pump to the load lock is up to speed,

Table 2.2: Standard formation conditions for Au_{561} clusters.

Formation parameter	Standard value
Magnetron power	10 W
Ar gas flow	180-200 sccm
He gas flow	180-200 sccm
Condensation chamber pressure	0.8 mbar
Condensation length	250 mm
Substrate voltage	1000 V

the sample is transferred to the deposition chamber and inserted into the sample holder. The sample substrate should align with one of the apertures in the mask so that only the cluster current hitting the substrate is detected. To start deposition the sample holder bias voltage and mass filter are turned back on and the deposition is timed to allow for a controlled density of clusters to be deposited.

For standard STEM characterisation, samples were deposited onto 3mm Cu mesh TEM grids, coated with thin films (≈10-20 nm) of amorphous carbon or holey carbon. These substrates were chosen because the thin film and low atomic number means good contrast will be achieved in HAADF STEM. For in-situ heating experiments MEMS-based heating chips were used, these will be discussed in more detail in section 2.2. In all cases the deposition density was chosen such the clusters would be monodisperse (negligible aggregation), but high enough for ease of imaging in the STEM. Typically, the deposition density was between 0.2 and 0.4 clusters per $100nm^2$. Figure 2.4 shows a typical low magnification STEM image of a Au_{561} sample.

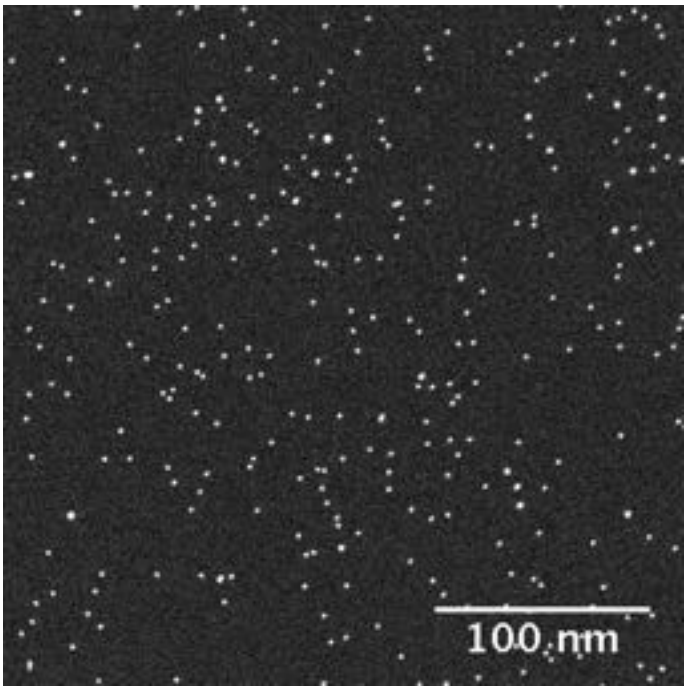

Figure 2.4: A HAADF STEM image of a typical Au_{561} cluster sample (amorphous carbon substrate). The deposition density used in this case was 0.2 clusters per $(10nm)^2$.

2.2 Sample Characterisation: Aberration Corrected STEM

For all imaging a JEOL2100F with spherical aberration corrector (CESOR) was employed, operated solely in STEM mode. Figure 2.5 shows a photograph of the instrument with some of the main components indicated, alongside a schematic ray diagram for the instrument in STEM mode.

A ZrO/W Schottky electron gun located at the top of the microscope column generates the electron beam and a series of acceleration tubes accelerate the beam to 200kV. The electron beam is then focused and collimated by the condenser lens system and aperture assembly before entering the aberration corrector optics. The aberration corrector removes the majority of the spherical aberration introduced by the condenser lenses and ultimately results in a resolution (probe size) of $\approx$ 1Å. Post-aberration corrector the pre-field objective lens forms the probe, which is rastered

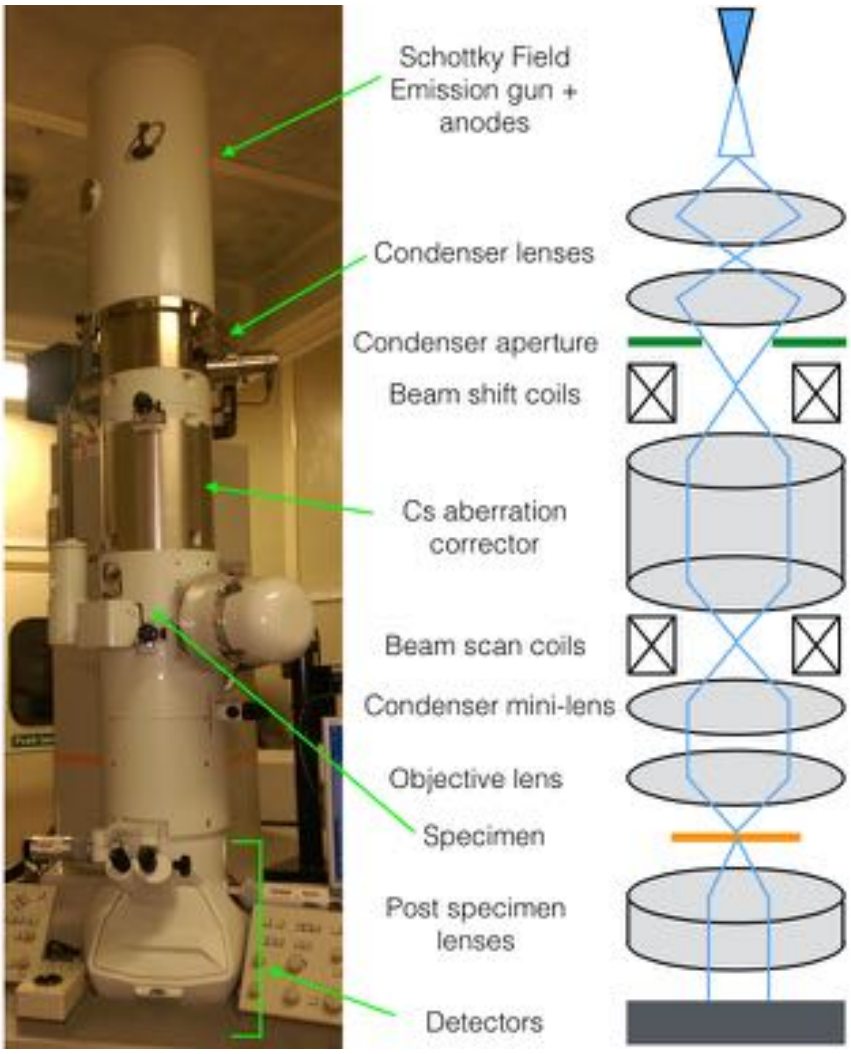

Figure 2.5: Key components of the JEOL 2100F aberration corrected STEM. A photograph of the instrument is on the left and a schematic ray diagram on the right.

across the sample by scan coils. BF, ADF, HAADF, EDX and EELS detectors are available for imaging and chemical analysis.

The vacuum system of the microscope is maintained by a selection of rotary, turbo, diffusion, and ion pumps. The electron gun chamber is maintained at 10^{-8} Pa to reduce contaminants on the gun's filament, whilst the rest of the microscope column is at $2{\times}10^{-5}$Pa. Figure 2.6 shows the valve status display for the microscope. This display shows a schematic of the microscopes pumps, valves, and gauges, alongside readings for the ion gauges. To further reduce contamination of the sample, an anti contamination device (cold trap) is employed, which must be

filled with liquid nitrogen prior to imaging.

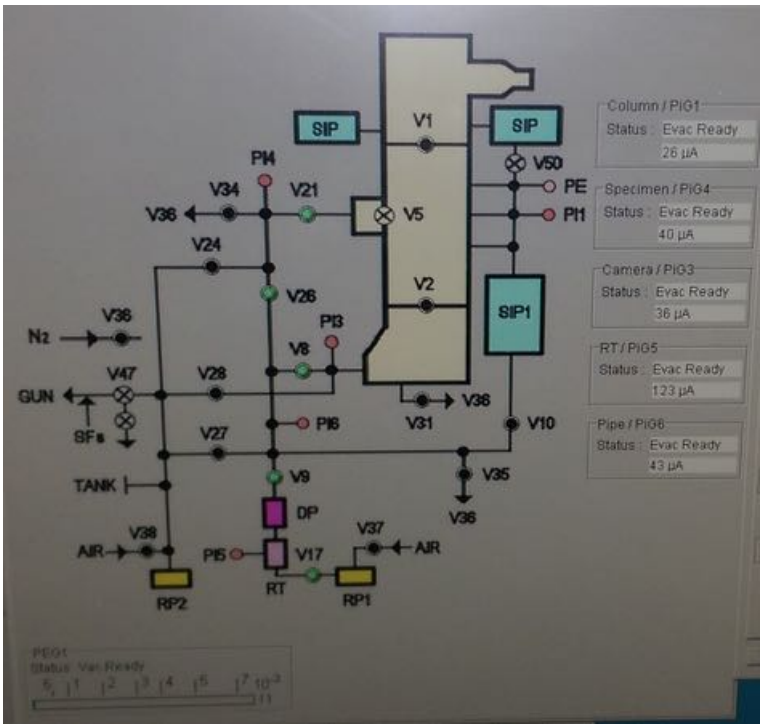

Figure 2.6: The valve status display for the JEOL 2100F, indicating the location of all valves, pumps and gauges. V: valve, PI: pirani guage, PE: penning gauge, RP: rotary pump, RT: turbomolecular pump, DP: diffusion pump and SIP: ion pump.

2.2.1 Practical Operation

Alignment

The resolution in the STEM is determined by the probe size. The probe size is ultimately determined by the aberrations of the electron lenses used to form the probe. Therefore, it is important to minimize aberrations prior to imaging, to ensure that atomic resolution imaging is possible and that fine details can be resolved. Initially, observing and correcting the Ronchigram provides a rough check of the aberration corrector alignment. The Ronchigram is a projection image of the specimen that can give an indication of the probe aberrations and of the aberration free portion of the probe [7]. Figure 2.7a shows a schematic of the Ronchigram formation. At under and over focus a shadow image of the specimen is seen, as the inflection point of the beam gets close to the sample plane, the magnification of the shadow image

increases. When the inflection point of the beam (the probe) is exactly in-line with the sample, the magnification is infinite and a pattern is seen, as shown in figure 2.7b. The size of the 'flat' region in the centre of the pattern gives a measure of the aberration free range of the probe (measure in mrad). The 'star' shape of the Ronchigram is a result of the double hexapole system of the spherical aberration corrector [8].

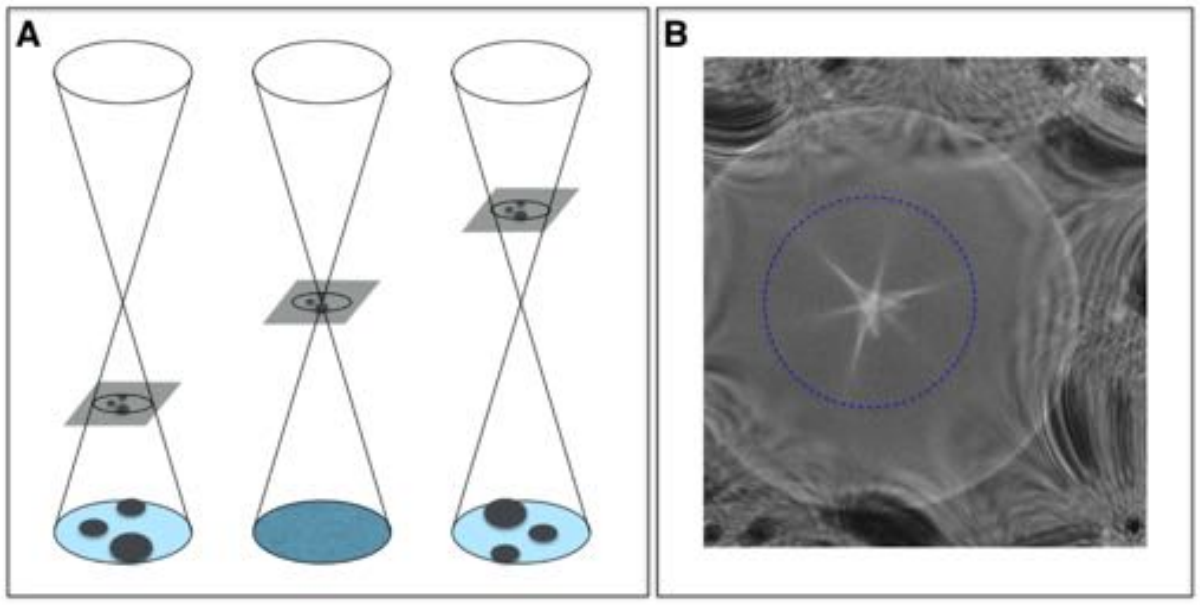

Figure 2.7: a) A schematic of the Ronchigram formation. b) An image of the ronchigram on the JEOL2100F instrument when the sample is in line with the inflection point of the electron beam. The blue dashed line indicates the flat, featureless region at the centre of the Ronchigram.

On a daily basis, whilst observing the Ronchigram the axial coma and 2-fold astigmatism can be corrected for. If after these corrections the flat region is very small or the pattern is not uniform, a full alignment of the aberration corrector must be performed. The full alignment of the aberration corrector is computer controlled; it is an iterative process that corrects for not only the spherical aberration but also the 'parasitic' aberrations induced by the corrector itself. Before starting a high density Au nanoparticle on a-carbon sample must be inserted. The software works by building a Zemlin tableau: a series of under and over focus images of a sample that enables the software to create an estimation of the probe shape and measure

the aberration free area of the probe. Figure 2.8 shows a screenshot of the CEOS software and the result of the Zemlin tableau. After each iteration of the Zemlin tableau, the software suggests which aberration should be corrected for, the user then accepts this suggestion (or choses another aberration to correct) and repeats the process until a reasonable value for the aberration free region is obtained.

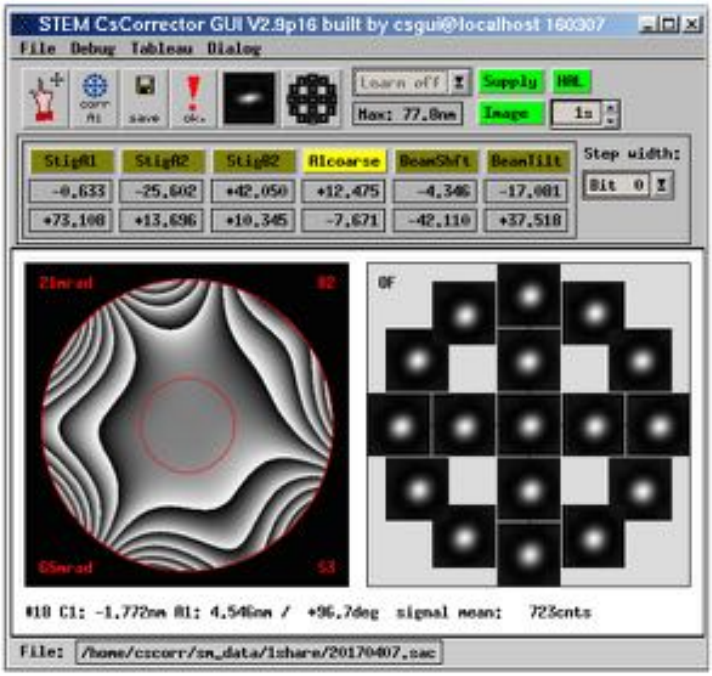

Figure 2.8: A screenshot taken from the CEOS GUI showing a calculated Zemlin tableau

Imaging

After alignment of the Ronchigram, a condenser aperture is inserted. This removes electrons scattered through large angles in the condenser lenses, collimating the beam. The aperture size inserted is chosen such that there is good resolution (less aberration), but still enough signal. For all imaging experiments in this thesis the 20μm aperture was used. The aperture is inserted such that it is aligned with the centre of the flat, featureless region of the Ronchigram (indicated in figure 2.7), this ensures that the coherent portion of the electron beam is used for imaging. For the majority of imaging performed in this thesis, a HAADF detector was employed. This is because it enables Z-contrast imaging; providing information on the

3D atomic structure of elemental clusters (when compared to simulations) [9] and determination of the size distribution in number of atoms. In cases where it was useful to observe lighter elements, the carbon substrate for example, a BF detector was used simultaneously with the HAADF detector. Figure 2.9 shows an example of a HAADF and a BF image of Au nanoparticles on a-carbon acquired simultaneously; the Au particles and Au single atoms are clearly visible in the HAADF image whilst the BF image shows the detail of the a-carbon substrate.

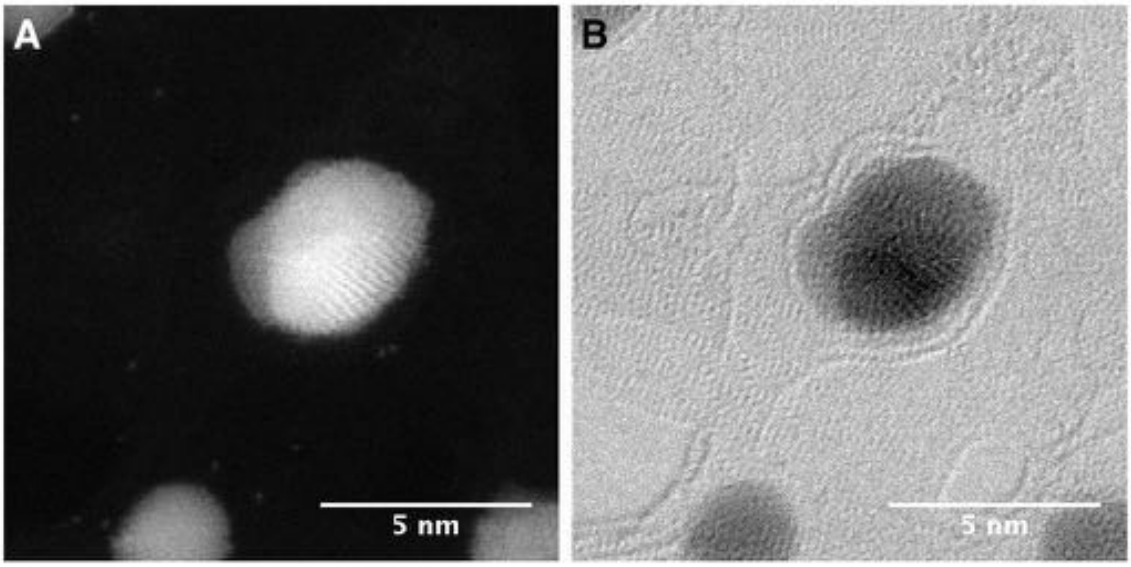

Figure 2.9: Au nanoparticles on amorphous carbon at 1000°C. a) A HAADF STEM image and b) a BF STEM image acquired simultaneously.

Throughout all experiments, a camera length of 10cm was used. The camera length refers to the effective distance between the sample and the detector; hence for an annular detector it controls the collection angle. For the HAADF detector used here, a 10cm camera length corresponds to an inner collection angle of 62mrad. This camera length was chosen because the corresponding inner collection angle means that Rutherford scattering will be dominant (criteria suggested is >50mrad [10]), but there will still be enough signal from the electrons scattered through high angles. During imaging the sample scan area is determined by the position of the sample stage (peizo controlled) and the magnification selected. The dwell time of the beam on each pixel can also be adjusted. A high dwell time will give more signal

but will also cause more damage to the sample; this may result in the structure of the sample changing during imaging or moving position. A lower dwell time will give a worse signal to noise ratio, however it is less damaging and faster, making it better suited for imaging beam sensitive materials. The imaging conditions used most commonly for the structural analysis work presented in this thesis are shown in table 2.3. This results in a dose of $4.2 \times 10^4 e^- / \text{Å}^2$/frame (see calculation of dose in appendix A). For video imaging of clusters a faster dwell time was regularly used and the magnification altered depending on the required dose.

Table 2.3: Standard imaging conditions used to collect atomic structure HAADF STEM data

Imaging condition	Standard value
Image size	15.74 × 15.74 nm
Pixels	512 × 512
Beam dwell time per pixel	20 μs
Dose	4.2×10^{-4} Å^{-1}frame^{-1}

Hydrocarbon contamination can cause serious degradation of images [11, 12, 13]. The electron probe attracts hydrocarbon molecules to the scan area resulting in a build up of hydrocarbons under the beam and loss of image quality. To solve this problem, a beam shower can be performed. A beam shower involves exposing a large area of the sample to a weak beam for 10-30 minutes to pin down the hydrocarbon molecules [11] and stop them building up under the electron beam. However, exposing a sample to the electron beam for a long period of time can also cause damage to the sample, so the sample should be monitored before and after to check for signs of damage (e.g. sputtered atoms from clusters). Beam showers were used to reduce the effects of contamination on many of the samples studied in this thesis. Where possible short beam showers were used and any effect was monitored. For silver clusters, which were particularly beam sensitive, beam showering was

avoided as much as possible and results discounted if the samples underwent any significant changes.

STEM-EELS Operation

The basic principle of STEM-EELS was explained in chapter 1. Here, the practical operation of STEM-EELS, and analysis of spectra will be described.

The JEOL2100F microscope used in this study is fitted with a Gatan Enfina EELS spectrometer. This is located directly below the microscope column. Prior to acquiring EELS spectra of a sample, the BF detector must be removed to allow the transmitted beam of electrons to enter the spectrometer and a suitable camera length selected.

The zero loss peak is then used to align the transmitted beam with the spectrometer. Focus is adjusted to obtain a narrow peak and the energy is shifted so that the centre of the zero loss peak is aligned with 0 eV. An example of a zero loss peak (obtained for a carbon nanotube and iron nanoparticle sample) is shown in figure 2.10. The width of the zero loss peak at its half maximum gives the energy resolution of the spectrum. For the instrument used here, the energy resolution is approximately 1eV.

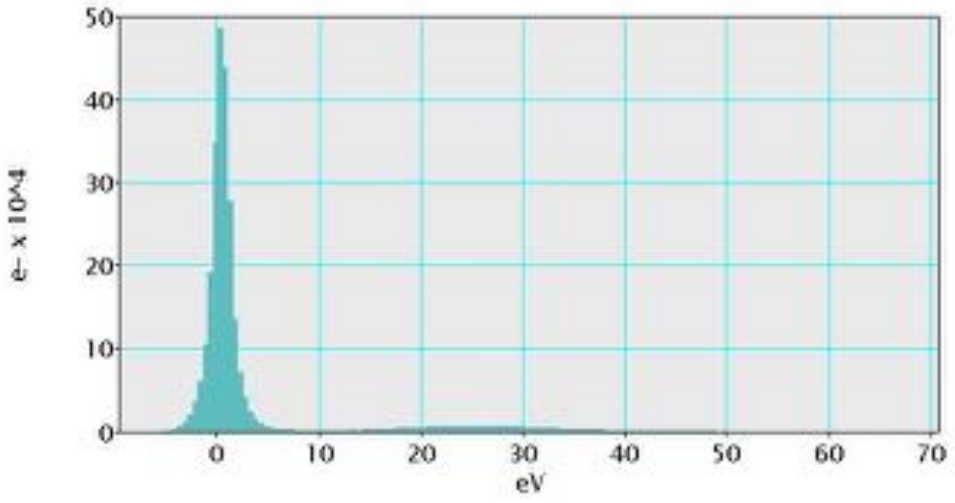

Figure 2.10: A typical example of the zero loss peak. Obtained for a carbon nanotube and iron nanoparticle sample.

For acquisition of spectra, a suitable energy range, aperture size and exposure time are selected. A larger aperture size will increase the signal but decrease spatial resolution. For the data collected in chapter 6 an aperture size of 3 mm and acquisition time of 1 second were used. To acquire a point spectra the beam is moved to the desired location and the spectra is recorded (using digital micrograph). For all EELS data collected in chapter 6 an average over 5 spectra was taken for each point. To record an EELS map the desired area of the sample is selected and the number of pixels and pixel dwell time are chosen. An EELS spectra is then recorded at each pixel to build up a spatial map of EELS spectra. For acquisition of maps it is particularly important that the sample has low drift, as the map acquisition requires much more time (>10 minutes). Automatic drift correction can be employed by selecting a well defined feature of the sample, however if the drift is too large this will not work.

All analysis of spectra presented in chapter 6 was performed using digital micrograph. Firstly, the edges in the core loss region of the spectrum are located with reference to known energies and features. The background is then subtracted for each edge using a power law background model [14]:

$$J(E) = AE^{-r} \tag{2.3}$$

where $J(E)$ is the (pre-edge) background, A is a scaling constant and r is exponent of the background (generally 2-6 [14]). The parameter fit (r, A) is performed in digital micrograph by selecting a suitable background window preceding the edge in question. The signal of the edge is then quantified by selecting a signal integration window that includes the main feature of the edge and is approximately 10% of the edge energy in width. For delayed edges (such as Ag), the start of the signal window should be offset slightly to include the main feature. The signal is then quantified by digital micrograph using the Hartree-Slater model [15] for calculation of the partial inelastic scattering cross section to obtain the relative proportion of various elements in the spectrum. Figure 2.11 shows a typical spectrum of an a-carbon substrate,

with the background subtraction and extracted carbon signal indicated.

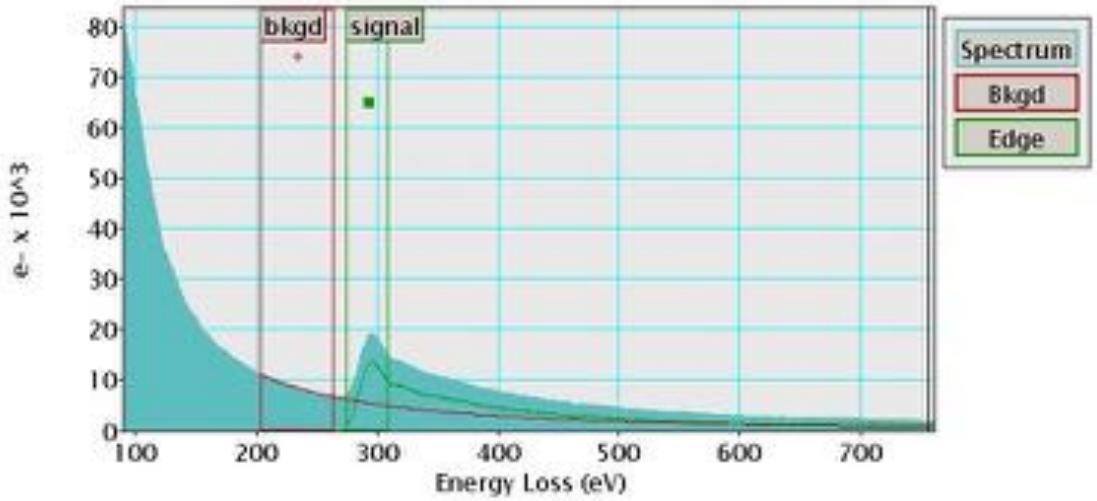

Figure 2.11: An EELS spectrum for a-carbon. The background and signal windows are indicated.

In-Situ Heating

For experiments conducted in chapters 4 and 5, a DENS solutions wildfire D6 heating holder was used in conjunction with DENS solutions MEMS heater-chips. This enabled in-situ heating of samples in the JEOL 2100F.

The heater-chips consist of a metal heater coil embedded in silicon nitride with imaging windows in-between. The imaging windows comprise of a thin ($\approx$ 5 nm for a-carbon, $\approx$ 20nm for a-silicon nitride), electron transparent film of either amorphous carbon or silicon nitride. A schematic of the chip design is shown in figure 2.12, with the heater coil and imaging windows indicated.

A 4 point probe system is used for resistive heating of the metal coil and measurement of its resistance. Figure 2.12 shows the electrical connections to the heater coil, two of the contacts provide a current to heat the coil, and the other two measure the voltage. This allows the resistance to be measured. The method provides an accurate measure of the resistance, unaffected by the contact or wire resistances. From the measured resistance the temperature can be deduced. This gives a live measurement of the temperature of the heater coil and allows feedback control of

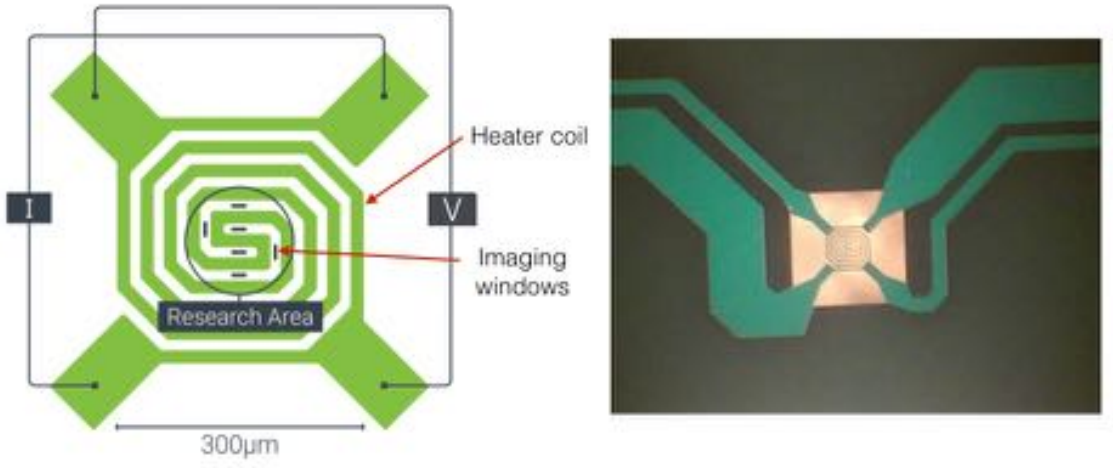

Figure 2.12: Left: a schematic of the DENS solutions heater chip design, indicating the electrical connections of the heater coil (for heating and 4-point probe measurement), the imaging windows and the research area in which the temperature uniformity is guaranteed. Figure adapted from reference 16. Right: a photograph of one of the DENS solutions XT heater chips used for heating experiments.

the applied heating current to maintain a steady temperature. The manufacturer calibrates each set of chips by measuring the resistance as a function of temperature. A calibration value is provided with the chips, which must be input into the heater software before starting the experiment.

For all experiments conducted in this thesis the DENS solution XT nanochips were used, which have a maximum temperature of 1300°C. Some general specifications of the XT-nanochips are shown in table 2.4.

Table 2.4: DENS solutions XT nano chip specifications [16].

Property	Value
Temperature range	Room temperature - 1300°C
Temperature accuracy	<5%
Temperature stability	<1°C at 1300°C
Heat/quench rate	200°C/ms
Resolution	Equivalent to that of the microscope
Settle time	<2s

Deposition of clusters onto the nanochips was performed in the same way as described above for a TEM grid, ensuring that the heater coil was aligned with the centre of the mask. This resulted in clusters being uniformly deposited over the entire central region of the nanochip.

For all experiments performed with the heating holder, the temperature was set manually on the digiheater software, which creates a log file of temperature versus time. When the temperature was increased or decreased the specimen height and/or focus were adjusted prior to recording images. This was to negate the bulgeing/contraction of the chip, as the temperature is increased/decreased.

For results collected in chapter 4, the temperature was increased incrementally; at each temperature a large number of clusters (≈100) were imaged to determine the relative proportion of atomic structures. For results collected in chapter 5, the temperature was increased incrementally and the same group of clusters was imaged to determine the surface melting temperature. To keep track of the particles as the temperature was increased (and to reduce the effect of the electron beam), a lower magnification was used whilst adjusting the temperature (1M×, 157.41×157.41nm field of view) than whilst imaging (10M×, 15.74×15.74 nm field of view). Focusing was also performed on a different area to ensure that the electron beam did not have too large of an effect on the sample. For analysis of both these data sets, the digiheater log file was referred to and each recorded image was assigned a specific temperature.

2.3 Sample Transfer in Inert Gas

For transfer of samples in inert gas between the cluster source and the microscope, a specially designed glovebox was used. Figure 2.13 shows a labelled picture of the glovebox; one side is attached to the loadlock of the cluster source via a gate valve and the other side opens to air for tools to be inserted. Two valves allow argon gas to flow into and out of the box.

The procedure for transferring samples between the cluster source and the microscope is as follows. All relevant tools and the STEM sample holder are inserted into the box. Argon is then allowed to flow through for several minutes to flush air from inside. The outlet valve is closed and the loadlock of the cluster source is vented with argon through the glovebox by opening the gate valve. A specially designed tool is used to retrieve the sample, which is inserted into the STEM holder. The glovebox is then disconnected from the loadlock and taken to the STEM lab. Throughout, the glovebox is over pressured with argon. The side is then opened and the sample holder inserted into the microscope. At this point the sample is exposed to air for a couple of seconds.

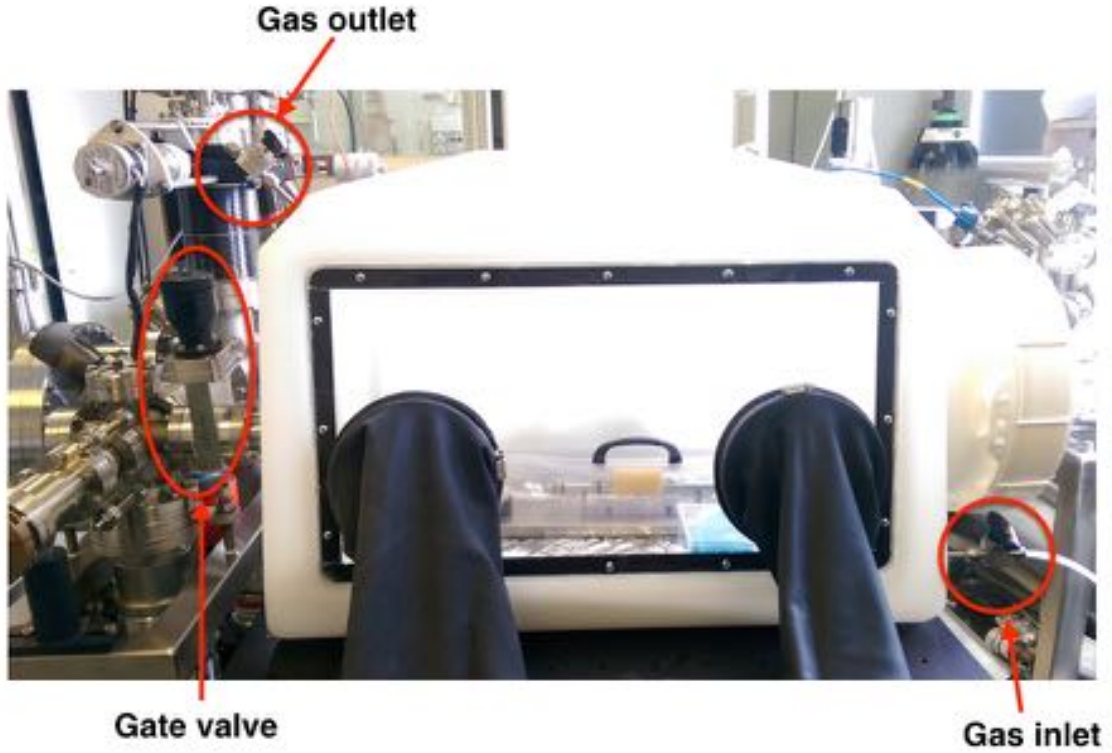

Figure 2.13: A labelled photograph of the specially designed glove box used to transfer samples from the magnetron cluster source to the STEM. The gate valve indicated connects the glove box to the load lock of the magnetron cluster source.

2.4 Image Analysis

2.4.1 Identification of Atomic Structure: Simulation Atlas Method

To determine the atomic structure of the size-selected clusters investigated in this thesis, HAADF STEM images of individual clusters were compared with simulated HAADF STEM images of model structures. Simulations were performed by Ray Hu, using QSTEM software [17]. The parameters used for the simulations are shown in table 2.5. The QSTEM software enables simulation of STEM (including HAADF)

Table 2.5: Parameters used in the QSTEM simulations of cluster structures (simulations performed by Ray Hu (Laboratory of Solid State Physics and Magnetism, University of Leuven).

Parameter	Value
High voltage	200kV
Defocus	-1.9nm
Astigmatism	0nm
Spherical aberration	0.001mm
Temperature	300K
Chromatic aberration	1.0mm
Beam energy spread, dE	1eV
Convergence angle	19mrad
Inner detector angle	62mrad
Outer detector angle	164mrad

images using a multislice algorithm [18]. A model is input along with the electron microscope properties (for example inner and outer detector angles, energy spread of the source and spherical aberration), and the electron scattering is calculated. The multislice method works by dividing the model in to a number of thin slices

perpendicular to the beam direction. Each slice is projected onto a single plane, this is called the projected potential of the slice. The amplitude and phase of the incident electron beam passing through the first projected potential are calculated. The scattered beams are then propagated through free space to the second projected potential and so on. The scattered electron wave is a convolution of the electron probe wavefunction multiplied by a transfer function, and the projected potential. [10]

As discussed in chapter 1, metal clusters generally present one of 3 structural motifs: TO, Dh or Ih. The majority of cluster sizes investigated in this thesis are magic numbers (309, 561, 923) meaning that the number of atoms corresponds to a geometrical shell closing for the cuboctahedron (fcc), Ino-Decahedron (Dh) and Icosahedron (Ih). For this reason geometrical models of the cuboctahedron, Ino-decahedron and icosahedron were used to create a simulation 'atlas' in which a complete range of the cluster rotation angles are simulated. Figure 2.14 shows the simulation atlas used for identification of Au_{561} structures. HAADF STEM images obtained of clusters were compared by eye against the simulation atlas images to identify the atomic structures. Clusters were classified more generally as Icosahedron, decahedron or fcc; these classifications include all various truncations of decahedra and fcc type structures. For example a decahedron with a Marks-type re-entrance is classified generally as a decahedron. Clusters that could not be matched to the atlas images were classified as unidentified or amorphous (UI/A). Figure 2.14 shows several examples of experimental HAADF STEM images matched to simulation atlas images.

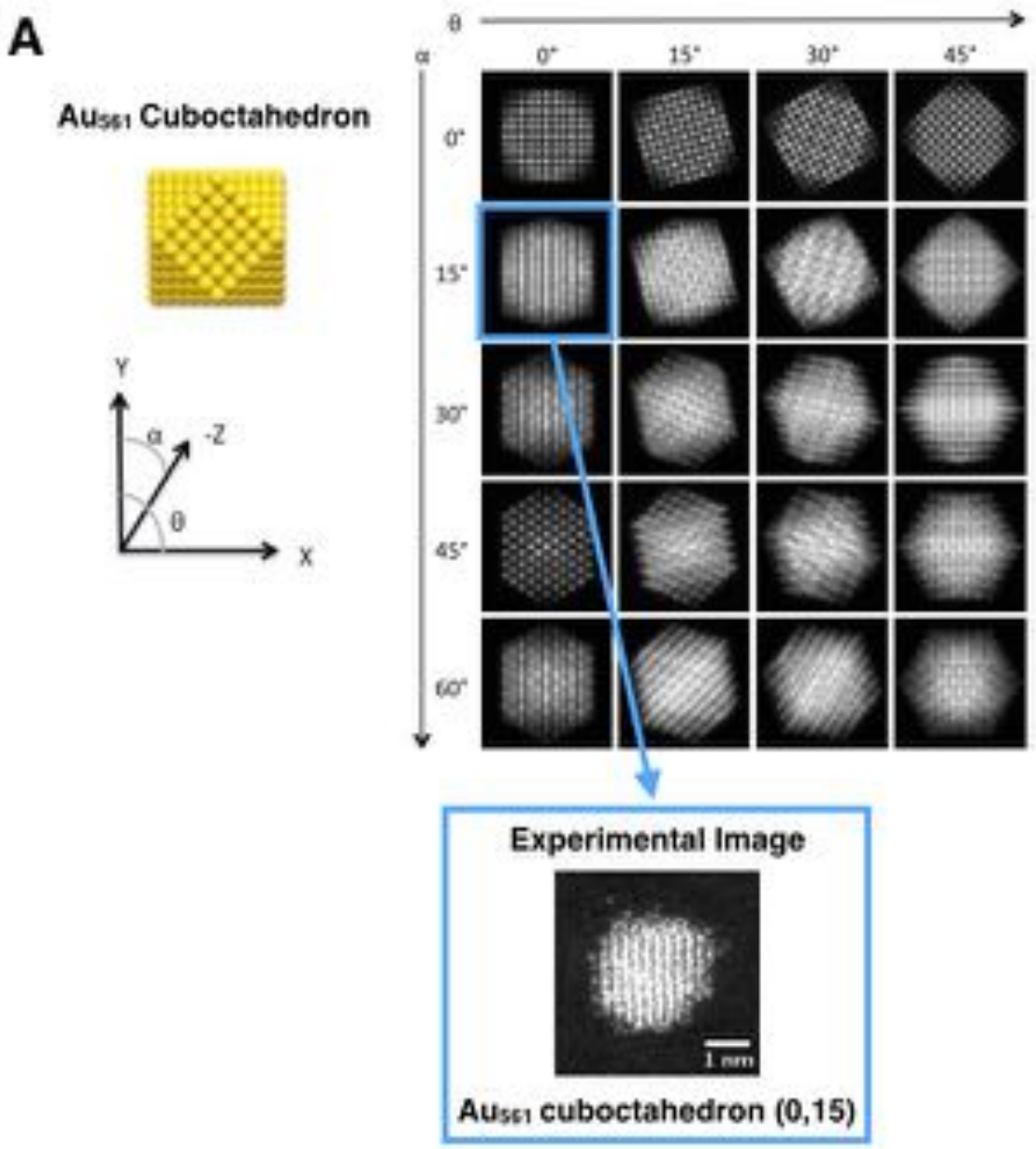

(a) The cuboctahedron atlas

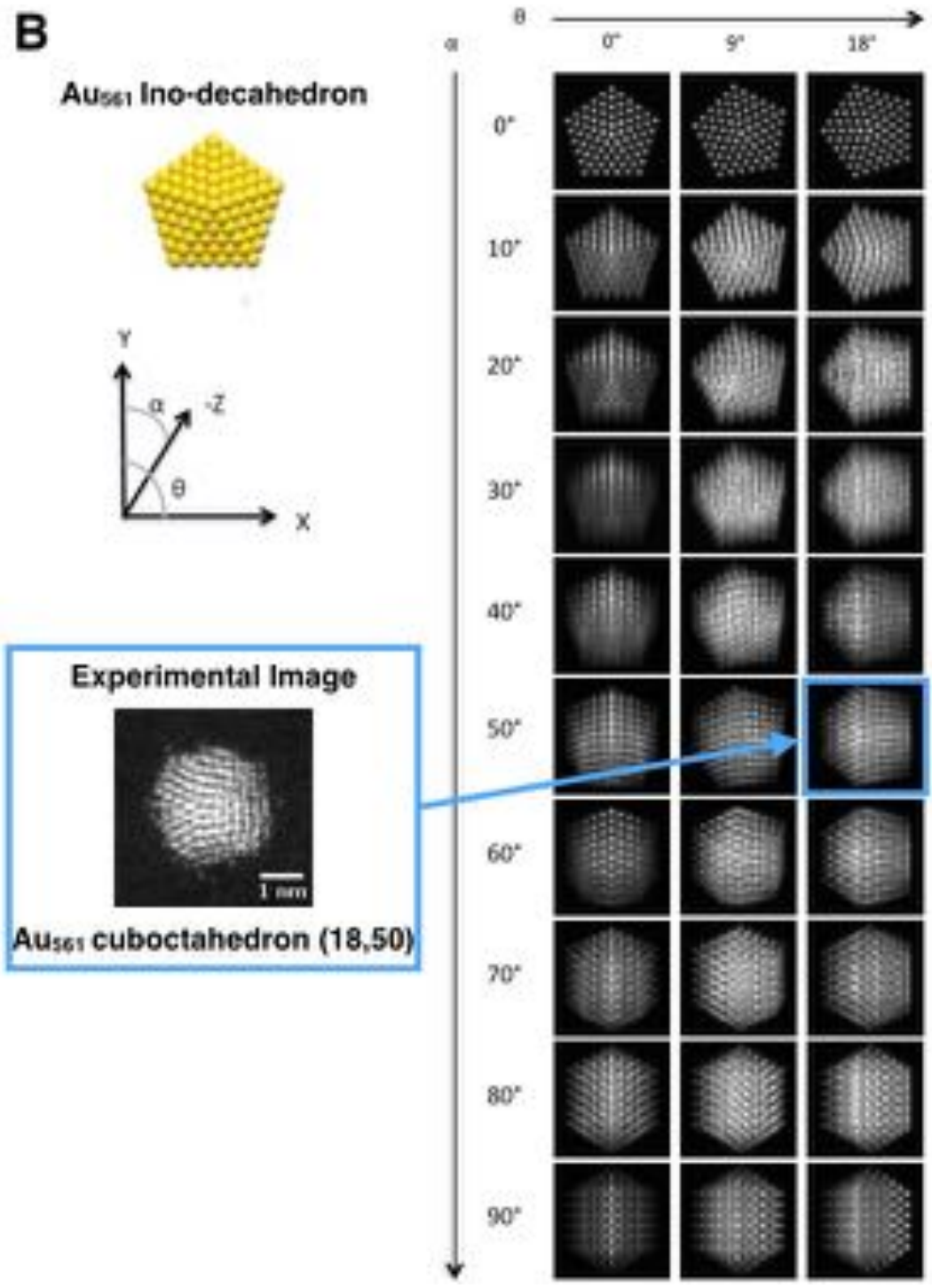

(b) The Ino-decahedron atlas

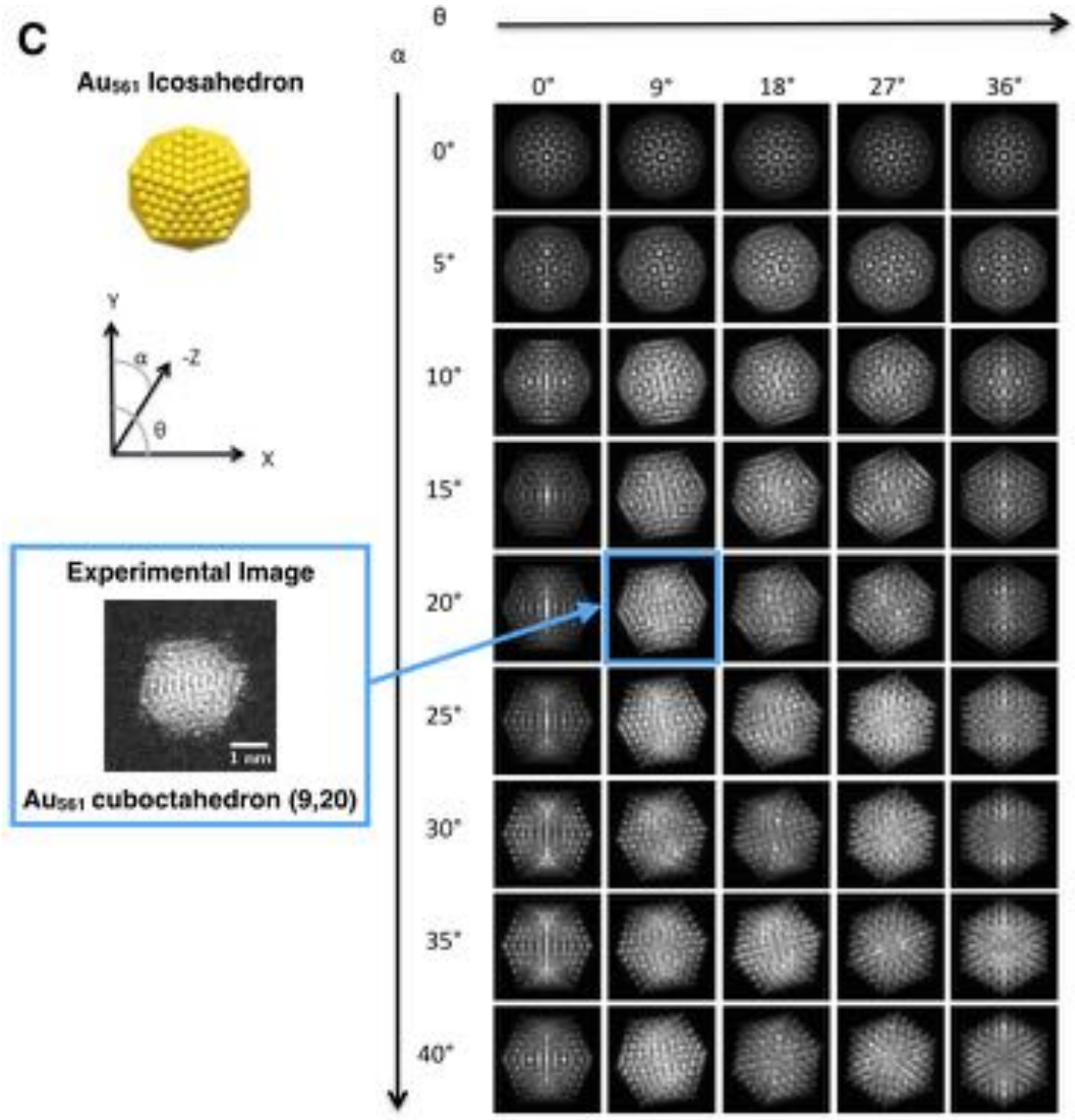

(c) The icosahedron atlas

Figure 2.14: The Au_{561} simulation atlas with experimental image matches indicated.

2.4.2 HAADF Intensity Measurement

As discussed in chapter 1, HAADF intensity is proportional to Z^n [19]. Moreover, for an elemental material, it has been shown that the relationship between HAADF intensity and number of atoms is linear up to approximately 6000 atoms (for approximately spherical particles) [20]. This can be useful for determining the size distribution of samples, particularly if used in combination with size-selected ele-

mental clusters. There are three key ways that HAADF intensity can be used to gain information on the size distribution of samples, all of which are detailed below.

1. Size distribution of size-selected clusters

For samples of size-selected clusters, measurement of the HAADF intensity can give the size distribution. The lateral time of flight mass filter used to size-select the clusters has a resolution dependent on the entrance and exit aperture sizes (as described in section 2.2). Measuring the HAADF intensity of a large number of these clusters, producing a histogram and assuming the peak (of a gaussian fit) is at the size selected by the mass filter, the distribution can be represented in terms of number of atoms. The FWHM of a Gaussian fit to the data gives an indication of the size distribution of these clusters, which can be compared with the theoretical size distribution based on the TOF settings. Figure 3.1 in chapter 3 shows an example of a typical size distribution of a Au_{561} size-selected cluster sample calculated in this way.

2. Size-selected clusters as mass balances

Size-selected clusters can be used as mass balances to determine the number of atoms in nanoparticles of an unknown size [20, 21, 22, 23]. For this analysis to work the atomic number of the 'unknown mass' nanoparticles must be known and the particles must consist of a single element. Size-selected clusters are prepared on a TEM grid and the nanoparticle of unknown mass is co-deposited. The HAADF intensity of the size-selected clusters and the nanoparticle of unknown mass are then be measured. The ratio of intensities of two (single element) nanoparticles is given by [19]:

$$\frac{I_1}{I_2} = \frac{N_1}{N_2}\left(\frac{Z_1}{Z_2}\right)^{\alpha} \tag{2.4}$$

where $I_{1/2}$ is the intensity of the size-selected cluster/nanoparticle of unknown mass, $N_{1/2}$ is the number of atoms in the size-selected cluster/nanoparticle, $Z_{1/2}$ is the atomic mass of the size-selected cluster/nanoparticle, and α is the exponent relating HAADF intensity to atomic number for a given camera length [19, 24]. Rearranging this equation enables the number of atoms in the nanoparticle to be calculated so

long as the exponent, α is known for the chosen camera length.

3. Atom counting

The number of atoms in an elemental nanoparticle can also be determined by measuring the HAADF intensity of single atoms of the same element [25, 26]. In this case, a large number of single atoms should be measured to determine the HAADF intensity corresponding to a single atom (and the associated error from the FWHM of the distribution). The number of atoms in a given nanoparticle of the same element can then be determined simply by measuring its HAADF intensity and dividing this by the HAADF intensity of a single atom.

For the results presented in this thesis, method 1 was regularly used to check the size distribution of samples and method 2 was used to determine the size of unknown aggregate particles in chapter 5. Method 3 was also used in several cases to confirm that the number of atoms was as expected from the size-selected cluster samples.

To measure the HAADF intensity of an individual cluster, an imageJ macro was used to integrate the intensity of an area including the cluster and subtract the background intensity. Figure 2.15 shows a schematic of the intensity measurement. Initially a threshold is applied to the image to determine the location of the clusters. Two concentric rings, of radius r_1 and r_2, are then drawn around each cluster. The intensity, I_1, of the area A_1 and the intensity, I_2, of the ring A_2 are measured. The intensity of the background, I_3 is then calculated by:

$$I_3 = \frac{I_2 A_1}{A_2} \tag{2.5}$$

and subtracted from the total intensity I_1 to give the cluster intensity, I_c:

$$I_c = I_1 - I_3 = I_1 - I_2 \frac{A_1}{A_2}. \tag{2.6}$$

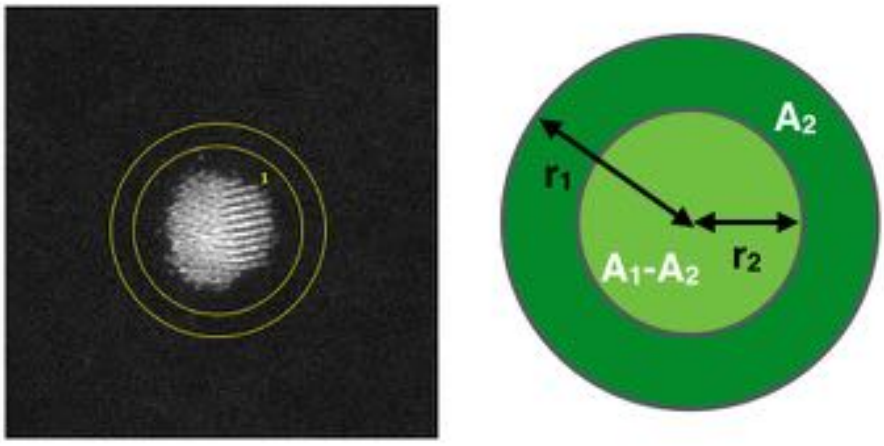

Figure 2.15: A schematic of the HAADF intensity measurement, to be viewed alongside equations 2.5 and 2.6. On the left hand side is a HAADF STEM image of a cluster with two rings of radius r_1 and r_2 drawn around it for measurement of the HAADF intensity. On the right hand side is a schematic of the rings and associated areas used for the HAADF intensity measurement. A_2 is the area of the dark green ring, A_1 is the area associated with the largest circle (radius r_1), and the inner circle (radius r_2) has an area given by A_1-A_2.

Generally, the variation in the intensity of the background is negligible; it is approximately 1% of the intensity of a single atom, provided that the sample is free from contamination during imaging. If images are taken at different magnifications, contain a different number of pixels, or have different acquisition times, the HAADF intensity has to be calibrated. Equation 2.7 gives the conversion between intensities for images taken with different conditions.

$$I = \frac{M^2 \times P_x \times P_y \times t}{M_0^2 \times P_{x0} \times P_{y0} \times t_0} \times I_0 \tag{2.7}$$

Where I_0 is the intensity of an image taken at magnifiation M_0, with $P_{x0} \times P_{y0}$ pixels and a dwell time t_0, and I is the equivalent intensity if the image is taken at magnification M, with $P_x \times P_y$ pixels and a dwell time of t.

References

[1] S Pratontep, S J Carroll, C Xirouchaki, M Streun, and R E Palmer. Size-selected cluster beam source based on radio frequency magnetron plasma sputtering and gas condensation. *Review of Scientific Instruments*, 76(4):045103, 2005.

[2] B von Issendorff and R E Palmer. A new high transmission infinite range mass selector for cluster and nanoparticle beams. *Review of Scientific Instruments*, 70(12):4497, 1999.

[3] S J Carroll, S Pratontep, M Streun, R E Palmer, S Hobday, and R Smith. Pinning of size-selected Ag clusters on graphite surfaces. *The Journal of Chemical Physics*, 113(18):7723, 2000.

[4] M Di Vece, S Palomba, and R Palmer. Pinning of size-selected gold and nickel nanoclusters on graphite. *Physical Review B*, 72(7):073407–1–4, 2005.

[5] R Smith, C Nock, S Kenny, J Belbruno, M Di Vece, S Palomba, and R Palmer. Modeling the pinning of Au and Ni clusters on graphite. *Physical Review B*, 73(12):125429, 2006.

[6] A Abdela. *Gas phase generation and deposition of size-selected metal clusters*. PhD thesis, University of Birmingham, 2013.

[7] JEOL. Glossary of TEM Terms, Keywords 'Ronchigram'.

[8] Mark P Oxley, Andrew R Lupini, and Stephen J Pennycook. Ultra-high resolution electron microscopy. *Reports on Progress in Physics*, 80:24, 2017.

[9] Z Y Li, N P Young, M Di Vece, S Palomba, R E Palmer, A L Bleloch, B C Curley, R L Johnston, J Jiang, and J Yuan. Three-dimensional atomic-scale structure of size-selected gold nanoclusters. *Nature*, 451(7174):46–8, 2008.

[10] D B Williams and C B Carter. *Transmission Electron Microscopy*. Springer, 2009.

[11] A Ennos. The origin of specimen contamination in the electron microscope *. *British Journal of Applied Physics*, 101, 1953.

[12] A Ennos. The sources of electron-induced contamination in kinetic vacuum systems This. *British Journal of Applied Physics*, pages 217–234, 1953.

[13] A J V Griffiths and T Walther. Quantification of carbon contamination under electron beam irradiation in a scanning transmission electron microscope and its suppression by plasma cleaning. In *Journal of Physics: Conference Series*, volume 241, 2010.

[14] R F Egerton. *Electron energy-loss spectroscopy in the electron microscope*. Springer US, 2011.

[15] H. P. Hanson, F. Herman, J. E. Lea, and S. Skillman. HFS atomic scattering factors. *Acta Crystallographica*, 17(8):1040–1044, 1964.

[16] DENSsolutions. Nanochip, MEMS-based technology.

[17] C Koch. *Determination of core structure periodicity and point defect density along dislocations*. PhD thesis, Arizona State University, 2002.

[18] E J Kirkland. *Advanced computing in electron microscopy*. Plenum Press, 1998.

[19] Z W Wang and R E Palmer. Intensity calibration and atomic imaging of size-selected Au and Pd clusters in aberration-corrected HAADF-STEM. *Journal of Physics: Conference Series*, 371:012010, 2012.

[20] N Young, Z Li, Y Chen, S Palomba, M Di Vece, and R E Palmer. Weighing supported nanoparticles: size-selected clusters as mass standards in nanometrology. *Physical Review Letters*, 101(24):246103, 2008.

[21] M M J Treacy and S B Rice. Catalyst particle sizes from Rutherford scattered intensities. *Journal of Microscopy*, 156(2):211–234, 1989.

[22] A Singhal, J C Yang, and J M Gibson. STEM-based mass spectroscopy of supported Re clusters. *Journal of Microscopy*, 67:191–206, 1996.

[23] Judith C Yang, Steven Bradley, and J Murray Gibson. The oblate morphology of supported PtRu$_{5}$ on carbon black. *Materials Characterization*, 51:101–107, 2003.

[24] Z W Wang, Z Y Li, S J Park, A Abdela, D Tang, and R E Palmer. Quantitative Z-contrast imaging in the scanning transmission electron microscope with size-selected clusters. *Physical Review B*, 84(7):073408, 2011.

[25] Z W Wang, O Toikkanen, F Yin, Z Y Li, B M Quinn, and R E Palmer. Counting the atoms in supported, monolayer-protected gold clusters. *Journal of the American Chemical Society*, 132(9):2854–2855, 2010.

[26] Z W Wang and R E Palmer. Mass spectrometry and dynamics of gold adatoms observed on the surface of size-selected Au nanoclusters. *Nano letters*, 12:91–5, 2012.

Chapter 3

Atomic Structure and Gas Phase Growth of Size-Selected Au Clusters

In this chapter results on the atomic structure and growth of clusters containing 309, 561 and 742 atoms are presented. A magnetron sputtering gas aggregation cluster source with LTOF mass filter was used for production of size-selected clusters and samples were characterised using HAADF ac-STEM. In section 3.1 the gas phase growth mechanism of Au clusters between 561 and 923 atoms is investigated and for size 561 the relative stability of competing structural isomers is determined by electron beam manipulation experiments. The majority of these results are published in reference 1. In section 3.2 the effect of condensation length on the gas phase growth of Au_{309} clusters is considered and electron beam manipulation experiments are used to determine the ground state structure at this size.

Production of size-selected cluster samples, STEM imaging, and structural analysis was performed by the author. The simulation atlases used to identify the atomic structure of clusters were created by Ray Hu (Laboratory of Solid State Physics and Magnetism, University of Leuven) using the QSTEM software, structural assignments in section 3.1 were double checked by Ray Hu and Alex Pattison

(NPRL, University of Birmingham), and the molecular dynamic simulations of cluster growth presented in sections 3.1 and 3.2 were performed by Guilia Rossi and Riccardo Ferrando (INFM and IMEM/CNR, University of Genoa).

3.1 Metastability and Growth of Size-Selected Au Clusters

3.1.1 Methods

For this work size-selected Au clusters were produced using a magnetron sputtering gas aggregation cluster source [2] with a lateral time of flight mass filter [3] operated at a resolution of M/ΔM=22 (ΔM=FWHM). In all cases the clusters were produced using slow growth conditions: long condensation length (250mm) and low magnetron power (10W), with the aim of reducing kinetic trapping [4]. The pressure in the condensation chamber and Ar and He gas flows were also kept constant. This was important because all of these factors have the potential to alter the growth, hence atomic structure of the resultant clusters. Clusters containing 561±13 atoms and 742±17 atoms (error given by ±HWHM) were deposited on amorphous carbon coated TEM grids for imaging with HAADF STEM. The atomic structure of the clusters were then determined by comparison with simulation atlases of the cuboctahedron, Ino-decahedron and Mackay Icosahedron (see methods for more details). Size 561 was chosen because it is a magic number and size 742 was chosen because it lies directly between magic number sizes 561 and 923 (for which there is previously published data [4]) and so could give information on the growth mechanism.

3.1.2 Results and Discussion

Figure 3.1 shows a histogram of the HAADF intensity of a typical Au_{561} sample, measured using the background subtraction method (discussed in chapter 2). The HAADF intensity is proportional to the number of atoms [5], hence figure 3.1 can

be considered a size distribution. Assuming that the main peak is representative of Au_{561}, a standard deviation of 8% is determined from the gaussian fit. This value is larger than the 5% expected from the mass filter, which is likely due to error in the HAADF intensity measurement. This may be a result of errors in the HAADF intensity measurement resulting from and uneven background (used for background subtraction) or inclusion/exclusion of single atoms surrounding the cluster. Another possibility is that the cluster beam entering the LTOF mass filter is not convergent, and diverges such that the beam profile is larger than the entrance aperture - the calculated resolution uses the entrance aperture size as an estimation of the beam profile at the exit aperture. The subsequent peaks represent dimers and trimers that may be a result of aggregation or double/triple mass, double/triple charge clusters transmitted through the mass filter. Structural analysis was only performed for clusters within the first (Au_{561}) peak.

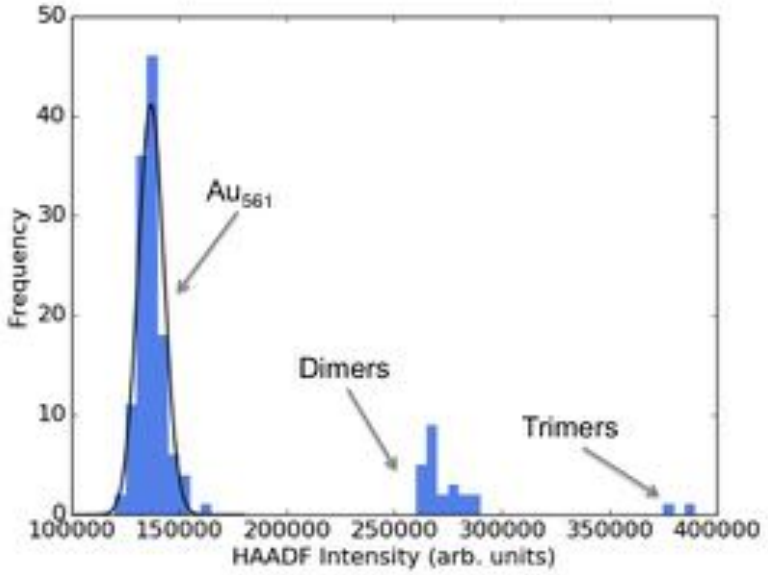

Figure 3.1: Size distribution of a deposited Au_{561} sample measured by HAADF STEM. The HAADF intensity (proportional to the number of Au atoms) of 149 clusters is plotted as a histogram. Peaks representing monomers, dimers and trimers are indicated.

Figure 3.2 shows typical HAADF STEM images of Au_{561} clusters matched by eye to multislice electron scattering simulations [6]; the experimental images are

on the top and the corresponding simulated images are underneath. (a, f) shows a Mackay icosahedron at a (27, 5) rotation, (b, g) a cuboctahedron at a (15, 60) rotation, (c, h) an Ino-decahedron at a (0, 0) rotation and (d, i) a decahedron at a (18, 10) rotation. The rotation angles of the clusters can be found in chapter 2. Not all clusters can be matched to the simulations, e) shows and example of a cluster that is amorphous.

The multislice simulations are performed for the cuboctahedron, Ino-decahedron and Mackay icosahedron for which 561 is a magic number. In reality the clusters produced have a finite size distribution (≈5%) and so many variations on these structures will exist; including different truncations and partial facets. Therefore, when matching the experimental images to the simulation atlas images, it is the core atomic structure that is focused upon and the atomic structure of the clusters are identified generally as fcc, Dh, Ih. This is even more pertinent when identifying Au_{742} structures, because it is not a magic number size. Structures that do not fall into any of these categories, including clusters that have no observable structure, are classified as unidentified/amorphous (UI/A).

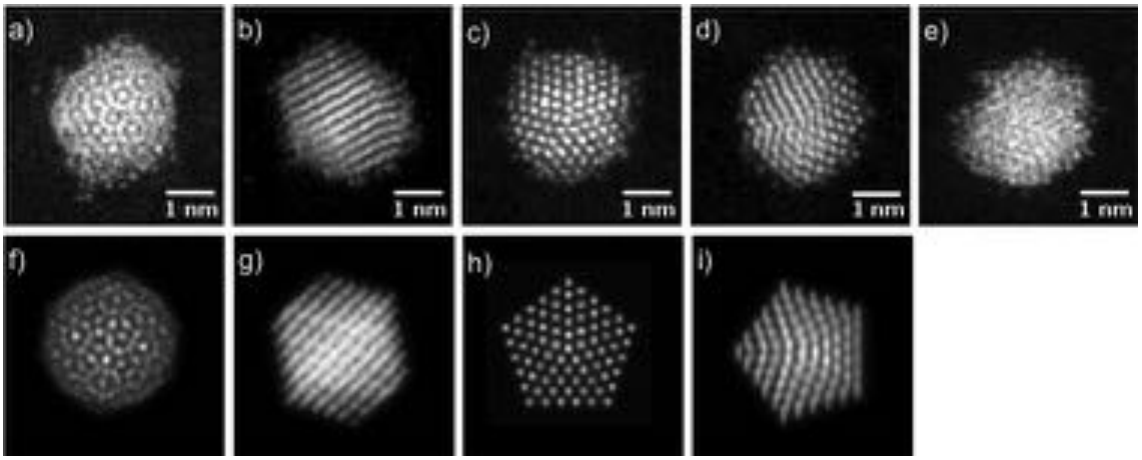

Figure 3.2: HAADF STEM images and corresponding electron scattering simulations [6] for Au_{561} clusters. (a)-(e) show HAADF STEM images of Au_{561} clusters with corresponding electron scattering simulations in (f)-(i). The specific orientations (θ,α) of the model clusters used in the simulated images are given in chapter 2. The clusters shown in (c) and (d) both show signs of re-entrant facets, indicating a Marks-decahedron structure. Adapted figure and caption from reference 1.

Figure 3.3 shows the proportions of structural isomers for Au_{561} and Au_{742} compared with results for Au_{923} from reference 4 (averaged from 2 sets of data presented at 250mm condensation length, 10 W magnetron power). This is based on 189 clusters for Au_{561} and 147 clusters for Au_{742}. In all cases the same slow growth formation conditions were employed. For Au_{561} the Dh is the dominant isomer (43%), in close competition with fcc (36%), whilst very few Ih were observed (2%). Similarly, for Au_{742} 46% of clusters were Dh, 37% fcc and 3% Ih and for Au_{923} 41% were Dh, 31% fcc and 4% Ih. The proportions of structural isomers for these three different sized clusters are almost identical: the ratios of fcc to Dh isomers for Au_{561}, Au_{742} and Au_{923} are 0.83±0.16, 0.79±0.18 and 0.74 respectively. The errors stated are based on statistical counting errors.

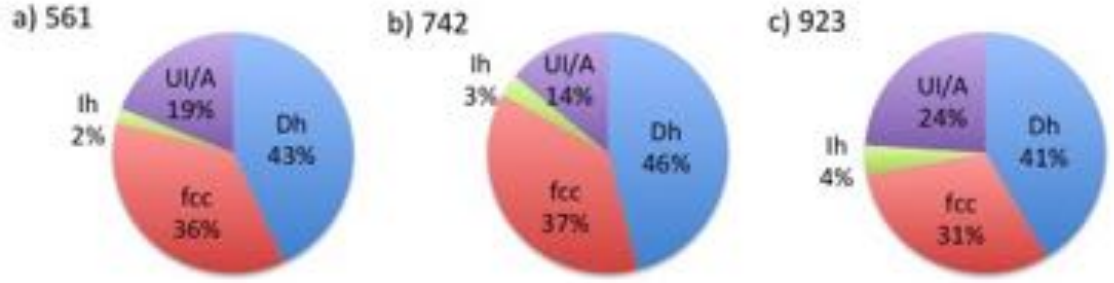

Figure 3.3: Percentages of structures observed for Au_{561} and Au_{742} compared with Au_{923}. (a)-(c) show the percentage of structures observed for Au_{561} and Au_{742} compared with Au_{923} [4]. Clusters are classified as face-centered-cubic (fcc), Decahedron (Dh), Icosahedron (Ih) or unidentified or amorphous (UI/A). The magnetron power, 10W, and condensation length, 250 mm, were the same in all cases. For Au_{561} 189 clusters were imaged, for Au_{742} 147 clusters were imaged. Figure and adapted caption from reference 1.

There are three possible explanations for why the same proportion of structural isomers are observed at these three different sizes. Firstly, if the clusters are assumed to be in equilibrium, then the obvious conclusion is that the Dh is the lowest energy structure, followed by fcc, with Ih being much higher in energy. Assuming this is the case, there must be no size dependence on the atomic structure between 561

and 923 atoms, otherwise the proportion of structural isomers would not be equal at all three sizes. This seems unlikely based on the literature of size dependent atomic structure [7, 8, 9, 10]. Another possibility is that the finite size range of the clusters studied results in both ground state Dh and fcc structures being present; it has been predicted by Goedecker et al [11] that the addition of just one atom can alter the ground state structure. In this scenario the Dh and fcc must be in close competition over the size range, and it is purely coincidental that the proportions of isomer are almost identical. The third explanation is that, despite slow growth conditions, the clusters are kinetically trapped during growth in the condensation chamber. Beyond a certain size the clusters will not have enough energy to rearrange to the ground state structure, hence they become trapped and continue to grow on a smaller, stable, seed structure - template growth. This growth mechanism is widely predicted for metal clusters [12, 13, 14, 15]. To investigate this further electron beam manipulation experiments were performed, which show that the clusters observed are not in equilibrium but are kinetically trapped. These results are presented below.

Table 3.1: Results of electron beam irradiation experiments on Au_{561} clusters. The frequency of structural transformations from an initial state to a final state, and in one case an intermediate state, is shown. Videos were recorded at a dose of 1.4-3.1$\times 10^4$ e^- per Angstrom^2 per frame for a minimum of 50 frames, field of view 15.74 $\times$ 15.74nm or 13.12 $\times$ 13.12nm

Initial State	Intermediate State	Final State	Frequency
Dh	-	fcc	17/19
Dh	-	Dh	2/19
fcc	-	fcc	13/15
fcc	Dh	fcc	2/15

Table 3.1 shows the result of electron beam manipulation experiments on Au_{561} clusters. These experiments were performed by continually imaging individual clusters (for a minimum of 50 frames with an acquisition time of 2.9 seconds per frame

and a dose of 1.4-3.1×10^4 e^- per Angstrom^2 per frame) and observing the resultant structural transformations, 'video imaging'. For clusters that were initially decahedral, 17/19 transformed to fcc and 2/19 remained decahedral. For clusters that were initially fcc, 13/15 remained fcc whilst 2/15 briefly transformed to an intermediate decahedral structure before transforming back to fcc. Figure 3.4 shows two examples of a Dh cluster transforming to fcc due to the irradiation of the electron beam during imaging.

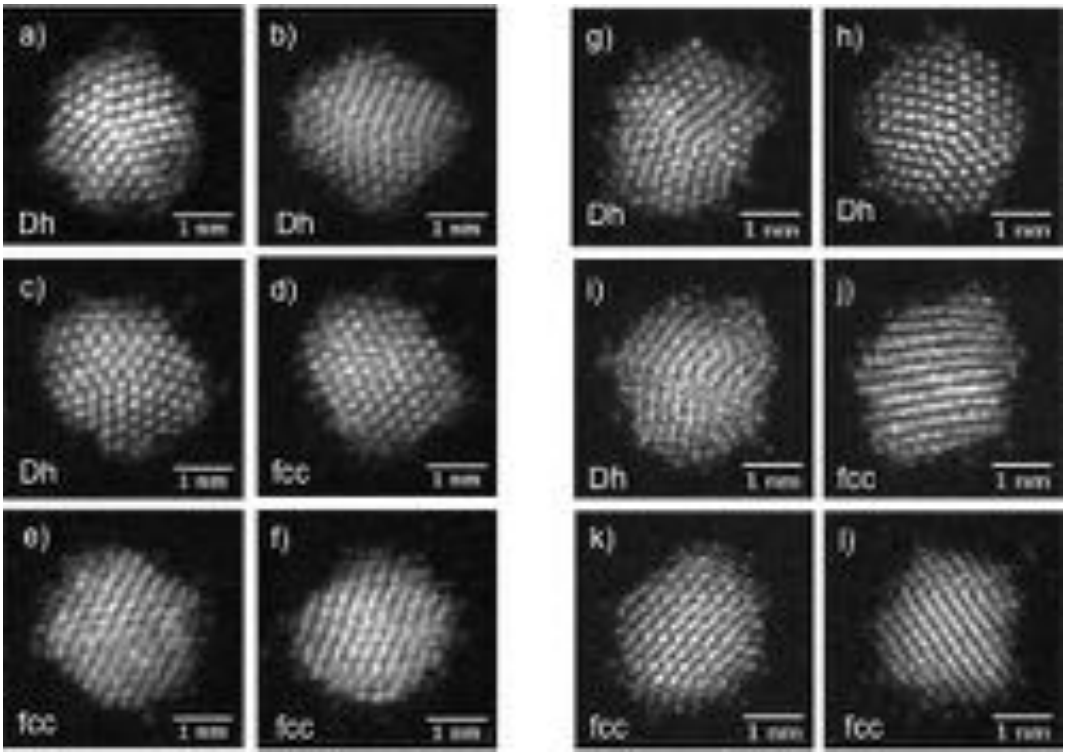

Figure 3.4: Examples of the Dh-fcc transition seen in electron beam irradiation experiments. (a-f) shows frames 1, 20, 35, 37, 57 and 89 of an e-beam irradiation video, the cluster has Dh structure in (a-c) and fcc structure in frames (d-f). In this case the structural transition took place at frame 36. (g-l) shows frames 2, 17, 37, 42, 51 and 74 of another e-beam irradiation video, the cluster has Dh structure in (g-i) and fcc structure in (j-l). In this case the structural transition took place at frame 42.

These results demonstrate that the Dh is not the ground state structure at this size; it is metastable, transforming to fcc under e-beam irradiation. fcc is most likely the ground state structure because it is stable under the electron beam. The metastability of the Dh, the most commonly observed structure, confirms the

kinetic trapping hypothesis. The general trend expected for Au nanoclusters is from Ih→Dh→fcc with increasing size due to competition between internal strain and surface energy. Assuming this to be true, for Au, fcc is already the most stable structure by 561 atoms. This is in agreement with several theoretical studies [8, 10, 16] but in contradiction to results by Barnard et al [7] who predict fcc are only stable at much larger sizes (>15nm). The growth of clusters on seed Dh structures also indicates that the decahedron is most stable at a smaller size, earlier on in the growth of the cluster. For example this could be a 434 atom Marks-Dh. Similarly, the absence of Ih in the experimental data can be explained by the fact that they are only stable at very small sizes, early on in the growth process, when the clusters still have enough energy to rearrange. This is corroborated by the manipulation experiments of Wang et al [17] that show the Ih to be metastable at size 923, transforming to Dh under e-beam irradiation.

Continuous irradiation with the electron beam can cause atom loss [18]. To confirm that structural changes were not as a result of the size of the cluster changing, figure 3.5 shows a plot of HAADF intensity vs frame number for the cluster shown on the left of figure 3.4. Although the resolution of this plot is not high enough to identify the loss of a single atom, it can rule out a continuous atom loss over the time frame of the structural transformation. The HAADF intensity only drops after about 90 frames, whereas structural transformation takes place at frame 36. The high contrast images in figure 3.5 show several single atoms surrounding the cluster surface, indicating that single atoms are ejected from the cluster. However, single atoms are not observed further away from the cluster, suggesting that atoms are ejected and then re-join the cluster during irradiation. Depending on the distance of the single atoms from the cluster, these atoms may contribute to the background intensity measurement.

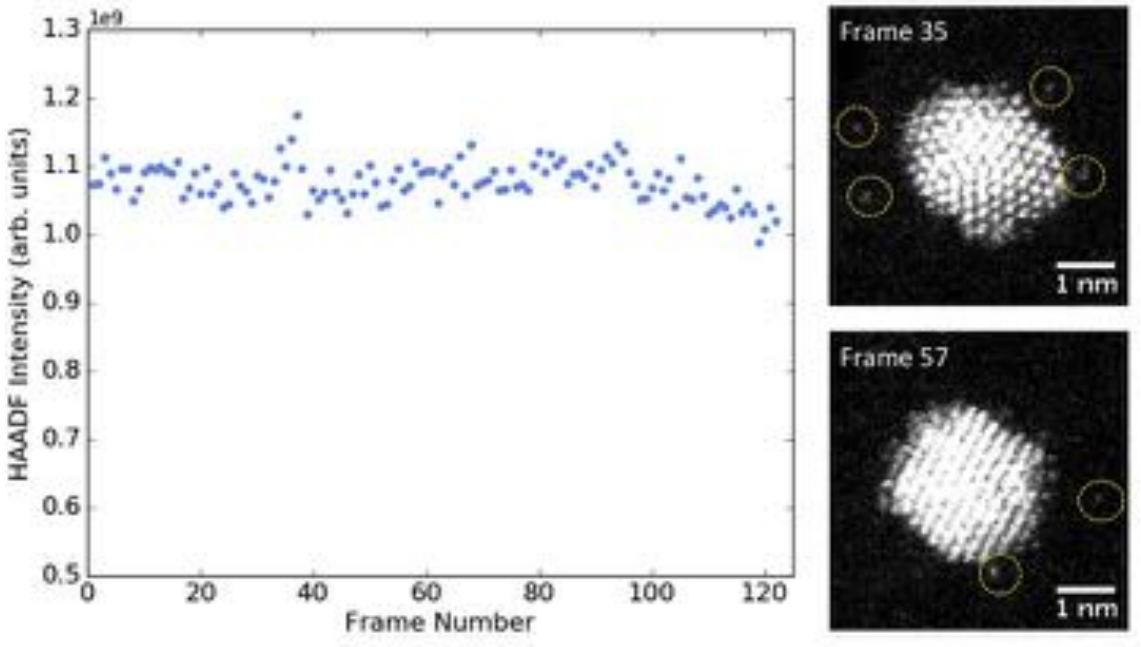

Figure 3.5: Left hand side: a plot of HAADF intensity versus frame number for the Au_{561} cluster shown in (a-f) of figure 3.4. Right hand side: high contrast images of the same Au_{561} cluster (frames 35 and 57) with several single atoms indicated by yellow circles.

To further explore the growth mechanism of Au clusters, molecular dynamic simulations were performed by Guilia Rossi and Riccardo Ferrando [1]. The growth of Au clusters from 13 to 923 atoms was simulated for 3 different temperatures: 400K, 500K and 600K, and the atomic structure determined by common-neighbour analysis [19]. In all cases they found that the clusters were liquid at small sizes and solidified during growth, the size at which they solidified being temperature dependent. For all but one case (35/36 simulations), there were no structural transitions observed during growth whilst the cluster was solid. This result is in good agreement with the idea that Au clusters are kinetically trapped and grow on smaller seed structures. Table 3.2 shows the results of the growth simulations. The Dh was the most commonly grown structure (50%), followed by fcc (36%) and Ih (6%). It was found that whilst the Dh and fcc structures differ in energy by less than 1eV, the Ih are much higher in energy. These results show very good agreement with the proportions of structural isomers observed for Au_{561}, Au_{742} and Au_{923}.

Table 3.2: Results of the growth simulations. The proportion of Dh, fcc, Ih and unclassified clusters at T = 400 K, T = 500 K, T = 600 K, and the overall percentage of structures is shown. Data and caption from reference 1.

Growth Temperature (K)	Decahedral	fcc	Icosahedral	Unclassified
400	6	3	1	2
500	7	4	0	1
600	5	6	1	0
Total	18 (50%)	13 (36%)	2 (6%)	3(8%)

3.1.3 Summary

In conclusion, the gas phase growth of Au clusters between 561 and 923 atoms was investigated. It was found that sizes 561, 742 and 923 present the same proportion of structural isomers when produced under the same conditions, this is attributed to kinetic trapping and template growth on a seed structure. For Au_{561} the most abundant Dh structures were found to be metastable with respect to fcc structures, confirming the idea that the clusters were kinetically trapped during growth. The fcc structure was determined to be the ground state structure for Au_{561}, due to its stability under electron beam irradiation. Molecular dynamic simulations of cluster growth are in excellent agreement with the experimental results, showing no solid-solid structural transitions during growth and similar final isomer proportions.

3.2 Control of the Atomic Structure of Au_{309} Clusters: The Effect of Condensation Length

3.2.1 Methods

Clusters consisting of 309 ± 8 atoms were produced with a magnetron sputtering, gas aggregation cluster source with LTOF mass filter and soft-landed ($\leq$ 2 eV/atom)

onto amorphous carbon coated TEM grids. In all cases the magnetron power (10W), condensation chamber pressure (≈0.5 mbar) and Ar and He gas flows (180 ± 10 sccm) were kept constant, whilst the condensation length was varied between 150 and 250 mm. The samples were characterised using HAADF ac-STEM and the atomic structure of the clusters were identified by comparison with a simulation atlas for Au_{309} (for details of method see section 3.1).

3.2.2 Results and Discussion

Figure 3.6 shows typical HAADF STEM images of Au_{309} clusters (top) and corresponding multislice electron scattering simulations (bottom) from the simulation atlas of the cuboctahedron, Ino-decahedron and Mackay-icosahedron. (a, b) shows an on axis (0, 0) Ino-decahedron, (c, d) a cuboctahedron at a (0, 30°) rotation, (e, f) an icosahedron at a (9°, 15°) rotation and g) an example of an amorphous cluster. As in section 3.1, the atomic structure of the Au_{309} clusters were classified more generally as fcc, Dh, Ih or UI/A .

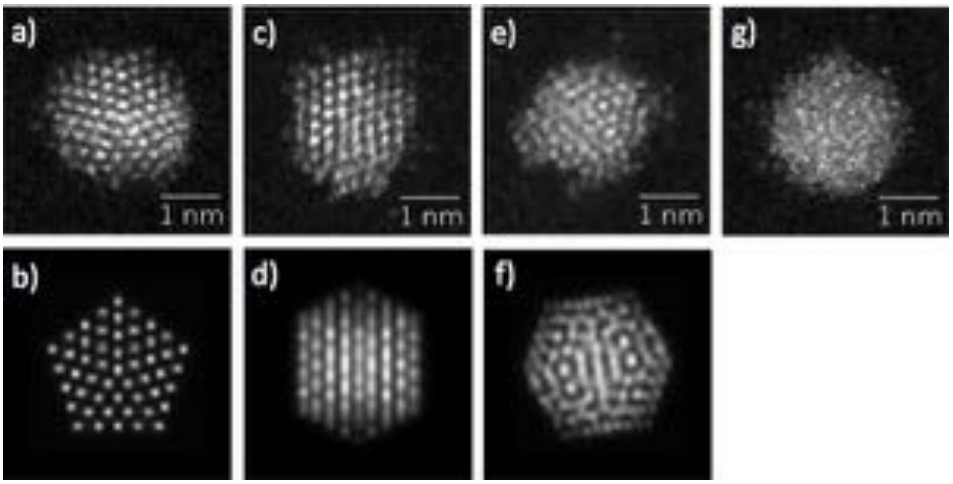

Figure 3.6: HAADF STEM images and corresponding electron scattering simulations [6] for Au_{309} clusters. (a, c, e, g) show HAADF STEM images of Au_{309} clusters with corresponding electron scattering simulations in (b, d, f): (a, b) Ino-decahedron (0, 0) orientation (Dh family), (c, d) cuboctahedron (15°, 60°) orientation (fcc family). (e, f) Icosahedron (9°, 15°) (Ih family), and (g) an amorphous cluster. The specific orientations (θ, α) of the model clusters used in the simulated images are given in chapter 2.

For each condensation length employed (150, 170, 190, 220, 250 mm) more than 150 clusters were imaged for structural analysis. The proportion of structural isomers at each condensation length is shown in figure 3.7, straight line fits to the data are shown as a guide to the eye. The error on the isomer proportions is a statistical counting error and the error on the condensation length is half the smallest division on the linear drive of the magnetron (±0.5 mm). As the condensation length is decreased from 250 mm to 150 mm the proportion of fcc isomers increases linearly from 30% to 58% and the proportion of UI/A clusters decreased linearly from 42% to 17%. The proportion of Ih isomers also increases slightly (0 to 6%) whilst the Dh portion remains fairly constant (between 22 and 25%).

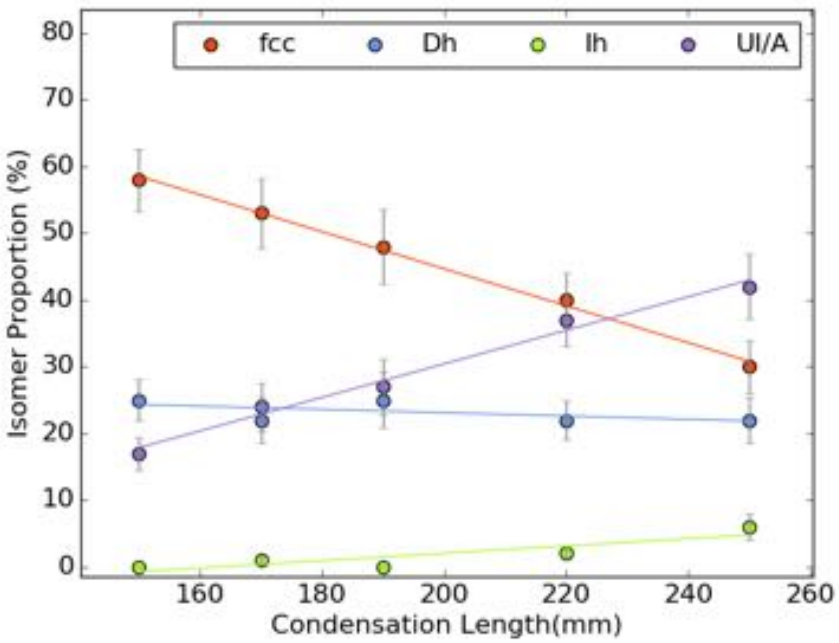

Figure 3.7: Proportion of structural isomers versus condensation length. Clusters classified as fcc, Dh, Ih or UI/A. Data is indicated by scatter points and straight line fits are shown. Error bars are shown for the isomer proportions.

To confirm that the large proportion of UI/A clusters were not masking an underlying trend, further analysis of the UI/A clusters was undertaken. Clusters that appeared truly amorphous were separated and the remaining UI structures were identified as most likely fcc, Dh or Ih. For this analysis general motifs, common to these structure groups, were used for identification. For example 'ring-dot' features

that are only observed in Ih structures [20] were used and an indicator of Ih structure, and clusters that consisted of straight lines across the majority of the image were identified as fcc.

Figure 3.8 shows the proportion of structural isomers for each condensation length after the extended UI/A analysis. As the condensation length is decreased from 250 mm to 150 mm the proportion of fcc isomers increased linearly from 43% to 65%, the proportion of amorphous clusters and Ih decreased linearly from 14% to 3% and 10% to 1% respectively, and the proportion of Dh was constant at ≈30%. The general trend remains the same; with a decrease in condensation length there is a corresponding increase in Ih and amorphous structures.

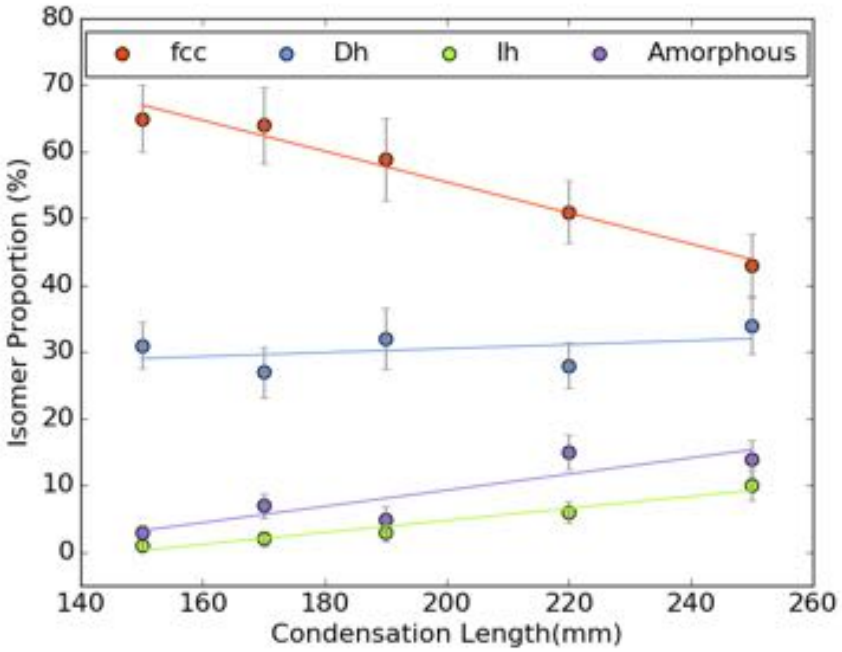

Figure 3.8: Proportion of structural isomers versus condensation length: data after UI/A amorphous analysis. Clusters are classified as fcc, Dh, Ih, or Amorphous. Data is shown as scatter points and straight line fits are also shown. Error bars are shown for the isomer proportions.

The condensation length is the distance between the magnetron and the exit nozzle of the condensation chamber, this is shown by a schematic in figure 3.9. It is the distance over which the clusters grow and so is representative of the growth time. Logically, a longer growth time would result in more equilibrated clusters, with a

higher proportion of low energy structures, and a shorter growth time would result in a greater proportion of higher energy structures, far from equilibrium. This logic was successfully used to explain the change in the proportion of Ih isomers for Au_{923} clusters as the condensation length was varied [4]. As the condensation length was decreased it was found that there was a decrease in Ih structures, that are known to be unstable at this size [17]. This was explained by the trapping of unstable Ih structures during short growth times.

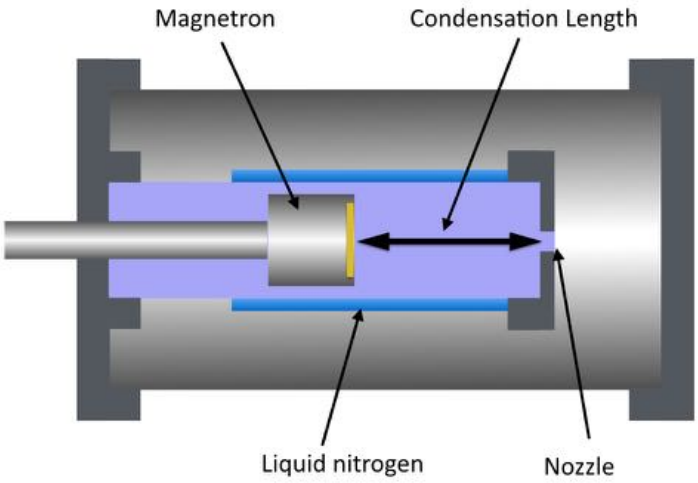

Figure 3.9: Schematic showing the condensation length in the condensation chamber of the magnetron sputtering gas aggregation cluster source. Diagram not to scale.

Interpreting the data shown in figure 3.8 in the same way leads to the conclusion that fcc is a high energy structure at this size, its proportion being larger for shorter growth times, and Ih and amorphous structures are lower in energy, their proportion increasing at longer growth times. However, if this is the case then why is fcc the most abundant isomer? Even if kinetic trapping is considered it seems unlikely that a smaller stable fcc structure acts as a seed, because this would contradict the generally accepted stability from Ih-Dh-fcc with increasing size (although it is not inconceivable that a particularly low energy fcc structure exists at a smaller size [11]). Furthermore, by comparison with the results from section 3.1, it appears that Au_{309} is not kinetically trapped - its proportion of structural isomers at 250 mm

condensation length being different to those at sizes 561, 742 and 923. Au_{309} is the smallest size cluster studied, this means that it is more likely to have enough energy to rearrange to the ground state structure. Given that fcc is the ground state structure for Au_{561} it is probable that this is also the case for Au_{309}.

To be able to interpret the condensation length data, further investigation into the relative stability of structural isomers at size 309 was undertaken. 'Video imaging' of individual Au_{309} clusters was performed at a dose of between $1.3 - 10.0 \times 10^4/e^-/Å^2$/frame, for a minimum of 100 frames. In contrast to Au_{561} and Au_{923} [1, 4], continuous fluctuations between different structural isomers were observed. The structural fluctuations are assumed to be a result of electron beam heating. The effect of knock-on damage and cluster charging are assumed to be negligible because the electron beam energy is much lower than the knock-on damage threshold for Au (the threshold for surface sputtering of Au is 400kV [21]), and the substrate is a good conductor of electricity. Figure 3.10 shows an example of an individual Au_{309} cluster fluctuating between different structural isomers. The cluster continually fluctuates between different orientations of fcc and Dh structures, amorphous or unidentified arrangements (as seen in frames 88 and 139) and structures with local Ih symmetry (frame 143).

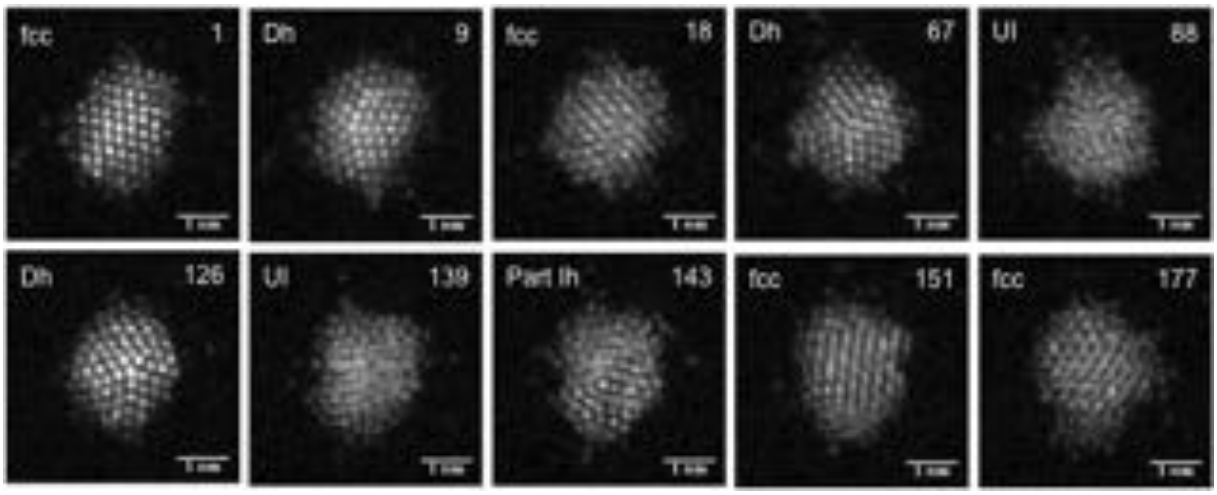

Figure 3.10: A selection of HAADF STEM images from a video of Au_{309}. The frame number is shown in the top right of each image and the atomic structure classification in the top left.

Because no clear transformation from one structure to another occurred, a different approach was taken to determine the ground state structure. 11 videos were recorded, consisting of a total of 1293 frames, and a frame by frame analysis was conducted whereby each video frame was identified as fcc, Dh, Ih or UI/A. The continuous irradiation with the STEM electron beam should allow the clusters to explore the potential energy surface. The structure most commonly observed (isomer with longest total residence time) is then considered the ground state (or lowest free energy) structure. This method was used previously to determine the atomic structures of Au_{20} and Au_{55} clusters [22, 23]. The results of the frame by frame analysis are shown in figure 3.11. UI/A structures are excluded because the nature of the experiment leads to many transitional amorphous and UI structures as well as out of focus frames (66% of frames fall into this category). It was found that 56% of identifiable structures were fcc, 37% Dh and 7% Ih.

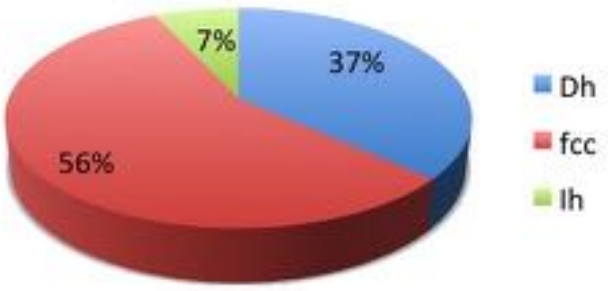

Figure 3.11: The proportion of structural isomers identified as fcc, Dh or Ih from the frame by frame analysis of all Au_{309} structural fluctuation videos. A total of 434 identified frames.

This result confirms that fcc is the ground state structure at size 309 (similarly to size 561) and implies that kinetic trapping was not a dominant growth mechanism for N$\leq$309 atoms under these formation conditions. Curley et al [24] reported a different proportion of structural isomers for Au_{309} based on static HAADF STEM images of Au_{309} clusters produced by a magnetron sputtering gas aggregation cluster source (Ino-decahedral 32%, cuboctahedral 25%, icosahedral 8%). The difference between the two seemingly similar experimental investigations is most likely due to

differing formation conditions in the magnetron sputtering, gas aggregation cluster source. The video imaging technique employed in this thesis means the formation conditions (resulting in kinetic trapping) do not contribute to the overall result of the investigation. Considering the result of section 3.1, that metastable Dh are formed by kinetic trapping, it follows that at 250mm condensation length kinetic trapping must occur between 309 and 561 atoms. The abundance of metastable Dh being a result of a particularly stable Dh in this size range (possible Marks-Dh-434).

The implication of fcc being the ground state structure on the condensation length data in figure 3.8, is that it cannot be interpreted in terms of longer growth time resulting in more equilibrated, ground state structures. Instead, other interpretations must be considered. One possibility is related to temperature. Due to the plasma formed in front of the magnetron gun, there will be a temperature gradient between the magnetron and the exit nozzle, with the temperature being higher at the magnetron and much lower at the nozzle [25]. This means that for shorter condensation lengths the clusters will be hotter than at longer condensation lengths. The result of a higher average cluster temperature would likely be a more equilibrated system; clusters having enough energy to rearrange to the ground state structure. In the case of Au_{309} this would lead to an increase in the proportion in fcc at shorter condensation lengths, in agreement with the experimental data. The increase in proportion of amorphous and Ih structures may also be explained by the fact that they are higher energy structures and so take less thermal energy to rearrange to ground state fcc, whereas Dh are expected to be much closer in energy to fcc [8, 16] so would take more thermal energy to rearrange. This effect would be more prominent for smaller clusters, for which less energy (lower temperature) is required for structural transformation, which can explain why this effect is not seen for Au_{923}.

Another interpretation involves the consideration of different growth routes within the condensation region. Initially small seed structures are formed by 3 body collisions between two metal atoms and one helium atom [2, 26, 27, 28]. Following this,

there are two mechanisms by which clusters may grow; atom by atom addition on smaller seed structures and coalescence of two or more larger sized clusters. Given a certain amount of sputtered material, smaller sized clusters should take less time to grow than larger clusters. Therefore, the condensation length at which the majority of Au_{309} clusters is formed will be shorter than for Au_{923}. If the atom by atom growth mechanism is not dominant at longer condensation lengths then the coalescence mechanism may start to become noticeable in the form of more UI/A and Ih structures. Coalescence of two or more clusters may lead to more unusual, unidentifiable (or amorphous) structures. Considering the case of Au_{309}, this would likely involve the coalescence of Ih clusters, which are expected to be most favourable at small sizes [8, 10, 16].

Molecular dynamics simulations of coalescence were performed by Giulia Rossi and Riccardo Ferrando. They investigated the atomic structures formed by the coalescence of clusters with different starting structures, and at different temperatures. The resultant cluster having approximately 309 atoms. Table 3.3 shows a summary of their results. In some cases perfect structures are obtained, in others unusual composite structures are formed that are unlikely to be identifiable using our simulation atlas method.

Table 3.3: Result of molecular dynamics simulations of cluster coalescence. The initial structures, final size in number of atoms, temperature, and final structure is shown. Results from unpublished data produced by Giulia Rossi and Riccardo Ferrando.

Cluster 1	Cluster 2	Total Size	Temperature (K)	Final Structure
Au_{147}-Ih	Au_{147}-Ih	294	300	Part Ih, part Dh
Au_{147}-Ih	Au_{147}-Ih	294	400	Part Ih, part Dh
Au_{147}-Ih	Au_{147}-Ih	294	500	Part Ih, part Dh
Au_{147}-Ih	Au_{147}-Ih	294	600	Liquid
Au_{147}-Ih	Au_{162}-Dh	309	400	Structure with 2 5-fold axis
Au_{147}-Ih	Au_{162}-Dh	309	400	Structure with 2 5-fold axis
Au_{147}-Ih	Au_{162}-Dh	309	500	Dh
Au_{147}-Ih	Au_{162}-Dh	309	500	Dh
Au_{147}-Ih	Au_{162}-Dh	309	600	Liquid
Au_{147}-Ih	Au_{162}-TO	309	400	fcc
Au_{147}-Ih	Au_{162}-TO	309	400	Distorted Dh
Au_{147}-Ih	Au_{162}-TO	309	500	twinned fcc
Au_{147}-Ih	Au_{162}-TO	309	500	twinned fcc
Au_{147}-Ih	Au_{162}-TO	309	600	liquid
Au_{147}-Dh	Au_{162}-TO	309	400	twinned fcc
Au_{147}-Dh	Au_{162}-TO	309	500	twinned fcc

3.2.3 Summary

In conclusion, the effect of condensation length on the atomic structures of Au_{309} has been investigated. It has been shown that the proportions of atomic structures can be controlled by changing the condensation length; significantly more fcc structures were generated at short condensation lengths (43% at 250mm to 65% at 150mm). This may be useful for catalysis studies where atomic structure is thought to play

an important role. Electron beam manipulation experiments showed that fcc is the ground state structure, followed by Dh, with Ih being highest in energy. The reason for the increased proportion of ground state fcc structures and decrease of high energy Ih and amorphous structures at shorter condensation lengths/ shorter growth times is unclear. Two possible reasons have been suggested, one relating to the effect of the temperature in the condensation region and the other relating to the dominance of different growth routes.

References

[1] D Wells, G Rossi, R Ferrando, and R E Palmer. Metastability of the atomic structures of size-selected gold nanoparticles. *Nanoscale*, 7:6498–6503, 2015.

[2] S Pratontep, S J Carroll, C Xirouchaki, M Streun, and R E Palmer. Size-selected cluster beam source based on radio frequency magnetron plasma sputtering and gas condensation. *Review of Scientific Instruments*, 76(4):045103, 2005.

[3] B von Issendorff and R E Palmer. A new high transmission infinite range mass selector for cluster and nanoparticle beams. *Review of Scientific Instruments*, 70(12):4497, 1999.

[4] S R Plant, L Cao, and R E Palmer. Atomic structure control of size-selected gold nanoclusters during formation. *Journal of the American Chemical Society*, 136(21):7559–7562, 2014.

[5] N Young, Z Li, Y Chen, S Palomba, M Di Vece, and R E Palmer. Weighing supported nanoparticles: size-selected clusters as mass standards in nanometrology. *Physical Review Letters*, 101(24):246103, 2008.

[6] C Koch. *Determination of core structure periodicity and point defect density along dislocations*. PhD thesis, Arizona State University, 2002.

[7] A S Barnard, N P Young, A I Kirkland, M A Van Huis, and X Huifang. Nanogold: a quantitative phase map. *ACS Nano*, 3(6):1431–1436, 2009.

[8] F Baletto, R Ferrando, A Fortunelli, F Montalenti, and C Mottet. Crossover among structural motifs in transition and noble-metal clusters. *The Journal of Chemical Physics*, 116(9):3856–3863, 2002.

[9] C-L Kuo and P Clancy. Melting and freezing characteristics and structural properties of supported and unsupported gold nanoclusters. *Journal of Chemical Physics B*, 109:13743–13754, 2005.

[10] H Li, L Li, A Pedersen, Y Gao, N Khetrapal, H Jonsson, and X C Zeng. Magic-number gold nanoclusters with diameters from 1 to 3.5 nm: relative stability and catalytic activity for CO oxidation. *Nano letters*, 15:682–688, 2015.

[11] K Bao, S Goedecker, K Koga, F Lançon, and A Neelov. Structure of large gold clusters obtained by global optimization using the minima hopping method. *Physical Review B*, 79(041405(R)):1–4, 2009.

[12] F Baletto, C Mottet, and R Ferrando. Reentrant morphology transition in the growth of free silver nanoclusters. *Physical Review Letters*, 84(24):5544–5547, 2000.

[13] M A Gracia-pinilla, D Ferrer, S Mejia-Rosales, and E Perez-Tijerina. Size-selected Ag nanoparticles with five-fold symmetry. *Nano Express*, 4:896–902, 2009.

[14] A Volk, P Thaler, M Koch, E Fisslthaler, W Grogger, and W E Ernst. High resolution electron microscopy of Ag-clusters in crystalline and non-crystalline morphologies grown inside superfluid helium nanodroplets. *The Journal of Chemical Physics*, 138(214312):1–7, 2013.

[15] F Baletto, C Mottet, and R Ferrando. Microscopic mechanisms of the growth of metastable silver icosahedra. *Physical Review B*, 63(15):155408, 2001.

[16] B Wang, M Liu, Y Wang, and X Chen. Structures and energetics of silver and gold nanoparticles. *The Journal of Physical Chemistry C*, 115(23):11374–11381, 2011.

[17] Z W Wang and R E Palmer. Determination of the ground-state atomic structures of size-selected Au nanoclusters by electron-beam-induced transformation. *Physical Review Letters*, 108(24):245502, 2012.

[18] J Reyes-Gasga, G R. Garcia, and M Jose-Yacaman. Electron-beam-induced structure transformation of the quasicrystalline phases of the $Al_{62}Cu_{20}Co_{15}Si_3$ alloy. *Radiation Physics and Chemistry*, 45(2):283–291, 1995.

[19] D Faken and H Jonsson. Systematic analysis of local atomic structure combined with 3D computer graphics. *Compuational Materials Science*, 2:279–286, 1994.

[20] N Jian and R E Palmer. Variation of the core atomic structure of thiolated $(Au_xAg_{1-x})_{312\pm55}$ nanoclusters with composition from aberration-corrected HAADF STEM. *The Journal of Physical Chemistry C*, 119(20):11114–11119, 2015.

[21] R F Egerton, R Mcleod, F Wang, and M Malac. Basic questions related to electron-induced sputtering in the tem. *Ultramicroscopy*, 110:991–997, 2010.

[22] Z W Wang and R E Palmer. Direct atomic imaging and dynamical fluctuations of the tetrahedral Au_{20} cluster. *Nanoscale*, 4(16):4947–9, 2012.

[23] Z W Wang and R E Palmer. Experimental evidence for fluctuating, chiral-type Au_{55} clusters by direct atomic imaging. *Nano Letters*, 12:5510–5514, 2012.

[24] Z Y Li, N P Young, S Di Vece, M andPalomba, R E Palmer, A L Bleloch, B C Curley, R L Johnston, J Jiang, and J Yuan. Three-dimensional atomic-scale structure of size-selected gold nanoclusters. *Nature*, 451:46–8, 2008.

[25] A Bogaerts, R Gijbels, and V V Serikov. Calculation of gas heating in direct current argon glow discharges. *Journal of Applied Physics*, 87(12):8334, 2000.

[26] P V Kashtanov, B M Smirnov, and R Hippler. Magnetron plasma and nanotechnology. *Physics-Uspekhi*, 50(5):455, 2007.

[27] P V Kashtanov, B M Smirnov, and R Hippler. Efficiency of cluster generation in a magnetron discharge. *Europhysics Letters*, 91(6):63001, 2010.

[28] B M Smirnov. Processes involving clusters and small particles in a buffer gas. *Uspekhi Fizicheskih Nauk*, 181(7):713, 2011.

Chapter 4

Experimental Determination of the Energy Difference Between Competing Isomers in Deposited, Size-Selected Gold Clusters

In this chapter the proportion of structural isomers for Au_{561} clusters is determined for temperatures between 20°C and 500°C. Based on this data, an experimental method for determination of the energy difference between competing Dh and fcc isomers is presented. A magnetron sputtering gas aggregation cluster source with LTOF mass filter was used for production of size-selected clusters. Heating of the samples was performed in-situ using a DENS solutions Wildfire heating holder for the STEM, and samples were characterised using HAADF ac-STEM. Production of size-selected cluster samples, STEM imaging, and structural analysis were performed by the author. The method for determination of the energy difference between isomers resulted from discussions with Riccardo Ferrando (INFM and IMEM/CNR, University of Genoa) and Hannes Jonsson (Faculty of Physical Sciences, University of Iceland). The content of this chapter is taken largely from a draft version of a paper written by the author.

4.1 Introduction

Nanoclusters can be used in a wide variety of applications from catalysis [1] to drug delivery [2, 3] and chemical sensing [4]. Understanding the energy difference between structural isomers is important not only for the design of well defined materials but also for understanding how these materials will work in-situ. For example, if a particular structural isomer is unstable, application of high temperature is likely to drive it toward the ground state, altering (and potentially degrading) the characteristics of the system. There has been a significant theoretical effort to determine the ground state structures and energy differences between competing isomers in nanoclusters [5]. In particular, gold has received much attention due to the role of structure in its catalytic performance [6].

Experimentally the atomic structure of nanoclusters can be determined by trapped ion electron diffraction [7], x-ray scattering [8], TEM tilt series [9], and HAADF STEM [10]. However, the formation conditions often lead to trapping of higher lying isomers and the population of clusters observed does not represent the ground state (or lowest free energy) structure [11]. Previous studies have gained some insight in to the potential energy surface of clusters through e-beam transformation experiments in the STEM and through ex-situ annealing. By continual irradiation with the e-beam larger (Au_{561} [12] and Au_{923}) clusters have been shown to transform one-way to the ground state structure [11] and smaller clusters have been shown to fluctuate continually [13, 14, 15] - allowing potential low energy structures to be identified. With these experiments it is not possible to quantify the energy difference between isomers because the temperature to which the e-beam heats the cluster to is unknown. Annealing experiments performed by Koga et al [16] found that annealing of small and medium sized (<14nm) Au clusters below the melting point (<1273K), resulted in the transformation of Ih to Dh and annealing above the melting point (1373K) resulted in fcc structures. Based on these results the conclusion drawn was that the energy barrier between Dh and fcc must be much larger than between Ih and Dh. No quantitative measure of the energy difference or

barrier height can be made via this method because the size distribution is broad and the structural analysis is performed after annealing, ex-situ. To determine the energy difference between isomers, the proportion of structural isomers has to be determined at a range at temperatures for a system in thermodynamic equilibrium, this is discussed in more detail below.

Here we use a heating stage in the aberration corrected STEM to determine the proportion of structural isomers for size-selected Au_{561} clusters at a range of temperatures. This enables the energy difference between competing fcc and Dh isomers to be calculated for Au_{561}. We identify two regimes: a low temperature regime in which metastable Dh transform to fcc and a high temperature regime in which the Dh isomer is repopulated. From the high temperature region data we find that the Dh and fcc are very close in energy with the Dh only 0.04±0.02eV higher than fcc. This analysis is based on the idea that, for an equilibrium system, at higher temperatures a greater proportion of clusters will occupy higher energy states (higher energy structural isomers), following Boltzmann statistics.

4.2 Methods

Au clusters consisting of 561±14 atoms were produced with a magnetron sputtering gas aggregation cluster source [17], with lateral time of flight mass filter ($M/\Delta M=20$) [18]. The clusters were deposited onto amorphous silicon nitride films of heating chips in the soft-landing regime (<2eV/atom) [19] to preserve their original atomic structure.

A JEOL 2100F scanning transmission electron microscope (STEM) with spherical aberration corrector (CEOS) and inner high angle annular dark field (HAADF) detector collection angle of 62 mrad was employed for atomic resolution imaging of the nanoclusters. In-situ heating was performed using a DENS solutions wildfire heating holder and DENS solutions MEMS based heating chips. The heating chips consisted of a metal heater coil embedded in silicon nitride, surrounded by imaging 'windows' of silicon nitride. A current was applied to the metal coil to heat the chips

whilst the resistance was measured in-situ using the four point probe method. The temperature was known from the chip calibration, performed by the supplier using a pyrometer. The error on the temperature measurement is 5%, and the temperature stability <1°C.

Experiments were conducted by setting the temperature to a constant value and taking static HAADF images of a population of clusters. At each temperature ≥ 100 clusters were imaged. The atomic structure of the clusters was then identified by comparison with multi-slice electron scattering simulations of the cuboctahedron, Ino-decahedron and icosahedron at different orientations using the simulation atlas method [11].

4.3 Results

4.3.1 Atomic Structure Versus Temperature

Figure 4.1 shows HAADF STEM images of Au_{561} clusters and corresponding multi-slice simulations from a simulation atlas. Images A) and B) were recorded at 20°C. A) shows a cuboctahedron at a (15, 60) rotation, B) shows an Ino-decahedra at a (18, 10) rotation. Images C) and D) were recorded at 500°C. C) shows a cuboctahedron at a (15, 60) rotation, and D) an on-axis Ino-decahedron.

The clusters investigated here contain 561±14 atoms, consequently the observed structures will deviate from the perfect cuboctahedron, Ino-decahedron and icosahedron and will instead contain a range of different truncations. Therefore we concentrate on the core atomic structure; HAADF STEM images matched to the cuboctahedron simulations are classified more generally as face-centred-cubic (fcc), images matched to the Ino-decahedron as decahedra (Dh).

Figure 4.2 shows the proportions of structural isomers observed for Au_{561} clusters at temperatures ranging from 20°C to 500°C. The same sample was used for all measurements so that formation conditions would not affect the results [20]. Cluster structures are identified as either face-centred-cubic (fcc), decahedra (Dh),

icosahedra (Ih) or unidentified/ amorphous (UI/A). The error on the proportion of structural isomers is a statistical counting error and the error on the temperature is 5%, due to the heating chip calibration as is discussed in the methods section.

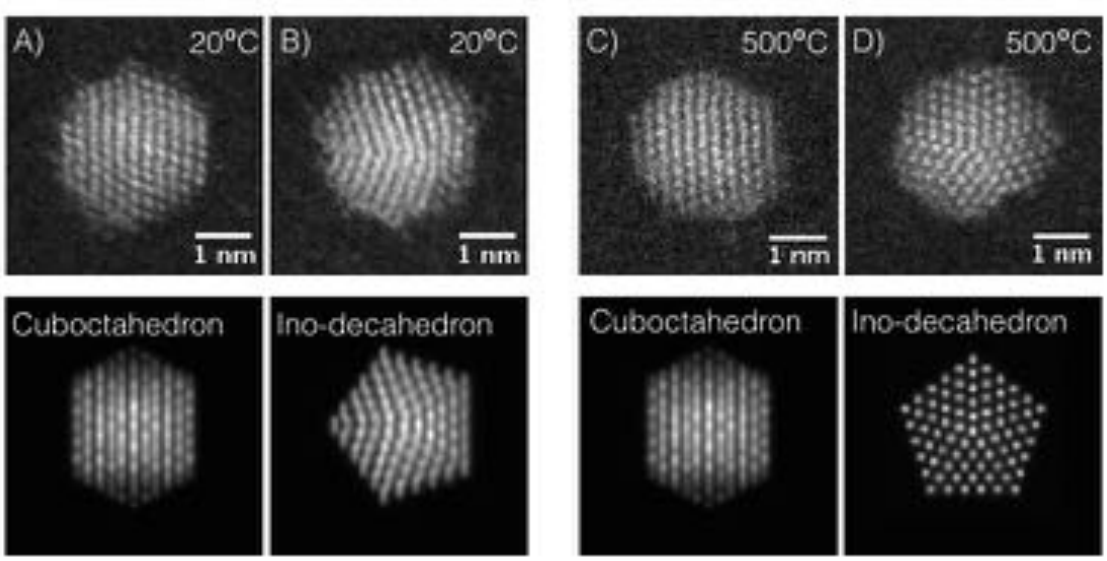

Figure 4.1: HAADF STEM images of Au_{561} clusters and matching multi-slice HAADF STEM simulations of the cuboctahedron and Ino-decahedron at different orientations. A) and B) show images recorded at 20°C and C) and D) show images recorded at 500°C.

At all temperatures investigated the majority of structures are fcc, followed by Dh, and Ih with a very low proportion (0-3%). The percentage of UI/A structures is fairly constant across the temperature range. We find that the clusters still provide a good match with the simulated structures at high temperature and there is no evidence of melting, as can be seen from figure 4.1. Between 20°C and 150°C the increase in temperature results in a increase in fcc. At temperatures $\geq$150°C the proportion of fcc gradually decreases. Complimentary to this, between 20°C and 125°C the proportion of Dh decreases and at temperatures $\geq$125°C there is a slight increase in Dh.

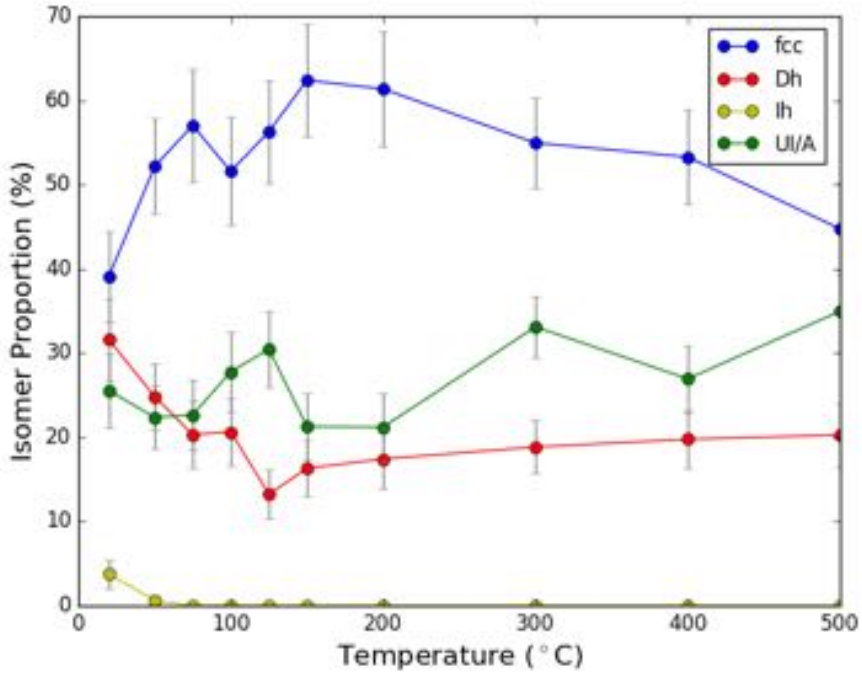

Figure 4.2: The proportion of structural isomers for Au_{561} at 20°C, 50°C, 75°C,100°C, 125°C, 150°C, 200°C, 300°C, 400°C, and 500°C. The clusters are classified as either face-centred-cubic (blue), decahedral (red), icosahedral (yellow) or unidentified/amorphous (green).

Figure 4.3 shows a plot of the Dh:fcc ratio versus temperature. Two temperature regimes are clearly visible. Between 20°C and 125°C the Dh:fcc ratio decreases from 0.81 to 0.24. Between 125°C and 500°C the Dh:fcc ratio increases from 0.24 to 0.45. The underlying data for this plot and associated errors are the same as for figure 4.2.

The increase in the proportion of fcc from 20°C to 125°C, and corresponding decrease in proportion of Dh, can be explained in terms of the release of trapped metastable Dh to ground state (or lowest free energy) fcc structures. It has previously been reported that Au_{561} clusters undergo a one-way transition from Dh to fcc when continuously exposed to the STEM electron beam [12] which can be considered similar to heating of the sample. Considering this explanation, one would expect the proportion of fcc to increase continually with temperature until all clusters are in the ground state. In contrast to this we see an increase in fcc from 20-150°C

followed by a slight decrease from 150-500°C.

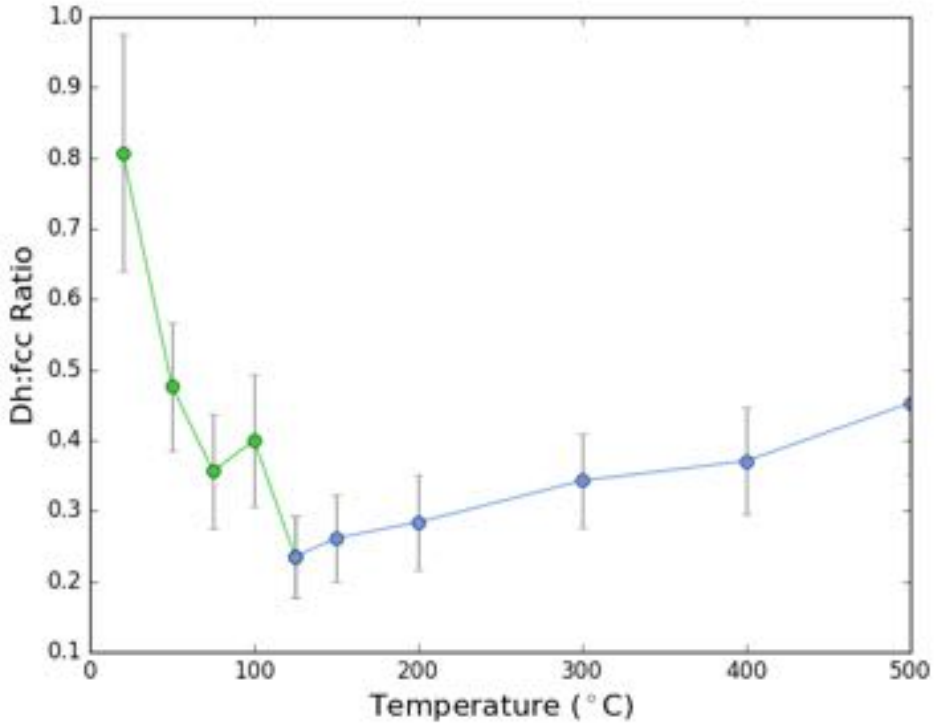

Figure 4.3: The Dh:fcc ratio of Au_{561} clusters versus temperature. The low temperature regime (20-125°C) is in light blue and the high temperature regime (125-500°C) in darker blue. Lines between markers are a guide to the eye.

There are several possible explanations for this behaviour. The first is a consequence of the population of clusters ranging in size from 547-575 atoms. It can be argued that the addition or subtraction of one or more atoms changes the ground state structure [21], such that within the size range of 547-575 atoms there may be multiple ground state structures (Dh-type and fcc-type). Hence, for the data presented here, it could be argued that by 100°C all the clusters are in the ground state and the isomer proportions are representative of the proportion of ground state structures within this size range. It is unlikely that this is the case, in the previous e-beam study the size distribution was also 547-574 atoms and Dh-fcc transformations were seen 90% of the time, indicating that fcc is the ground state structure over the entire size range. In addition this does not explain the reversal of the trend in the high temperature region. A second possibility is that as the temperature

of the clusters increase, atoms are lost through sublimation resulting in a smaller cluster size at higher temperatures. If the decahedron is more stable at smaller cluster sizes, then this could explain the slight increase in Dh at higher temperatures. Whilst it is not possible to rule out the loss of tens of atoms, it is unlikely that this is the cause of the increase in Dh. We know from previous studies on Au_{309} and Au_{435} [22] that fcc is the ground state structure at these sizes, indicating that a crossover to the Dh occurs at a size <309 atoms. Based on the diameter of the clusters at 500°C (see fig 4.1), it is obvious that such a large loss of atoms has not occurred. The final explanation assumes that fcc is the ground state (lowest free energy as T> 0) structure; from 20°C to 125°C the proportion of fcc increases as clusters (Dh) transform to the ground state (lowest free energy structure), whereas at higher temperatures (>125°C) a proportion of the clusters are excited to a higher energy, metastable structure - the Dh. According to this explanation the Ih must have a significantly greater energy, as we do not see repopulation of this isomer even at 500°C. This is in agreement with experimental observations of Ih Au_{923} clusters under the electron beam, which were found to transform to Dh or fcc structures after very short exposure times [11].

4.3.2 Determination of the Energy Difference Between Isomers

If the increase in Dh in the high temperature region is a result of excitation of clusters to a higher energy metastable state, then the energy difference between the Dh and fcc structural isomers can be calculated. This is explored in more detail below.

If a system is in thermodynamic equilibrium at a given temperature, T, then the partition function is given by:

$$Q(\beta) = \sum_{\alpha} n_{\alpha} Q_{\alpha}(\beta) \tag{4.1}$$

where β=1/K_BT, Q_α is the partition function of isomer α and n_α is the number of permutational isomers [5, 23]. The harmonic superposition theorem gives the simplest expression for the partition function of isomer α, Q_α:

$$Q_\alpha(\beta) = e^{-\beta E_\alpha} \prod_i \frac{2}{\sinh(\beta\hbar\omega_{\alpha i}/2)} \tag{4.2}$$

where E_α is the potential energy minimum of isomer α and $\omega_{\alpha i}$ represents the vibrational frequencies (i) in minimum α [23]. Considering the classical limit (valid for T> θ_D, θ_D= Debeye temperature [5]), whereby $\hbar\beta\omega_{\alpha i}\rightarrow 0$, equation 4.2 becomes:

$$Q_\alpha^{Classical}(\beta) = \frac{e^{-\beta E\alpha}}{(\beta\hbar\bar{\omega}_\alpha)^\kappa} \tag{4.3}$$

where $\bar{\omega}_\alpha^\kappa$ is the geometrical average of the vibrational frequencies and κ is the number of degrees of freedom [23]. If state α has n_α permutational isomers, the probability of being in isomeric state α is [5]:

$$P_\alpha = \frac{n_\alpha Q_\alpha(\beta)}{Q(\beta)}. \tag{4.4}$$

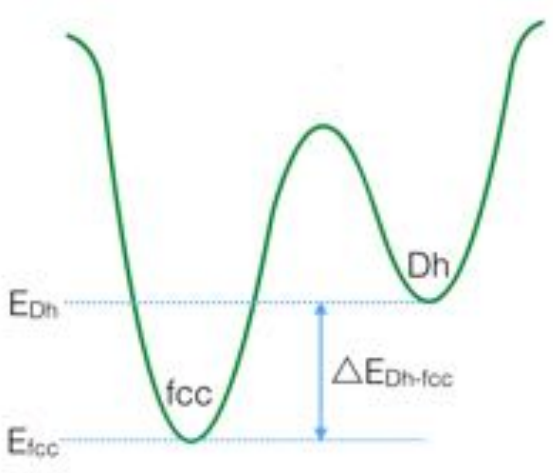

Figure 4.4: A schematic of the Dh and fcc minima to accompany the derivation of the energy difference between Dh and fcc isomers

If we examine the simple case of cluster isomers with only 2 minima correspond-

ing to Dh and fcc isomers (as shown in figure 4.4), the ratio of the probabilities is:

$$\frac{P_{Dh}}{P_{fcc}} = \frac{Q_{Dh}n_{Dh}}{Q_{fcc}n_{fcc}} = \frac{e^{-\beta E_{Dh}}}{e^{-\beta E_{fcc}}} \frac{(\beta\hbar\bar{\omega}_{fcc})^{\kappa}}{(\beta\hbar\bar{\omega}_{Dh})^{\kappa}} \frac{n_{Dh}}{n_{fcc}}. \tag{4.5}$$

Taking the natural logarithm and simplifying:

$$\ln\left(\frac{P_{Dh}}{P_{fcc}}\right) = \beta(E_{fcc} - E_{Dh}) + ln\left(\frac{n_{Dh}}{n_{fcc}}\right) + ln\left(\frac{\bar{\omega}_{fcc}}{\bar{\omega}_{Dh}}\right)^{\kappa} = \beta(E_{fcc} - E_{Dh}) + constant. \tag{4.6}$$

Hence, by making a plot of ln(Dh/fcc) versus 1/T, the energy difference between the Dh and fcc isomers can be determined from the gradient:

$$Gradient = 1/K_B(E_{fcc} - E_{Dh}) \rightarrow \Delta E_{fcc-Dh} = gradient \times K_B \tag{4.7}$$

The Dh:fcc ratio determined from the experimental results presented above is analogous to P_{Dh}/P_{fcc}. Therefore, this analysis can be applied to the data presented in this chapter to determine the energy difference between the Dh and fcc isomers for Au_{561}. However, there are two key assumptions made that must be considered. The partition function for each isomer is given by the harmonic superposition approximation, for which the vibrational frequencies are assumed to be harmonic and independent of temperature. In many cases this approximation has been shown to be valid for temperatures below the melting point [5]. If the vibrational frequencies are anharmonic, there would be a temperature dependence [5], resulting in non-linearity or a change of slope in the plot of ln(Dh/fcc) versus 1/T. Secondly, we have assumed that for each basin (Dh-basin, fcc-basin) in the potential energy surface of the cluster, there is only a contribution from one structural isomer - only one isomer partition function has been considered per structural basin. This assumption is discussed in more detail below with reference to the experimental data.

Figure 4.5 shows a plot of the natural log of the Dh to fcc ratio versus the reciprocal of the temperature. We interpret the low temperature region as the release of trapped metastable Dh to ground state fcc structures, therefore the system is not

in equilibrium and the above analysis cannot be performed. In the high temperature region we see the repopulation of of higher lying Dh isomers (dynamic behaviour) and can therefore assume equilibrium. The green dashed line shows a weighted linear least squares fit to the high temperature region of the plot. The gradient of this line is -510±240 K. Based on the method and assumptions stated above, this gives a value of 0.04±0.02 eV for the energy difference between Dh and fcc isomers (ΔE_{Dh-fcc}).

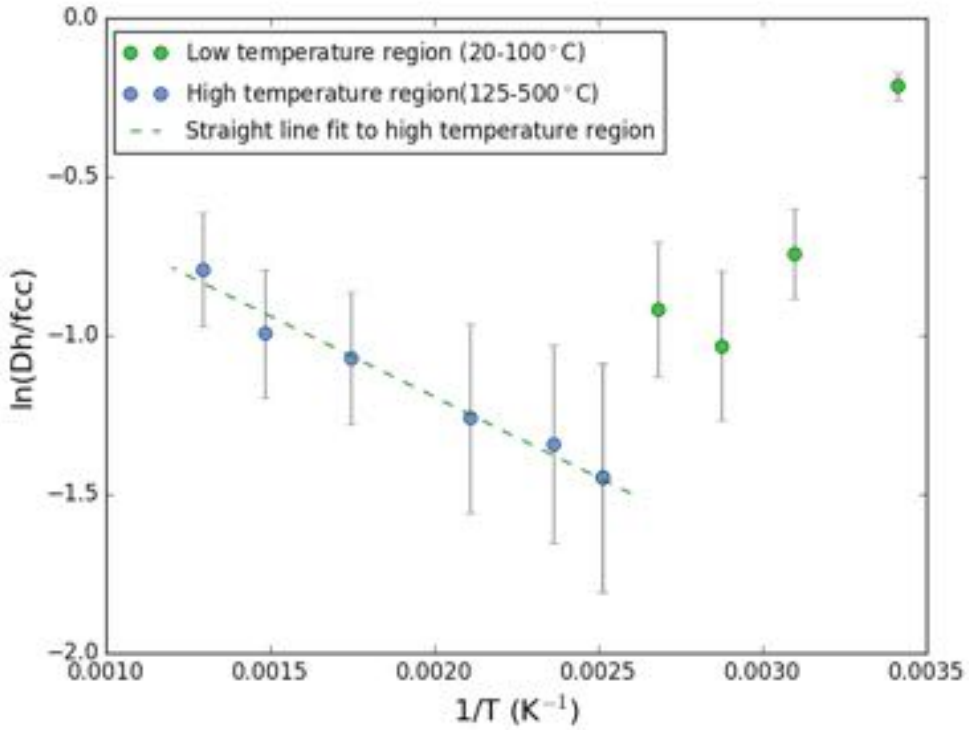

Figure 4.5: The natural logarithm of the Dh:fcc ratio for Au_{561} plotted against the reciprocal of the temperature measured in Kelvin. The green dashed line shows a weighted least squares fit to the high temperature region. The equation of this line is: y=mx+c where m=-510±240 K and c=-0.2±0.4

The calculated energy difference of 0.04 eV is very small (corresponding to ≈190°C) and means that within this size range, 561±14, the Dh and fcc isomers are closely competing. This is in qualitative agreement with several [21, 24, 25] theoretical calculations which predict the Dh and fcc isomers to be competing at this size. Molecular dynamic simulations by Baletto et al [24] determined that the

crossover size for Dh-fcc is 500 atoms and that the Dh and fcc isomers remain close in energy whilst the Ih is not favoured above 100 atoms. Chen et al [25] also found that fcc is the lowest energy structure for this size range; the truncated octahedron is the lowest energy structure with the octahedron, truncated decahedron and Ih only ≈ 0.01 eV higher in energy. In a global optimisation study by Goedecker et al [21] similar differences in energy between isomers were calculated to what we have determined experimentally. For example, it was found that a truncated octahedron Au cluster with 201 atoms is 0.007 eV higher in energy than a 192 atom Marks decahedron cluster and similarly, that a 140 atom Au truncated octahedral cluster is equal in energy to a 146 atom Marks decahedron cluster. These very small differences in energies between isomers explains the experimental observation of Dh and fcc isomers at room temperature.

When comparing the experimental result to theoretical calculations, the assumption that structures can be classified generally as Dh or fcc must be carefully considered. In the majority of the theoretical calculations discussed above, the energy of a specific structure and size is calculated. By comparison, for the experimental work discussed here there is a range of sizes (547-575 atoms), and within the classification of Dh or fcc there may be many different truncations and arrangements of atoms on the surface. If in fact our fcc or Dh 'basin' consists of many different structural isomers, then the experimental determination of the energy difference between Dh and fcc as described here, becomes less meaningful.

Decahedral particles can be considered as multiply twinned fcc domains. This should not impact the determination of the energy difference between Dh and fcc structures because the twinning of fcc domains results in increased internal strain, hence the energy associated with Dh and fcc particles will be different. It is important to note that in this thesis, where a cluster is classified as fcc, it refers to single crystal fcc (truncated-octahedra) and not twinned or multiply twinned fcc structures.

4.4 Summary

In summary, we have used a heating stage in the aberration-corrected STEM to make variable temperature measurements of the proportion of structural isomers in a population of Au_{561} clusters. We have identified two distinct regions. In the low temperature region, from 20-125°C, there is a decrease in the Dh:fcc ratio. We attribute this to the transformation of trapped metastable Dh to ground state (lowest free energy) fcc structures. In the high temperature region, from 125-500°C, the Dh: fcc ratio increases; the Dh isomer is repopulated and the system is in equilibrium. By considering the ratio of the partition functions of Dh and fcc basins, we were able to calculate the energy difference between Dh and fcc isomers from the high temperature region of the data. We found that the Dh isomer is 0.04±0.02eV higher in energy than the fcc for Au_{561}. This result is in good qualitative agreement with the theoretical studies of Baletto et al [24] and Chen et al [25] that both report that fcc (T-Oh) and Dh structures are closely competing in this size regime. Ultimately, this method allows for a direct comparison with theoretical studies and provides an experimental method for quantitatively mapping the potential energy surface of size-selected clusters.

References

[1] M Turner, V B Golovko, OP H Vaughan, P Abdulkin, A Berenguer-Murcia, M S Tikhov, B F G Johnson, and R M Lambert. Selective oxidation with dioxygen by gold nanoparticle catalysts derived from 55-atom clusters. *Nature*, 454(7207):981–3, 2008.

[2] M Cully. Drug delivery: nanoparticles improve profile of molecularly targeted cancer drug. *Nature Reviews Drug Discovery*, 15(4):231, 2016.

[3] S S Agasti, A Chompoosor, C You, P Ghosh, C K Kim, and V M Rotello. Photoregulated release of caged anticancer drugs from gold nanoparticles. *Journal of the American Chemical Society*, 131:5728–5729, 2009.

[4] K Saha, S Agasti, C Kim, X Li, and V M Rotello. Gold nanoparticles in chemical and biological sensing. *Chemical Reviews*, 112(5):2739–79, 2012.

[5] F Baletto and R Ferrando. Structural properties of nanoclusters: Energetic, thermodynamic, and kinetic effects. *Reviews of Modern Physics*, 77:371–417, 2005.

[6] C T Campbell. The active site in nanoparticle gold catalysis. *Science*, 306(5694):234–5, 2004.

[7] A Wiesel, N Drebov, T Rapps, R Ahlrichs, U Schwarz, R Kelting, P Weis, M M Kappes, and D Schooss. Structures of medium sized tin cluster anions. *Physical Chemistry Chemical Physics*, 14:234, 2012.

[8] I Barke, H Hartmann, D Rupp, L Flu, M Sauppe, M Adolph, S Schorb, C Bostedt, R Treusch, C Peltz, S Bartling, and T Fennel. The 3D-architecture of individual free silver nanoparticles captured by X-ray scattering. *Nature Communications*, 6(6187):1–7, 2015.

[9] K Koga and K Sugawara. Population statistics of gold nanoparticle morphologies: direct determination by HREM observations. *Surface Science*, 529(1-2):23–35, 2003.

[10] Z Y Li, N P Young, M Di Vece, S Palomba, R E Palmer, A L Bleloch, B C Curley, R L Johnston, J Jiang, and J Yuan. Three-dimensional atomic-scale structure of size-selected gold nanoclusters. *Nature*, 451(7174):46–8, 2008.

[11] Z W Wang and R E Palmer. Determination of the ground-state atomic structures of size-selected Au nanoclusters by electron-beam-induced transformation. *Physical Review Letters*, 108(24):245502, 2012.

[12] D Wells, G Rossi, R Ferrando, and R E Palmer. Metastability of the atomic structures of size-selected gold nanoparticles. *Nanoscale*, 7:6498–6503, 2015.

[13] Z W Wang and R E Palmer. Experimental evidence for fluctuating, chiral-type Au_{55} clusters by direct atomic imaging. *Nano Letters*, 12:5510–5514, 2012.

[14] Z W Wang and R E Palmer. Direct atomic imaging and dynamical fluctuations of the tetrahedral Au_{20} cluster. *Nanoscale*, 4(16):4947–9, 2012.

[15] M P Ajayan and L D Marks. Experimental evidence for quasimelting in small particles. *Physical Review Letters*, 63(3), 1989.

[16] K Koga, T Ikeshoji, and K Sugawara. Size-and temperature-dependent structural transitions in gold nanoparticles. *Physical Review Letters*, 92(11):115507, 2004.

[17] S Pratontep, S J Carroll, C Xirouchaki, M Streun, and R E Palmer. Size-selected cluster beam source based on radio frequency magnetron plasma sputtering and gas condensation. *Review of Scientific Instruments*, 76(4):045103, 2005.

[18] B von Issendorff and R E Palmer. A new high transmission infinite range mass selector for cluster and nanoparticle beams. *Review of Scientific Instruments*, 70(12):4497, 1999.

[19] M Di Vece, S Palomba, and R Palmer. Pinning of size-selected gold and nickel nanoclusters on graphite. *Physical Review B*, 72(7):073407–1–4, 2005.

[20] S R Plant, L Cao, and R E Palmer. Atomic structure control of size-selected gold nanoclusters during formation. *Journal of the American Chemical Society*, 136(21):7559–7562, 2014.

[21] K Bao, S Goedecker, K Koga, F Lançon, and A Neelov. Structure of large gold clusters obtained by global optimization using the minima hopping method. *Physical Review B*, 79(041405(R)):1–4, 2009.

[22] A Silva. Atomic structure and dynamics of size-selected metal clusters, 2016.

[23] F Calvo, J P K Doye, and D J Wales. Equilibrium properties of clusters in the harmonic superposition approximation. *Chemical Physics Letters*, 366(1-2):176–183, 2002.

[24] F Baletto, R Ferrando, A Fortunelli, F Montalenti, and C Mottet. Crossover among structural motifs in transition and noble-metal clusters. *The Journal of Chemical Physics*, 116(9):3856–3863, 2002.

[25] B Wang, M Liu, Y Wang, and X Chen. Structures and energetics of silver and gold nanoparticles. *The Journal of Physical Chemistry C*, 115(23):11374–11381, 2011.

Chapter 5

In Situ ac-STEM of Surface Melting in Supported Au Nanoclusters Below 5nm

In this chapter surface melting of Au clusters between 2 and 5 nm on an amorphous-carbon support is investigated and interpreted in relation to models of melting point suppression. A magnetron sputtering gas aggregation cluster source with LTOF mass filter was used for production of size-selected clusters. Heating of the samples was performed in-situ using a DENS solutions Wildfire heating holder for the STEM and samples were characterised using HAADF and BF ac-STEM. The content of this chapter is taken largely from a draft version of a paper written by the author (with suggestions from R Palmer). Production of size-selected cluster samples, STEM imaging, and structural analysis was performed by the author.

5.1 Overview

The behaviour of Au nanoparticles at elevated temperatures is interesting from a fundamental perspective and is also relevant to the topic of catalysis. It is well known that gold nanoparticles exhibit catalytic activity at the nanoscale [1]. Understanding their morphology and surface structure under relevant reaction conditions,

such as elevated temperature, may prove useful in the design of catalyst materials. Melting point suppression at the nanoscale [2] is a well established phenomenon. First predicted by Pawlow in 1908 [3] and detected experimentally by Takagi in 1954 via shape changes in the diffraction rings of a nanoparticle ensemble [4], a 1/r dependence of melting temperature at the nanoscale holds true for all but a few materials [5, 6]. Early experimental observations of melting point suppression in supported Au nanoparticles were reported in the seminal electron diffraction study by Buffat and Borel [7], as well as in a TEM evaporation rate investigation by Sambles [8]. Subsequently there have been several experimental studies of the high temperature behaviour of gold nanoparticles. However, at present there is only very limited [9] single particle, time resolved data on the melting point, with no data below 5nm - a catalytically relevant size regime [10]. Additionally, because previously reported experimental studies of Au nanoparticle melting do not track the particles in real space as the temperature is increased (instead they use static temperature evaporation or diffraction methods), the exact mechanism by which melting occurs (homogeneous/liquid shell/LNG) remains unknown.

There are several theoretical models for melting point suppression at the nanoscale. Pawlow's theory is a thermodynamic model based on the triple point equilibrium of spherical solid and liquid particles of the same material and equal mass, surrounded by their vapour. The liquid shell model, LNG model and numerous molecular dynamics studies of Au [11, 12, 13, 14, 15] and other metal [16, 17, 18] nanoparticles predict the formation of a liquid shell as a mechanism for nanoparticle melting. The liquid shell model, first suggested by Reiss and Wilson [19] and developed by others [20, 21] including Sambles [8], is a thermodynamic model that assumes a solid core surrounded by a liquid shell of constant thickness in the proximity of the melting temperature. The LNG model, proposed by Couchman and Jesser [22], is based on nucleation theory and describes melting as the nucleation of a liquid shell on the surface of the nanoparticle that spreads into the core until a critical radius is reached and the whole particle melts. The model predicts a melting region in which

there is solid-liquid coexistence. There has been no experimental observation of the existence of a liquid shell prior to melting for Au nanoparticles. Young et al [23] reported surface roughening (amorphous regions) in 10.2nm diameter Au particles at >600°C, however a liquid shell was not observed in this case. Such a solid core, liquid shell structure and solid-liquid coexistence have been reported for lead [24], platinum [25] (not with atomic resolution), and most recently for large gallium nanoparticles at room temperature [26].

Here we observe the behaviour of individual, size-selected Au nanoclusters ($\leq$5nm) in real space with atomic resolution as their temperature is increased up to 1000°C using in-situ heating in the ac-STEM. Shape changes observed in the nanoparticles as the temperature is ramped are used as an indicator of the surface melting temperature for individual particles. Prolonged loss of core atomic structure is used, where possible, to estimate the core melting temperature. The results are compared with Pawlow's model, the liquid shell model and the LNG model for melting point suppression. It was found that the complete cluster (core) melting temperature is much higher than predicted by all the models of melting point suppression. The STEM images reveal the formation of a quasi-liquid shell that wets the substrate and persists over a range of temperatures, supporting the theory of a liquid shell melting mechanism and the coexistence of solid and liquid phases.

5.2 Experimental Methods

Size-selected Au nanoclusters were prepared using a magnetron sputtering, gas aggregation cluster source [27] with lateral time of flight mass filter [28]. ($M/\Delta M$=22). Clusters containing either 309$\pm$7 or 561$\pm$13 Au atoms were deposited onto amorphous carbon membranes of the heating chips, using low deposition energy (soft landing [29]) to preserve their original structures.

STEM imaging was performed using a 200keV JEOL 2100F instrument with spherical aberration corrector (CEOS). A high angle annular dark field (HAADF) detector with inner collection angle of 62 mrad, and a bright field detector were employed

for imaging. Use of the HAADF detector enabled any aggregate particles to be accurately sized by using the size-selected clusters as 'mass-standards' [30].

For in-situ heating a DENS solutions Wildfire heating holder was used in conjunction with MEMS-based heating chips. The chips featured ≈5 nm thick amorphous carbon membranes, on which the Au nanoparticles were deposited. Heating experiments were performed by STEM imaging of individual particles at incrementally increasing temperatures. The surface melting temperature of the nanoparticles was deduced by observing shape changes that were not consistent purely with rotations of the particle (compared against simulation atlases [31] showing particles at different angles of orientation). For example, when a shape change is observed, the surface melting temperature for that particle is recorded as directly in-between the temperature of the last observed 'original-shape' particle and first 'shape-changed' particle.

The error on the surface melting temperature is a function of the temperature window in which the shape change occurred and the temperature stability of the MEMS heating chip, which is essentially negligible in comparison (<0.1°C). Another source of error arises from the calibration of the heating chip; there may be a systematic error - an offset of up to 5% on the stated temperature. This systematic error effects the accuracy of all temperature measurements. However, so long as measurements are made using the same heating chip the general trend (melting temperature vs particle size) should not be affected.

5.3 Results

Figures 5.1 and 5.2 both show examples of shape changes that occur in the Au nanoparticles at high temperatures. Figure 5.1 shows a Au_{561} particle which is heated incrementally from 550°C to 1000°C. The selection of frames shown in the figure is taken from a series of 22 HAADF STEM images of this particle. The first observation of a shape change is at 657°C where there is a protrusion from the cluster surface, indicative of surface melting. Beyond 657°C, one can see that the

shape of the nanoparticle is continually changing and is no longer consistent with the shape of an 'as deposited' cluster at room temperature (see images in chapter 3 for reference). Despite the shape changes in the nanoparticle, the core atomic structure is still visible up to 962°C.

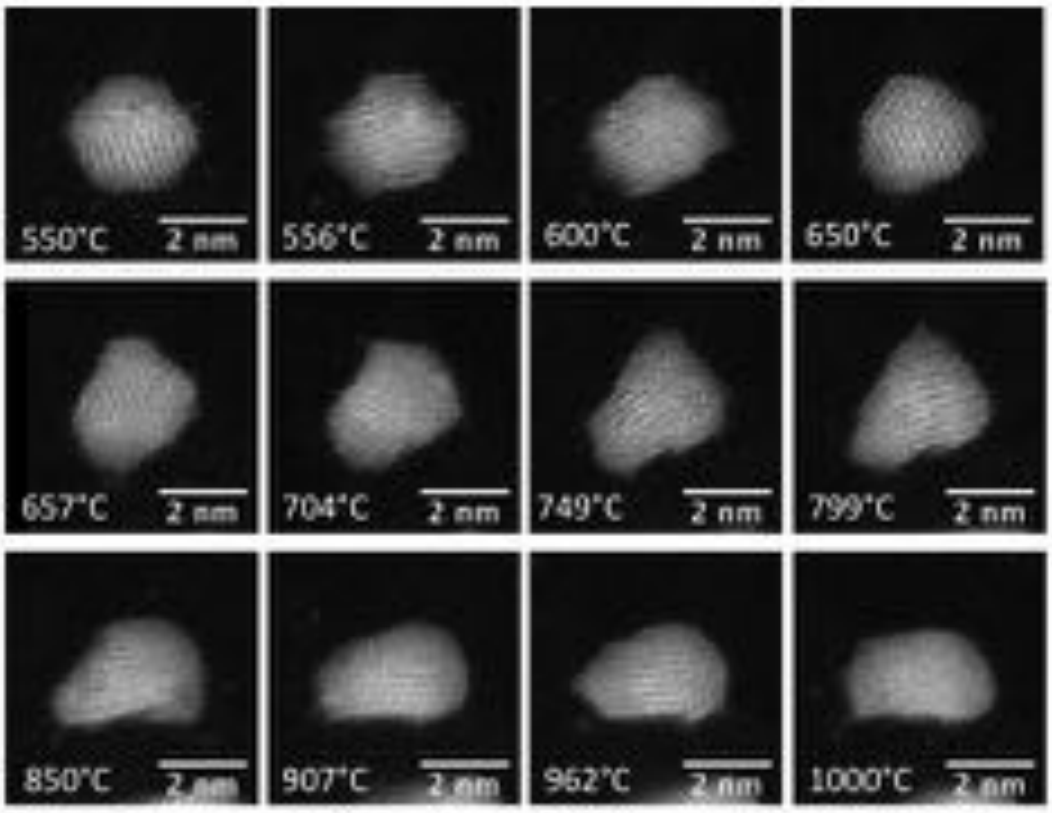

Figure 5.1: Selected images from a series of HAADF STEM images of an individual Au_{561} particle at high temperature (550°C - 1000°C).

Similarly, Figure 5.2 shows a Au_{2530} particle heated from 650°C to 1000°C. Again, the selection of frames shown here are taken from a series of 22 HAADF STEM images. This particle has been formed by aggregation and its size has been determined using the size-selected Au_{561} clusters as mass balances (using the HAADF intensity). In this case the first shape change is seen at 801°C. Beyond this temperature, small fluctuations in the shape of the nanoparticle surface can be seen. The core atomic structure is still present at 1000°C, although certain regions around the cluster surface appear amorphous.

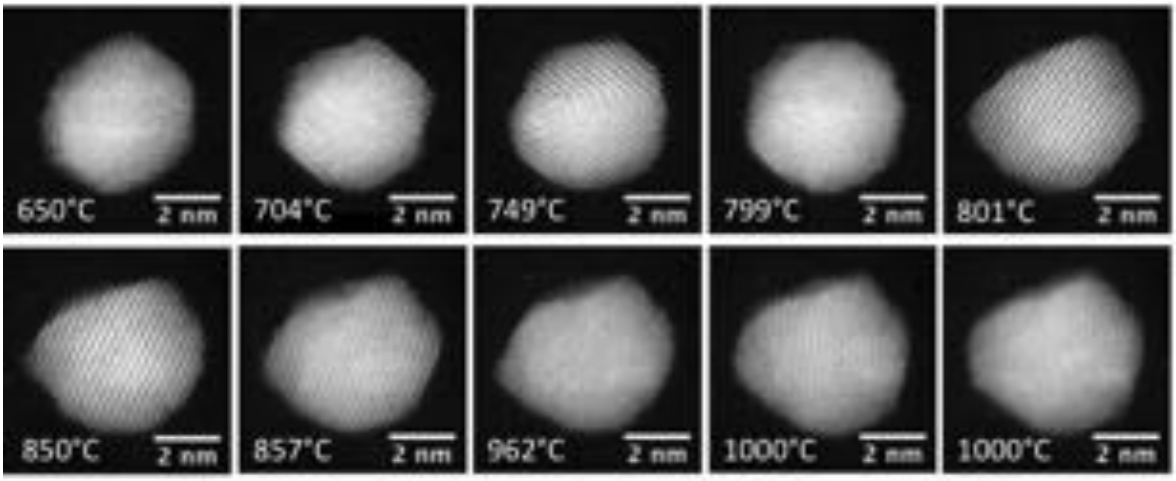

Figure 5.2: Selected images from a series of HAADF STEM images of an individual Au_{2530} particle at high temperature (650°C - 1000°C).

The size-selected clusters used in this experiment are deposited onto an amorphous carbon film and this may effect the melting temperature and/or mechanism. BF images of the clusters were recorded simultaneously with the HAADF images in this work so that changes to the a-carbon substrate could be observed. Figure 5.3 shows two bright field ac-STEM images of a Au_{561} cluster (the same particle is shown in figure 1) taken at 550°C and 962°C, before and after surface melting. At 550°C the cluster shape and structure is consistent with that of a free Ino-decahedron, implying that the cluster is in minimal contact with the carbon substrate, at 962°C the cluster has wet the substrate and several layers of carbon appear to have nucleated on the cluster surface.

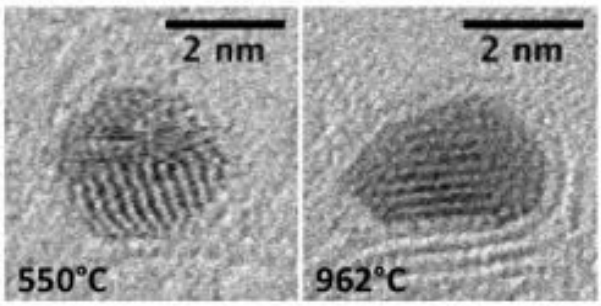

Figure 5.3: Bright field STEM images of a Au_{561} nanoparticle taken at 550°C (left) and 962°C (right).

Figures 5.4 and 5.5 show two examples of the formation of a quasi-liquid layer at the cluster surface and the coexistence of solid and liquid phases at high temperatures. Figure 5.4A shows a series of HAADF STEM images of an Au_{1110} particle at high temperature. At 704°C and 749°C the particle appears to be solid and is consistent with the shape of a cuboctahedron. At 799°C the particle still appears to be solid but the shape is consistent with that of a decahedron, indicating that a structural transition has occurred. The particle's shape changes dramatically at 801°C, indicating that the surface is molten. One can see that a solid core-liquid shell structure is formed, with the liquid layer wetting the substrate. Figure 5.4B shows a profile plot of the HAADF intensity of the Au_{1110} particle at 1000°C. The arrow indicates the drop in intensity (hence in projected atom density) at the edge of the solid core. Figure 5.5A shows a series of HAADF STEM images of a Au_{561} particle beyond the temperature at which shape changes are first observed. At 650°C a protrusion on the surface of the particle indicates that the surface is partially molten, however by 801°C a visible complete liquid shell-solid core structure has formed and the liquid shell has wet the substrate resulting in the dramatic shape change. The shape of the liquid shell appears to fluctuate, with a near spherical shape being temporarily recovered at 899°C. Figure 5.5B shows a profile plot of the HAADF intensity of the Au_{561} particle at 857°C.

For both the particles in figures 5.4 and 5.5 it can be seen that the core atomic structure of the particle persists after both surface melting and after the wetting of the liquid layer on the substrate. For the Au_{561} particle (Fig 5.5) the atomic structure is only present in the core and the shell appears amorphous. However, for the larger Au_{1110} particle the fcc structure persists up to 900°C and is present in both the core and shell with only small amorphous regions existing at the very edges of the particle (indicated by arrows in fig 5.4A). The high contrast images shown in 5.4C further highlight the structure of the liquid shell. At 850°C both amorphous and structures regions exist at surface, whilst at 899°C the entire outer shell appears amorphous.

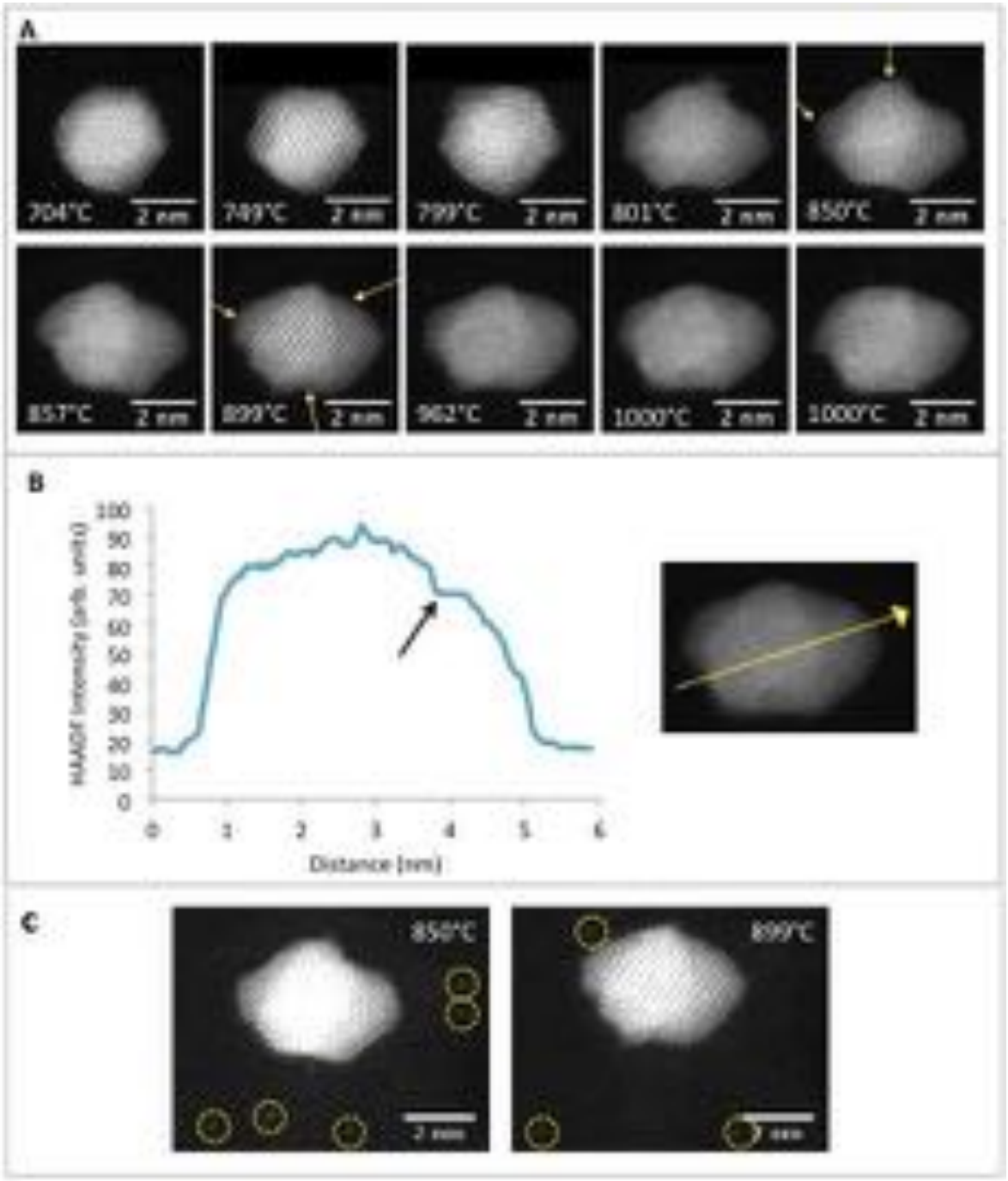

Figure 5.4: HAADF STEM images and corresponding profile plots of an Au_{1110} nanoparticle, showing the formation of a liquid shell at high temperatures. A) HAADF STEM images of an Au_{1110} particle at between 704°C and 1000°C). Amorphous regions at the edges of the particle are highlighted by yellow arrows. B) A line profile plot of the HAADF intensity across the particle in A at 1000°C. The yellow arrow on the HAADF image indicates the direction and location of the line profile (image smoothed by a mean filter). C) High contrast images for viewing amorphous regions and single atoms (marked by yellow rings).

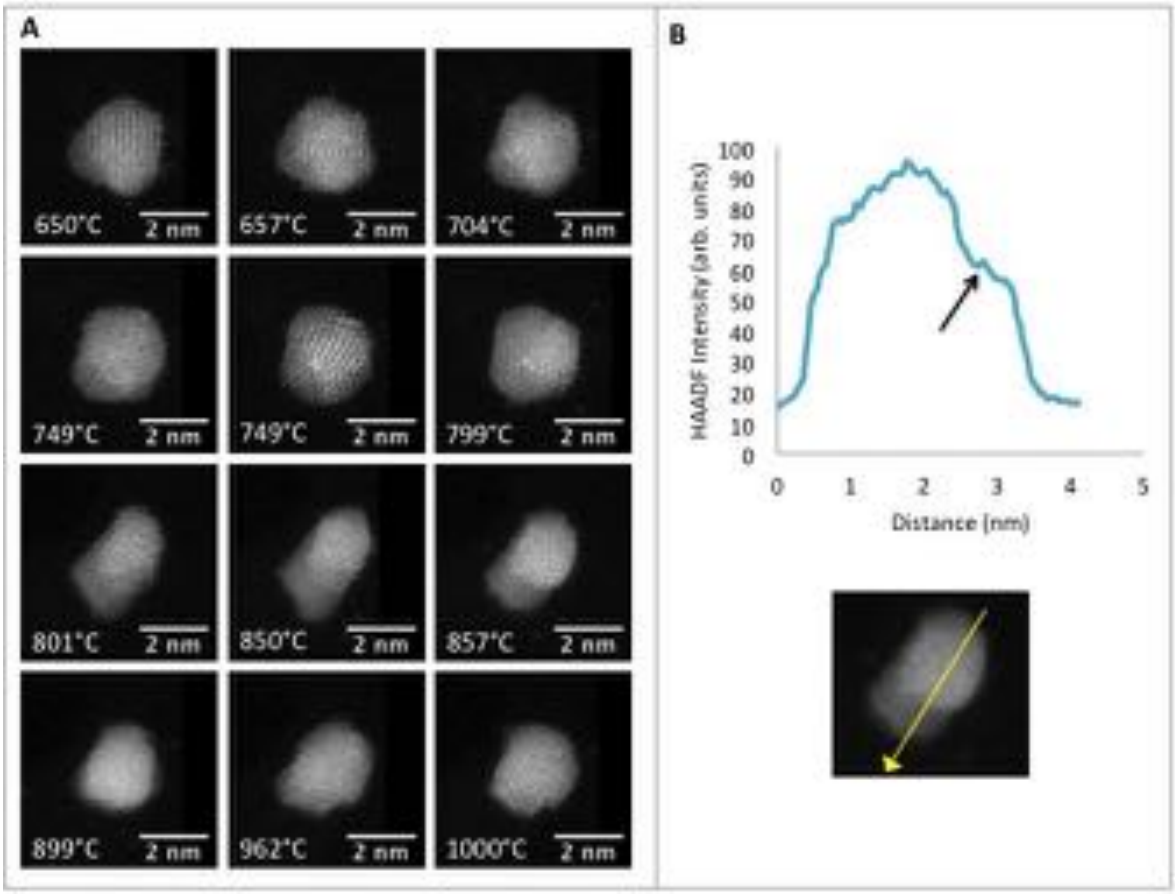

Figure 5.5: HAADF STEM images and corresponding profile plots of Au_{561} nanoparticle, showing the formation of a liquid shell at high temperatures. A) HAADF STEM images of an Au_{561} particle between 650°C and 1000°C. B) A line profile plot of the HAADF intensity across the particle in A at 857°C. The yellow arrow on the inset HAADF image indicates the direction and location of the line profile.

Throughout all the experimental data, structural transitions during heating were observed, but there was no evidence of an Ih or Ih solid-liquid csoexistence state prior to melting - a widely predicted phenomenon [12, 32, 33]. Nor was there evidence of a rapidly fluctuating quasi-molten state as has been predicted and observed in several studies [23, 34, 35, 36]. All experimental reports of quasi-melting in the literature were observed with HRTEM. It is possible that the geometry of imaging in HRTEM promotes quasi-melting. In the HRTEM, although the beam is spread, the overall dose received by the cluster may be higher because the sample is continually irradiated. By comparison, in the STEM the cluster is only irradiated whilst the

convergent beam scans over it during imaging, which may result in a lower overall dose being delivered to the cluster. The difference in the continuity of the electron beam irradiation of the cluster, or the overall dose, could explain why quasi-melting is not seen in the STEM study presented in this thesis. This would suggest that it is the electron beam irradiation that promotes quasi-melting and not purely sample heating.

After heating to 1000°C the Au_{561} sample was then slowly cooled (over $\approx$ 15 minutes) to room temperature (23°C). Several of the particles were then imaged again. Figure 5.6 shows 3 examples of particles at 1000°C and after cooling back down to room temperature. The particle in A/D is the same as in fig 5.1, the particle in B/E is the same as in fig 5.4 and the particle in C/F is the same as in fig 5.7. The particle shown in figure 5.8 disappeared upon cooling, and it is clear from the figure that the size of the particle in A/D has significantly decreased. This is most likely due to sublimation, Ostwald ripening, or in the case of the disappeared particle, coalescence. It can also be seen, that upon cooling, the clusters regain a near-spherical shape and visible lattice structure across the entirety of the particles.

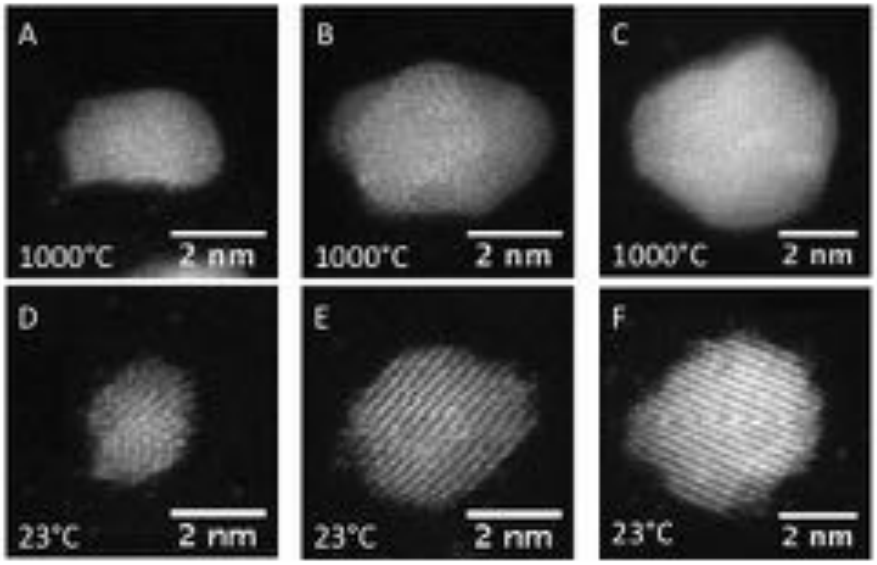

Figure 5.6: HAADF STEM images of Au clusters at 1000°C and after slowly cooling to 23°C. A, B and C show 3 different particles at 1000°C and D, E and F show the same 3 particles at 23°C .

5.4 Discussion

There are two ways in which the melting temperature of a nanoparticle can be measured using in-situ heating in the STEM. The first would be to use the loss of lattice structure in the images as an indication of melting [9]. The second is to use changes in shape - a method that arises directly from the data collected here (although shape changes have been used to describe melting previously in field emission experiments [37]. For our study the criteria of the loss of atomic structure was not suitable due to the time resolution of the experiments (each image taking 5.4s to record); the phenomenon of quasi-melting below the melting point, where the particle structure rapidly fluctuates, has been reported in both experimental and theoretical studies [34, 35]. If this were to occur the rapidly fluctuating particle is likely to appear amorphous in the recorded STEM image and could be misinterpreted as being molten. Therefore, for this work, shape changes in the particles will be used to identify surface melting; whereas a free particle should become spherical when molten, the particles studied here are on a substrate, meaning that as the cluster surface melts the liquid surface layer wets the substrate resulting in the dramatic shape changes such as those seen in figures 5.1-5.5.

Looking back at figure 5.1, the shape changes are observed at temperatures $\geq$657 °C. Therefore, for this particle the surface melting temperature is estimated as 654$\pm$4°C, directly halfway between the temperature of the last 'original-shape' particle and the first 'shape-changed' particle. Similarly, for the particle in figure 5.2, the surface melting temperature is recorded as 800$\pm$1°C (between images recorded at 799°C and 801°C). The error stated here does not include the potential systematic error of <5% arising from the heating chip calibration. This analysis was applied to all of the 9 clusters studied. To avoid a cluster rotation or structural transformation being misinterpreted as a shape change, simulation atlases for fcc, Ih and Dh clusters at different angles of orientation were referenced.

Figure 5.7 shows the results of our single particle analysis of the surface melting temperature as a function of the reciprocal of the cluster radius, r. Where possible,

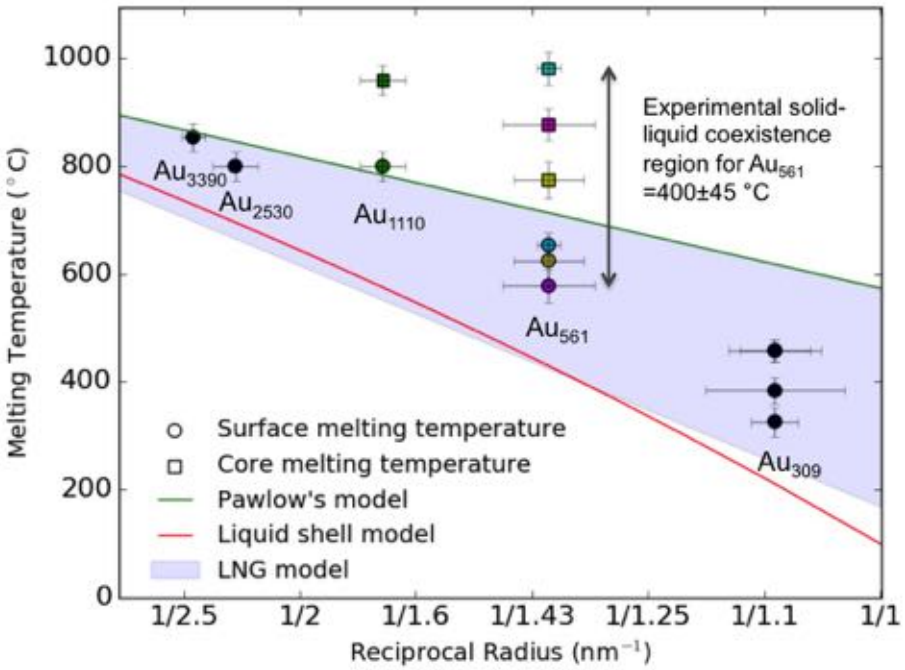

Figure 5.7: Experimental, single particle measurements of surface and core melting temperatures in Au nanoparticles, plotted alongside several models for melting point suppression. The experimental data is represented by scatter points: circles show surface melting temperatures and squares show core melting temperatures. The cluster sizes in number of atoms are indicated on the plot and the corresponding core and surface melting temperatures have the same colour. The solid green line is Pawlow's model from reference 38, the solid red line is the liquid shell model from reference 8 and the blue region is the liquid nucleation and growth model melting sector from references 22 and 39.

core (complete) cluster melting temperatures are also shown, measured by observing the loss of core atomic structure by eye from the HAADF images and their FFT's. Pawlow's triple point model [3], the liquid shell model [8] and the LNG model [22] are also plotted for comparison. The equations and parameters used to plot these models are presented in appendix B. For the liquid shell model the smallest possible shell thickness of 2.7Å (the atomic diameter) is used. The circular points are measurements of the surface melting temperature of size-selected Au_{309} and Au_{561} particles, and aggregated Au_{1110}, Au_{2530} and Au_{3390} particles. The squares show core melting temperatures, where such a measurement was possible, and the colours

indicate the corresponding surface and core measurements for an individual particle. The error on the surface melting temperature includes both the error arising from the temperature window and the 5% heating chip calibration error, both of which are described in more detail in the methods section. The particle radius was calculated by making four separate measurements of the average particle diameter, then taking the mean value; the error is given by the maximum and minimum of these values. Both are shown by error bars in the figure.

Pawlow's model is for complete particle melting, therefore it is reasonable to assume that our surface melting measurements should fall below those predicted by this model. Indeed this is the case for all but one particle (Au_{1110}). However, the experimentally measured core melting temperatures are much higher than predicted by Pawlow's model. The liquid shell model predicts significantly lower whole particle melting temperatures than Pawlow's model across our size range, as well as a shifting down of the curve for small particles. The melting temperatures predicted by this model are much lower than those observed in the experimental data for both surface and core melting. Furthermore, our ac-STEM images (see figures 5.4 and 5.5) show that the liquid shell thickness varies between particles and is generally greater than 1 atomic layer. Increasing the atomic shell thickness in the liquid shell model results in a greater degree of melting point suppression for small particles sizes, something which is not mirrored by the experimental data - to which a straight line is a good fit (T_m=-904/r+1245°C, R^2=0.9). The liquid nucleation and growth model predicts a melting region (see fig 5.7), where the lower boundary is representative of the onset of surface melting and the upper boundary is the point by which the complete particle should be molten. Within this region solid and liquid phases coexist, and complete melting may occur at any point. Again, both our surface and core melting temperature measurements are higher than those predicted by this model. However, the liquid nucleation and growth model is in good qualitative agreement with our data; our repeated single particle measurements show that surface melting and solid-liquid coexistence occurs over a temperature range (see fig 5.4).

When comparing the experimental data with the theoretical models it is important to consider the influence of the substrate. Naturally, wetting of liquid surface at high temperatures will result in an increase in contact between the cluster and the carbon substrate. Additionally, figure 5.3 showed that at high temperatures layers of carbon may nucleate around the cluster. This level of contact with the carbon substrate may effect the cluster's melting temperature; for the cluster shown in the figure, the atomic structure of the core is still visible at 962°C, much higher than the complete melting temperature predicted by all three models. Similarly, for the other Au_{561} clusters, core atomic structure is still visible at 749°C and 847°C, for the Au_{1110} at 957°C and for the Au_{2530} and Au_{3390} clusters up to 1000°C (the highest measured temperature), implying a core melting temperature much higher than predicted by the models discussed above. One explanation for this is that after surface melting (and wetting), the increased contact with the carbon substrate stabilises the cluster. It is also possible that the carbon and gold are mixing at the surface of the particles, thus altering the melting temperature. In the future, the role of gold and carbon mixing could be further investigated by STEM-EELS measurements and analysis of the carbon K-edge before and after surface melting of the clusters.

It is important to note that the degree of formation of the solid core-liquid shell structure (as seen in fig 5.4) does vary from cluster to cluster, yet it is clear in all cases that melting initiates at the surface of the particle. This mechanism for melting is consistent with the liquid nucleation and growth model, however a comparison of our experimentally measured critical core radii (see figure 5.8) with those predicted by the model show some significant differences. Experimentally, we observe a much lower limit on the critical core radius and a much higher upper limit on the core melting temperature. More generally, we find a much larger solid-liquid coexistence region compared with the liquid nucleation and growth model (see figure 5.7).

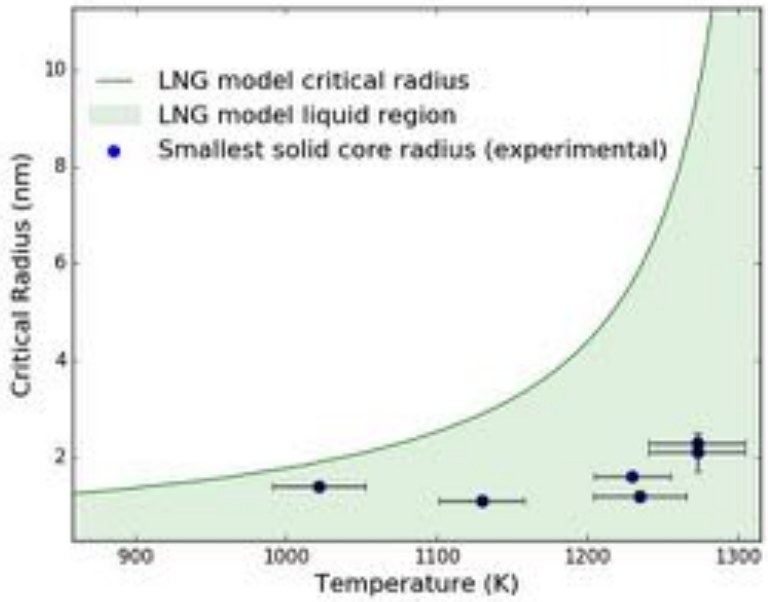

Figure 5.8: The LNG model critical radius is plotted (green line), the region below the curve (filled green) is the liquid region (core and surface) as predicted by the model. Experimental measurements of the smallest solid core sizes observed are also plotted (blue scatter points).

5.5 Summary

In summary, in situ heating experiments on 2-5nm Au clusters have been performed in the aberration corrected STEM, demonstrating melting point suppression and surface initiated melting. Surface melting has been directly observed in real space, and the formation of a solid core liquid shell structure at high temperatures has been discovered. Whilst the results are in good qualitative agreement with the liquid nucleation and growth model, the experimental solid liquid coexistence region is found to be much larger than predicted by the model.

References

[1] A Corma and H Garcia. Supported gold nanoparticles as catalysts for organic reactions. *Chemical Society Reviews*, 37(9):2096–126, 2008.

[2] M Schmidt, R Kusche, B von Issendorff, and H Haberland. Irregular variations in the melting point of size-selected atomic clusters. *Nature*, 393(6682):238–240, may 1998.

[3] P Pawlow. The dependency of the melting point on the surface energy of a solid body. *Z. Phys. Chemie*, 65:545–548, 1909.

[4] M Takagi. Electron-diffraction study of liquid-solid transition of thin metal films. *Journal of the Physical Society of Japan*, 9(3):359–363, 1954.

[5] A Shvartsburg and M Jarrold. Solid clusters above the bulk melting point. *Physical Review Letters*, 85:2530–2532, 2000.

[6] G A Breaux, R C Benirschke, T Sugai, B S Kinnear, and M F Jarrold. Hot and solid gallium clusters: too small to melt. *Physical Review Letters*, 91(21):215508, 2003.

[7] Ph Buffat and J P Borel. Size effect on the melting temperature of gold particles. *Physical Review A*, 13(6):2287–2298, 1976.

[8] J R Sambles. An electron microscope study of evaporating gold particles: the Kelvin equation for liquid gold and the lowering of the melting point of solid gold particles. *Proceedings of the Royal Society A: Mathematical, Physical and Engineering Sciences*, 324(1558):339–351, 1971.

[9] J Lee, J Lee, T Tanaka, and H Mori. In situ atomic-scale observation of melting point suppression in nanometer-sized gold particles. *Nanotechnology*, 20(47):475706, 2009.

[10] M Turner, V B Golovko, OP H Vaughan, P Abdulkin, A Berenguer-Murcia, M S Tikhov, B F G Johnson, and R M Lambert. Selective oxidation with dioxygen by gold nanoparticle catalysts derived from 55-atom clusters. *Nature*, 454(7207):981–3, 2008.

[11] J-H Shim, B-J Lee, and Y W Cho. Thermal stability of unsupported gold nanoparticle: a molecular dynamics study. *Surface Science*, 512:262–268, 2002.

[12] C L Cleveland, W D Luedtke, and U Landman. Melting of gold clusters. *Physical Review B*, 60(7), 1999.

[13] L J Lewis, P Jensen, and J-L Barrat. Melting, freezing, and coalescence of gold nanoclusters. *Physical Review B*, 56(4):2248–2257, 1997.

[14] F Ercolessi, W Andreoni, and E Tosatti. Melting of small gold particles: mechanism and size effects. *Physical Review Letters*, 66(7), 1991.

[15] N Wang, S I Rokhlin, and D F Farson. Nonhomogeneous surface premelting of Au nanoparticles. *Nanotechnology*, 19:415701, 2008.

[16] H S Lim, C K Ong, and F Ercolessi. Surface effects in vibrational and melting properties of Pb clusters. *Zeitschrift für Physik D Atoms, Molecules and Clusters*, 26(1 Supplement):45–47, 1993.

[17] Y Joo Lee, E-K Lee, S Kim, and R Nieminen. Effect of potential energy distribution on the melting of clusters. *Physical Review Letters*, 86(6):999–1002, 2001.

[18] F Calvo and F Spiegelman. On the premelting features in sodium clusters. *Journal of Chemical Physics*, 120(20):9684–9689, 2004.

[19] H Reiss and I B Wilson. The effect of surface on melting point. *Journal of Colloid Science*, 3(6):551–561, 1948.

[20] K J Hanszen. Theoretische untersuchungen uber den schmelzpunkt kleiner kugelchen. *Zeitschrift fur Physik*, 157(5):523–553, 1960.

[21] A E Curzon. *Thermodynamic theory of size dependence of melting temperature in metals*. PhD thesis, Imperial College, Univ. London, 1960.

[22] P R Couchman and W A Jesser. Thermodynamic theory of size dependence of melting temperature in metals. *Nature*, 269(5628):481–483, 1977.

[23] N P Young, M A van Huis, H W Zandbergen, H Xu, and A I Kirkland. Transformations of gold nanoparticles investigated using variable temperature high-resolution transmission electron microscopy. *Ultramicroscopy*, 110(5):506–516, 2010.

[24] Y Lereah, G Deutscher, P Cheyssac, and R Kofman. Direct observation of low-dimensional effects on melting of small lead particles. *Europhysics Letters*, 14(1):87–90, 1990.

[25] Z L Wang, J M Petroski, T C Green, and M A El-Sayed. Shape transformation and surface melting of cubic and tetrahedral platinum nanocrystals. *The Journal of Physical Chemistry B*, 102(32):6145–6151, 1998.

[26] M Losurdo, A Suvorova, S Rubanov, K Hingerl, and A S Brown. Thermally stable coexistence of liquid and solid phases in gallium nanoparticles. *Nature Materials*, 2016.

[27] S Pratontep, S J Carroll, C Xirouchaki, M Streun, and R E Palmer. Size-selected cluster beam source based on radio frequency magnetron plasma sputtering and gas condensation. *Review of Scientific Instruments*, 76(4):045103, 2005.

[28] B von Issendorff and R E Palmer. A new high transmission infinite range mass selector for cluster and nanoparticle beams. *Review of Scientific Instruments*, 70(12):4497, 1999.

[29] M Di Vece, S Palomba, and R Palmer. Pinning of size-selected gold and nickel nanoclusters on graphite. *Physical Review B*, 72(7):073407–1–4, 2005.

[30] N Young, Z Li, Y Chen, S Palomba, M Di Vece, and R E Palmer. Weighing supported nanoparticles: size-selected clusters as mass standards in nanometrology. *Physical Review Letters*, 101(24):246103, 2008.

[31] Z W Wang and R E Palmer. Determination of the ground-state atomic structures of size-selected Au nanoclusters by electron-beam-induced transformation. *Physical Review Letters*, 108(24):245502, 2012.

[32] A S Barnard, N P Young, A I Kirkland, M A Van Huis, and X Huifang. Nanogold : a quantitative phase map. *ACS Nano*, 3(6):1431–1436, 2009.

[33] C L Cleveland, W D Luedtke, and U Landman. Melting of gold clusters : icosahedral precursors. *Physical Review Letters*, 81(10):2036–2039, 1998.

[34] L D Marks and P M Ajayan. Quasimelting and phases of small particles. *Physical Review Letters*, 60(7):585–587, 1988.

[35] M P Ajayan and L D Marks. Experimental evidence for quasimelting in small particles. *Physical Review Letters*, 63(3), 1989.

[36] C-L Kuo and P Clancy. Melting and freezing characteristics and structural properties of supported and unsupported gold nanoclusters. *Journal of Chemical Physics B*, 109:13743–13754, 2005.

[37] T Castro, R Reifenberger, E Choi, and R P Andres. Size-dependent melting temperature of individual nanometer-sized metallic cluster. *Physical Review B*, 42, 1990.

[38] Y G Chushak and L S Bartell. Melting and freezing of gold nanoclusters. *Journal of Physical Chemistry B*, 105:11605–11614, 2001.

[39] G Guenther and O Guillon. Models of size-dependent nanoparticle melting tested on gold. *Journal of Materials Science*, 49(23):7915–7932, 2014.

Chapter 6

Atomic Structure and Ageing of Size-Selected Ag Clusters

In this chapter, the atomic structure of size-selected Ag clusters and the effect of exposure to air on atomic structure and chemical composition are investigated. Samples of size-selected Ag clusters were produced using a magnetron sputtering gas aggregation cluster source with LTOF mass filter. The atomic structure of the clusters was characterised using HAADF STEM and chemical composition investigated by STEM-EELS. In section 6.1, results are presented on the atomic structure of Ag clusters containing 309, 561, 742 and 923 atoms, for comparison with similar results obtained for Au in chapter 3. In section 6.2, ageing of size-selected clusters is investigated. Section 6.2.1 looks at the atomic structure of size-selected Ag clusters for different durations of air exposure and section 6.2.2 presents EELS chemical composition results for size-selected Ag clusters before and after air exposure. The motivation behind this work is related to the importance of understanding how Ag nanomaterials evolve in the environment. Ag nanoparticles are used widely as an antibacterial, meaning they are both in direct contact with humans and released into the environment; understanding how their structure and chemical composition develops is a first step to understanding and avoiding toxicity. More generally, the corrosion of silver nano-structures is of general interest due the use of silver and

silver alloys in electronics.

Production of size-selected cluster samples, STEM characterisation (HAADF imaging, EELS) and structural and chemical analysis was performed by the author. The simulation atlas used to identify the atomic structure of clusters was created by Ray Hu (University of Leuven) using the QSTEM software.

6.1 Atomic Structure of Size-selected Ag Clusters

Size-selected clusters were produced using a magnetron sputtering gas aggregation cluster source [1] with LTOF mass filter [2], operated at a resolution of M/ΔM=22. Samples containing 309 ±7, 561±13, 742±17 and 932±21 atoms were produced for comparison with results presented for Au in chapter 3. The formation conditions known to effect atomic structure were kept the same as for Au in chapter 3; 10W magnetron power, 250mm condensation length and 0.8mbar condensation chamber pressure. In all cases the clusters were soft-landed onto amorphous carbon coated TEM grids to preserve the free gas phase structure as far as possible [3]. Due to the known sensitivity of silver to air (namely sulphur-containing compounds), samples were transferred between the load-lock vacuum chamber of the cluster source and the STEM in inert gas. This was done using the glovebox described in chapter 2. HAADF STEM imaging was performed for all samples, with a minimum of 100 images being taken for each cluster size. The resulting images were analysed using the simulation atlas method [4], to determine the proportion of different classes of atomic structures.

Figure 6.1 shows experimental HAADF STEM images of Ag clusters, matched to simulated HAADF STEM images from the Au simulation atlas [5]. Fig 6.1A shows experimental images of Ag_{561} clusters on the left and the corresponding simulation atlas images on the right. i-ii) shows a cuboctahedron at a (15, 60) rotation, iii-iv) an Ino-decahedron at a (9,10) rotation and v-vi) an Ino-decahedron at a (0, 60) rotation. The final panel (vii) shows a cluster that does not directly match to the simulation atlas. However, it does display a ring-dot feature characteristic of the

Ih structure, and is therefore classified as a partial Ih structure. Similarly, fig 6.1B shows experimental images of Ag_{923} clusters on the left and corresponding simulated images on the right. i-ii) shows a cuboctahedron at a (45,60) rotation, iii-iv) shows a cuboctahedron at a (45,0) rotation, v-vi) shows an Ino-decahedron at a (18,70) rotation and vii) an icosahedron at a (0,20) rotation. For both Fig 6.1a and b the more general classification of the cluster structure (fcc, Dh or Ih) is also shown in the top right hand corner.

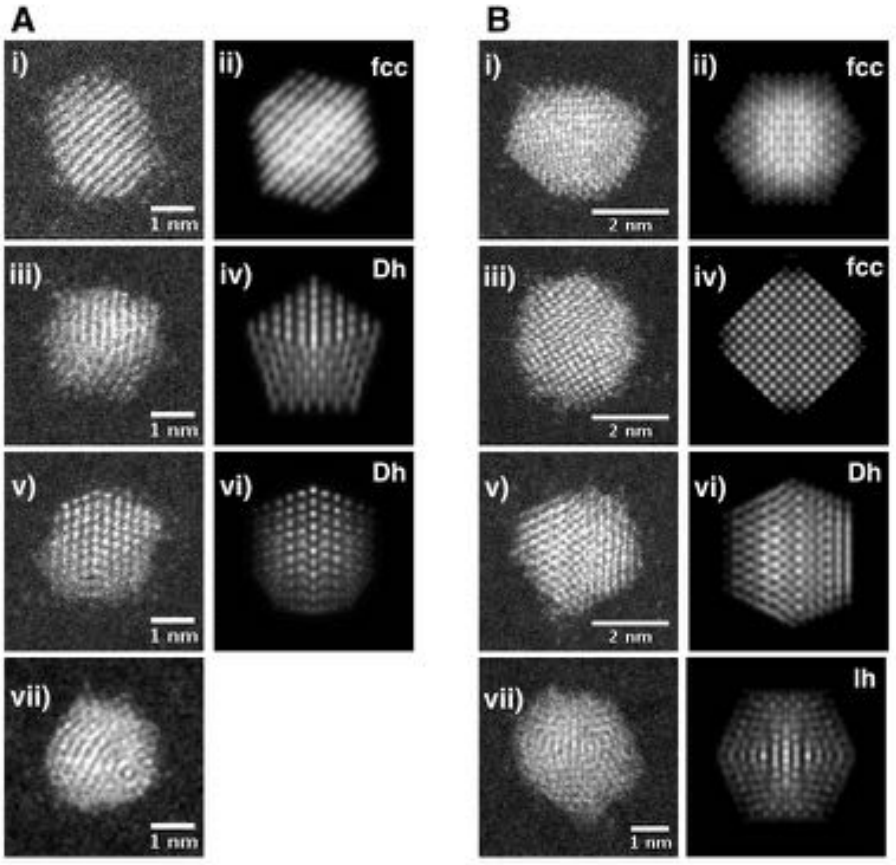

Figure 6.1: Typical HAADF STEM images of size-selected Ag clusters matched to Au simulation atlas images. a) Size 561 and b) size 923

The decision to use the Au simulation atlas was based on a consideration of whether it was necessary to compute a new atlas for Ag. The same geometrical structures are expected for silver as for gold (Cuboctahedron, Ino-decahedron, icosahedron) and it is assumed that the HAADF intensity is linear in atom number for all samples, hence the main difference expected between simulations of Ag and

Au structures is in the overall scaling of the intensity (Ag has a lower atomic number than Au). Because comparisons between experimental images and the simulation atlas are made by eye, a difference in intensity would not alter a structural identification. Indeed, figure 6.1 shows that experimental images of Ag clusters match well to the Au atlas. To confirm that there are no significant differences (by eye) between simulated images of Au and Ag clusters, several sample rotations of the Ag cuboctahedron, Ino-decahedron and icosahedron were simulated using QSTEM software [5]. It was found that there were no qualitative differences between the simulations. Based on these factors it was deemed unnecessary to produce a new simulation atlas based on Ag models of cuboctahedron, Ino-decahedron and icosahedron.

Figure 6.2a shows the proportion of atomic structures for size-selected Ag clusters containing 309±7, 561±13, 742±17 and 923±21 atoms. Similarly to the Au analysis, the structures are classified generally as fcc, Dh, Ih and UI/A. For sizes 309, 561 and 742, fcc is the dominant isomer, followed by Dh, with very few Ih (Ih classification includes partial-Ih). For size 923, the Dh is the dominant isomer, closely followed by fcc (36% vs. 38%), with very few Ih. The proportion of UI/A clusters is almost identical for sizes 561, 742 and 923, but more than double for size 309. This is most likely due to the small size resulting in increased instability (rotations and structural changes) of the clusters under the electron beam. Fig 6.2b shows the Dh:fcc ratio versus cluster size; there is a gradual increase in this value from 0.3±0.1 at size 309 to 1.1±0.2 at size 923.

The Dh:fcc ratio increases with size, this is notably different from gold for which (under the same formation conditions) the Dh:fcc ratio was constant between 561 and 923 atoms. This result shows that for Ag, kinetic trapping of structures does not occur by atom by atom growth on a seed structure - or at least that it is not the dominant mechanism. Could it be the case that the structures we observe represent the equilibrium structures at this size? Looking at the proportions of the structural isomers this seems unlikely; the relative proportion of fcc decreases with size and the proportion of Dh and Ih increases with size. This is completely contradictory to

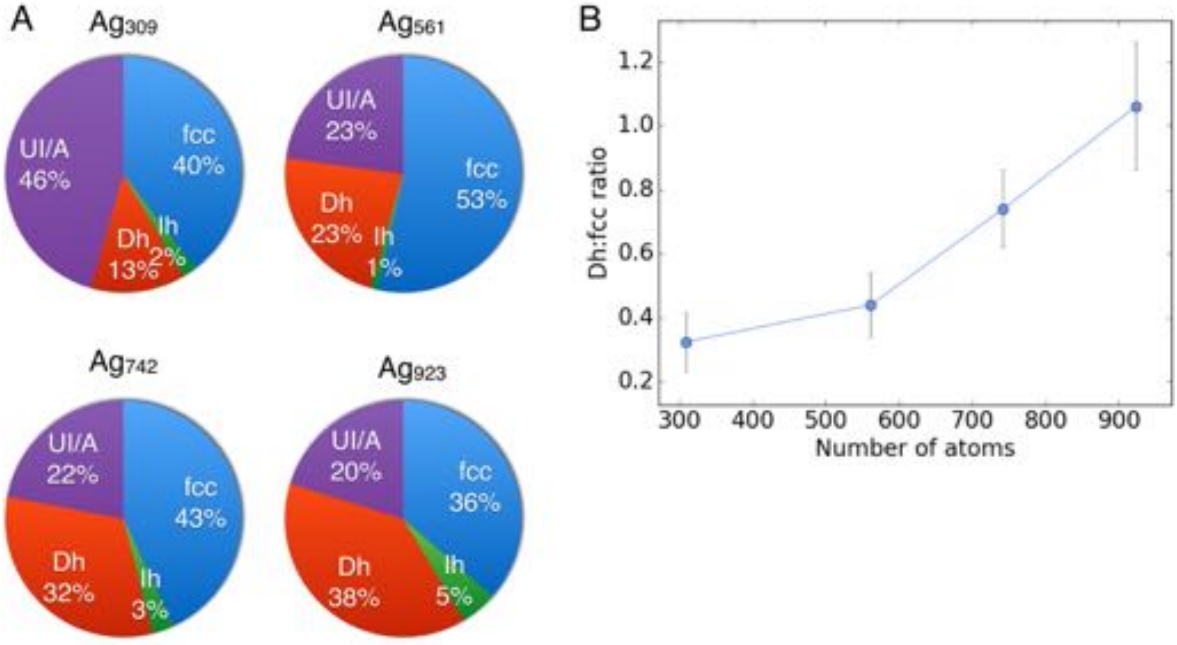

Figure 6.2: a) The proportion of structural isomers observed for size-selected Ag clusters containing 309, 561, 742 and 923 atoms. b) A schematic plot of the Dh:fcc ratio versus cluster size. The error on the Df:fcc ratio is indicated.

the generally accepted trend of Ih→Dh→fcc with increasing size [6, 7, 8]. A more likely explanation is an alternative growth mechanism resulting in kinetic trapping of Dh and Ih at larger sizes.

The observation of large metastable Ih produced from gas aggregation sources is well documented [9, 10, 11]. The presence of these metastable structures is explained by kinetic trapping, largely dependent on the temperature of formation. Reinhard et al reported that increasing the evaporation temperature in a gas aggregation source results in fewer large Ih and more fcc structures - indicating that fcc is the equilibrium structure and that the Ih are formed due to kinetic effects [9]. Molecular dynamics simulations of the growth of Ag clusters also show the formation of large metastable Dh and Ih during growth; not only by seed growth (as is reported for Au) but also by solid-solid transitions during growth [12]. Solid-solid transitions describe a growth mechanism whereby the atomic structure of a solid cluster changes during growth, often leading to the formation of metastable structures. For results presented here it seems likely that this alternative growth mechanism, whereby

metastable structure are formed through solid-solid transitions during growth, is resulting in the increase of Dh and Ih at larger sizes.

6.2 Ageing: the Effect of Air Exposure on Size-Selected Ag Clusters

In this section the effect of different durations of air exposure (from 20 mins to 24 days) on the atomic structure and chemical composition of Ag clusters is investigated by HAADF STEM and STEM EELS. Unlike the Au clusters described in chapters 3-5, Ag clusters are not stable in air. It is shown here that both atomic structure and chemical composition evolve with increased air exposure time.

6.2.1 Results on the Atomic Structure of (Initially) Size-Selected Ag Clusters After Exposure to Air

Figure 6.3 shows experimental images of Ag_{923} clusters that have been exposed to air for 10 days and the corresponding simulation atlas images. a,d) shows a cubotahedron, b,e) an ino-decahedron and c,f) and icosahedron. In the experimental images a core-shell type structure can been seen, in which the core has an ordered structure and the shell appears amorphous. This is characteristic of many of the air exposed clusters, with the proportion of core shell structures increasing with increased air exposure.

In the air exposed clusters another structural type was commonly observed - a partial icosahedron. These clusters contain certain features characteristic of the icosahedron, such as the 'ring-dot', but do not match directly to the atlas for the icosahedron. Figure 6.4 shows experimental images of the partial Ih structures and examples of the ring-dot motif commonly observed in the icosahedron simulation atlas. Figure 6.4A shows shows two examples of partial Ih structures in Ag_{923} clusters exposed to air for 10 days; in both cases there appears to be an off-centre icosahedron core - a feature that is present in many of these structures. The right

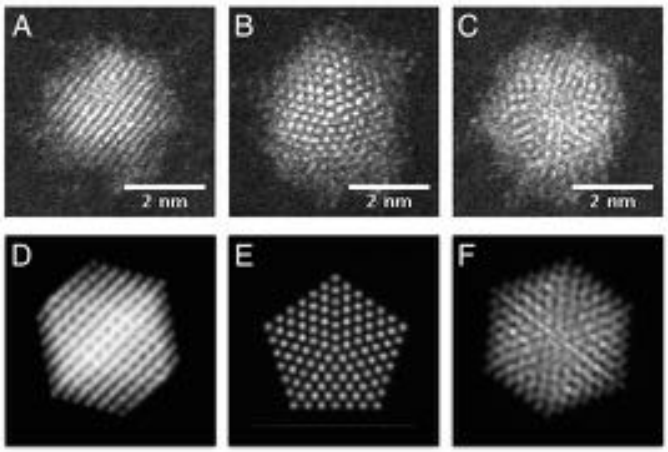

Figure 6.3: a-c) Typical HAADF STEM images of size-selected Ag_{923} clusters exposed to air for 10 days. d-f) simulation atlas images matched to the core atomic structure of the air exposed Ag_{923} clusters.

hand side cluster appears to be a 'half-icosahedron', a structure that seems unlikely to be stable for a pure Ag cluster. Figure 6.4B shows a further two examples of partial Ih structures in Ag_{561} clusters (exposed to air for 4 days); the left-hand side particle contains several ring-dot features and the right-hand side particle seems to have an off-axis Ih core.

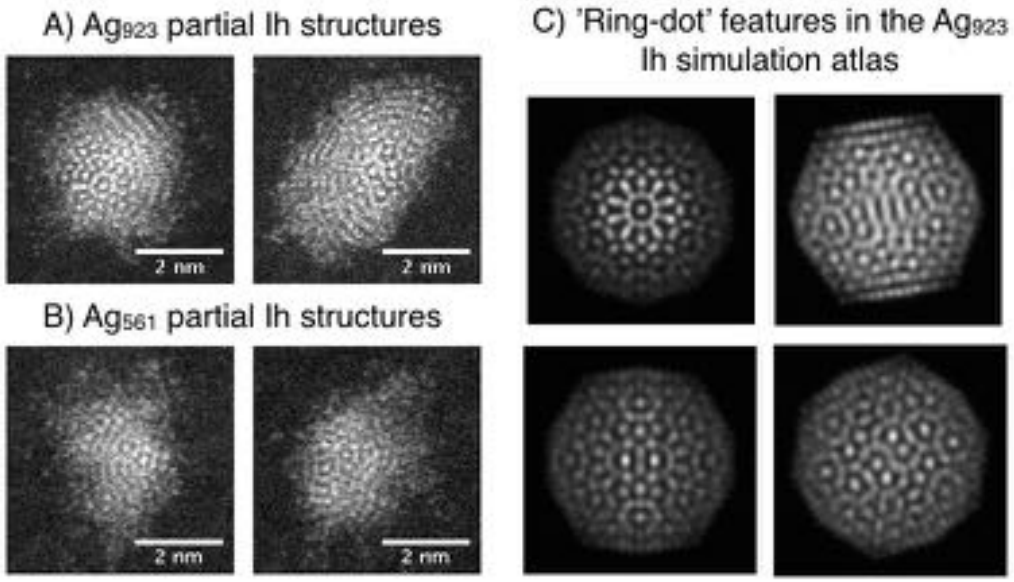

Figure 6.4: a) Example HAADF STEM images of partial icosahedra structures in Ag_{923} clusters exposed to air for 10 days. b) Example HAADF STEM images of partial icosahedra structures in Ag_{561} clusters exposed to air for 4 days. c) Examples of 'ring-dot' features in the Ag_{923} simulation atlas.

In figure 6.5 the proportion of structural isomers before and after exposure to air is presented. As before, structures are classified generally as fcc, Dh and Ih. This 'core-structure' analysis is particularly important when analysing the air exposed clusters due the formation of a disordered shell around the cluster. It is the core structure that is being used to identify the atomic structure. The partial Ih structures discussed above are grouped with the Ih for the purpose of the structural analysis. The general trend observed in all cases is an increase in Ih and p-Ih structures upon exposure to air. Figure 6.5A shows results for Ag_{561} after transfer

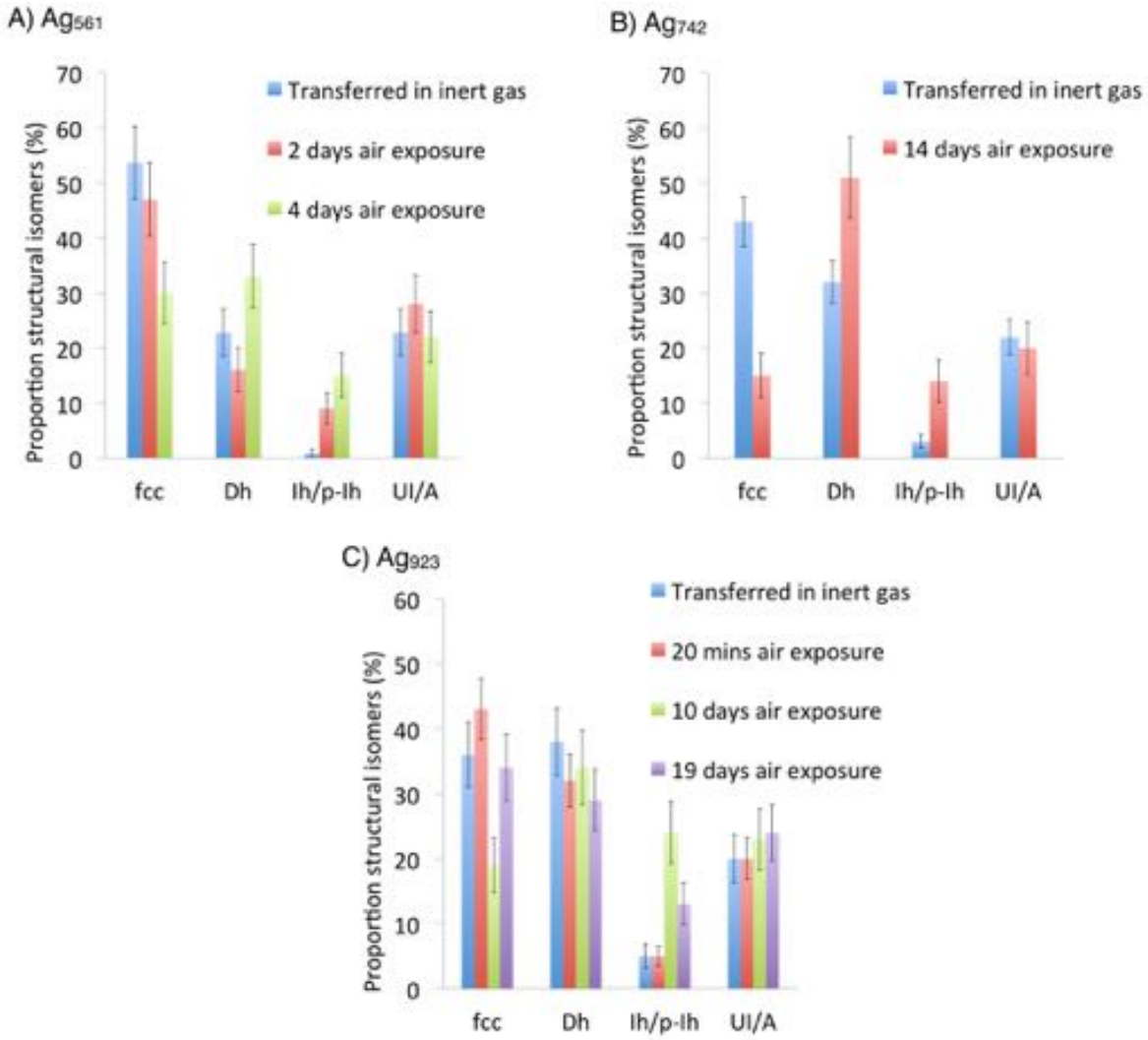

Figure 6.5: The proportion of structural isomers in size-selected Ag samples after exposure to air for varying amounts of time. Structures are classified as face-centred cubic (fcc), decahedral (Dh), Icosahedral/ partial-icosahedral (Ih/p-Ih), or unidentified/amorphous (UI/A). a) Ag_{561}, b) Ag_{742}, c) Ag_{923}.

in inert gas, exposure to air for 2 days and exposure to air for 4 days. The proportion of fcc gradually decreases with increased air exposure and the proportion of Ih/partial Ih increases. Figure 6.5B shows results of Ag_{742} after transfer in inert gas and after 14 days air exposure. The proportion of fcc decreases and the proportion of Dh and Ih/partial-Ih increases. Figure 6.5C shows results for Ag_{923} after transfer in inert gas, 20 minutes air exposure, 10 days air exposure and 19 days air exposure. Up to 10 days air exposure there is a decrease in fcc and and increase in Ih/partial Ih, at 19 days there is a slight increase in fcc and a decrease in Ih/partial Ih.

After air exposure there were also a number of clusters which displayed no atomic structure and appeared to be broken up to some degree - 'shell only' clusters. Figure 6.6 shows several examples of these 'shell only' clusters. In the structural analysis these clusters were classified as UI/A. For Ag_{561}, after 2 days air exposure 5% of the UI/A structures consist of 'shell only' clusters, and 7% after 4 days. For Ag_{742}, after exposure to air for 2 weeks there are no 'shell only' clusters. For Ag_{932}, after 20 minutes air exposure and 10 days exposure to air there are no 'shell only' clusters, but after 19 days air exposure 18% of the UI/A structures are formed of 'shell only' clusters. If the 'shell only' cluster form from Ih and p-Ih structures, it could explain why there is a decrease in Ih/p-Ih for Ag_{923} after 19 days air exposure.

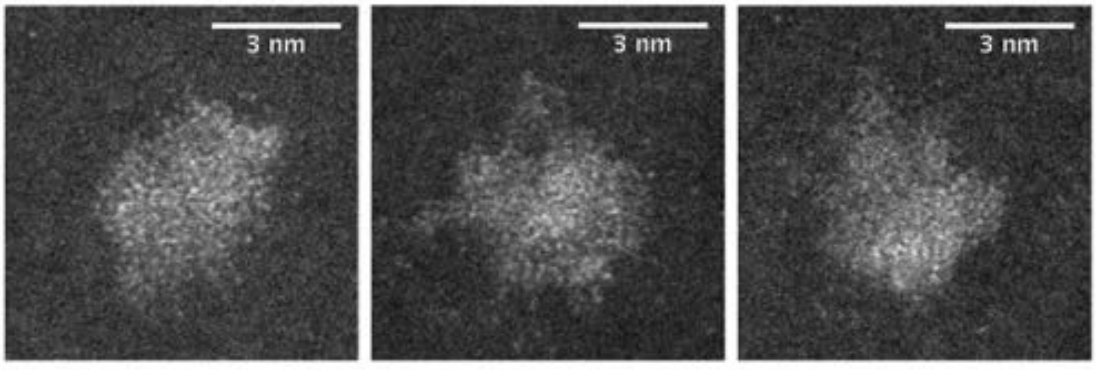

Figure 6.6: Examples of 'shell only' clusters in Ag_{923} clusters exposed to air for 19 days.

From the data presented in this section it can be seen that exposure of Ag clusters to air results in a significant structural change. It is known that silver corrodes in

air; the black tarnish formed on silverware after longterm air exposure is a result of the formation of silver sulphide [13]. As well as silver sulphide there are several other possible products of silver corrosion; namely silver sulphate and silver oxide [14, 15]. Therefore, it is possible that the core shell structures formed here and the change in atomic structure are a result of the formation of silver sulphide, silver sulphate, silver oxide or some combination of these.

6.2.2 Results on the Chemical Composition of (initially) Size-Selected Ag Clusters after Exposure to Air

To further understand the origin of the structural changes the Ag clusters undergo upon exposure to air, the chemical composition of the clusters must be studied after air exposure. Chemical analysis should confirm if the structural changes are due to formation of an oxide, sulphide, sulphate or some other compound. Based on the literature of silver corrosion, a silver-sulphur compound of some type is expected [14, 15, 16, 17, 18, 19], either Ag_2S or Ag_2SO_4.

To study the chemical composition after air exposure, size-selected Ag_{2057} clusters were produced (as before) and STEM-EELS measurements performed before and after air exposure. A larger cluster size (2057 atoms) was chosen so that the clusters did not break apart due to prolonged e-beam exposure during STEM-EELS acquisitions. This is particularly important for EELS mapping, where clusters are exposed to the beam for much longer periods of time (10-15 minutes). EELS point spectra measurements were performed after transfer of samples in inert gas from the cluster source, and on the same sample after 24 days air exposure.

Figure 6.7A shows an EELS point spectra for a Ag_{2057} particle. A HAADF STEM image of the particle is inset. There is a small sulphur L-edge signal (165eV), and a silver M-edge signal (367eV). The peak at 284eV is the carbon-edge from the amorphous carbon substrate. No oxygen K-edge (532eV) is present, as can be seen from the spectra. The Ag M-edge has a delayed maximum feature and has been identified with reference to EELS atlas data from Gatan's website [20].

Figure 6.7B shows a point EELS spectra of the amorphous carbon background, for comparison with figure 6.7A. A small sulphur signal, carbon signal and small Ag signal are visible, no oxygen signal is present. In addition there is a peak onset at approximately 650eV. This is thought to be due to manganese contamination (L_3 640eV, L_2 651eV) on the substrate and it is not present in any of the EELS spectra of clusters.

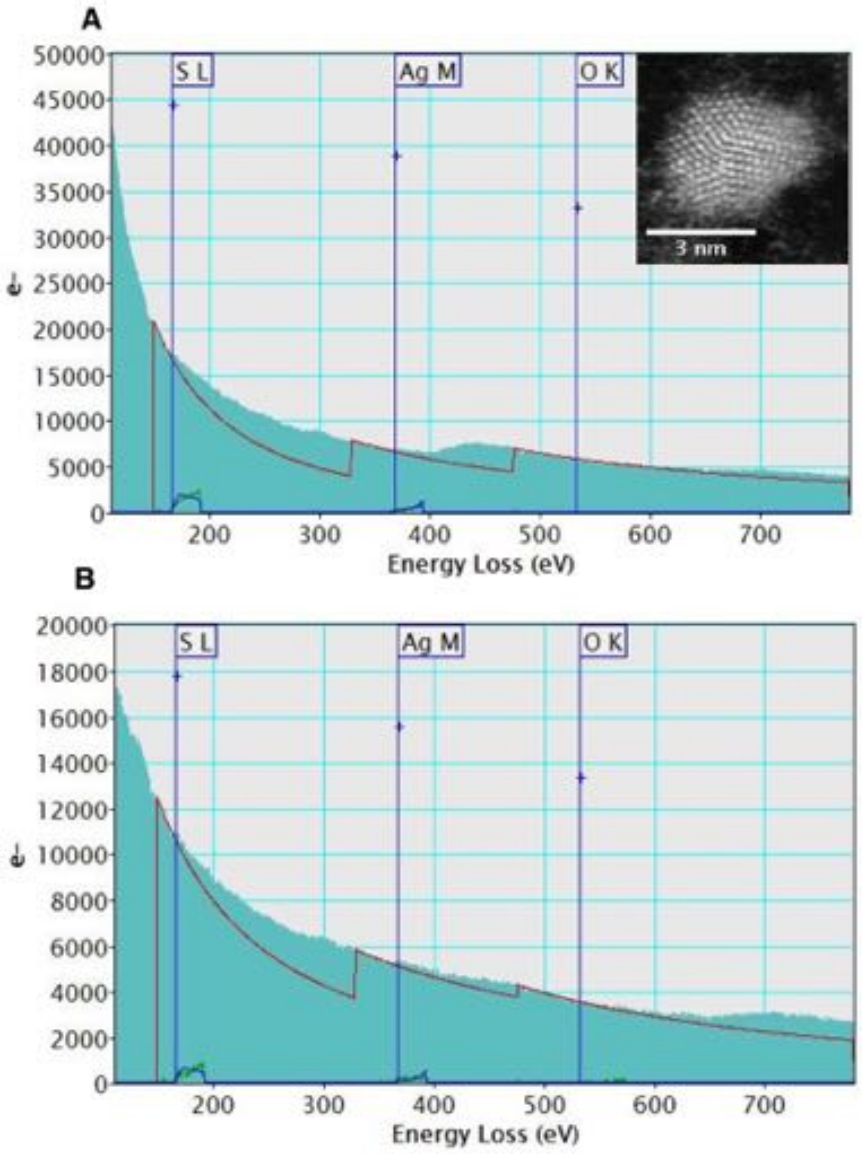

Figure 6.7: a) A point EELS spectra taken of a Ag_{2057} cluster (HAADF image inset) after transfer in inert gas. b) A point EELS spectra of the amorphous carbon substrate. In both cases the positions of the S L-edge, Ag M-edge and O-K edge are indicated. The red lines show the background subtraction and the green show the signal extracted after background subtraction.

There are two possible reasons for the presence of sulphur in the Ag clusters. The first is that during the inert gas transfer process, there is a short exposure to air ($\approx$ 5 seconds). Depending on the level of sulphur present in the air, it is possible that this is the source of the sulphur. However, due to the very short exposure time and the low level on sulphur present in the atmosphere, this seems unlikely; it has been shown that for a thin film of silver it takes approximately 1 hour for a 1 Å silver sulphide film to form [21]. It is also noted that, in the clusters produced here, there is what appears to be the start of a shell formation which was not seen for the samples in section 6.1. Another possibility is sulphur contamination in the cluster source deposition chamber, which was not present when the samples studied in section 6.1 were produced. Finally, the TEM grids themselves may contain a source of sulphur.

Figure 6.8 shows an example of an EELS spectrum taken in the shell of an Ag_{2057} cluster exposed to air for 24 days. In this case the position of sulphur, carbon (substrate material), silver and oxygen edges are indicated and the background subtraction is shown so that it is clear if these edges exist in the spectrum. One can see that sulphur, carbon and silver edges are present whilst there is no signal for oxygen. This was the case for all spectra recorded (exposed to air and transferred in inert gas).

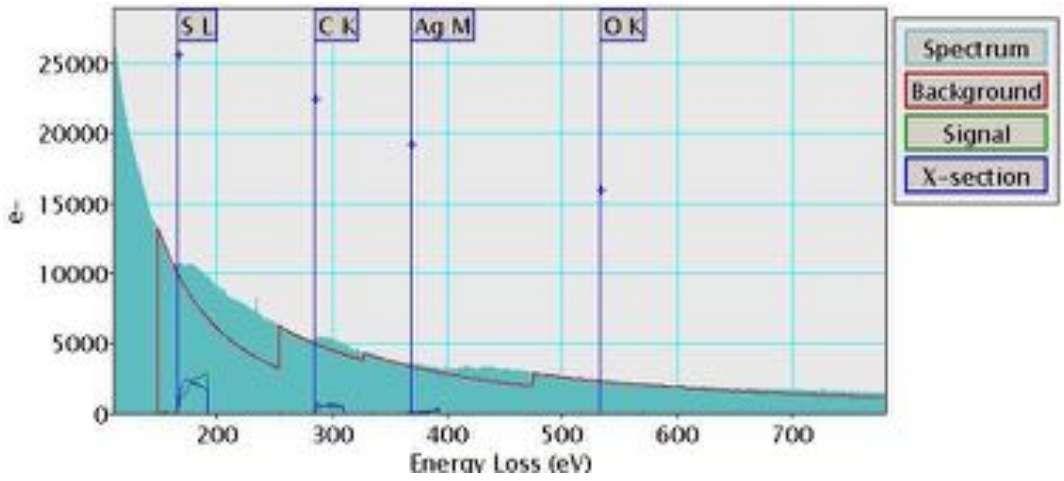

Figure 6.8: A point EELS spectrum the shell of a silver cluster exposed to air for 24 days. The background subtraction for sulphur, carbon, silver and oxygen edges is shown to indicate which elements are present.

Figure 6.9 shows two EELS point spectra taken of a Ag cluster after 24 days exposure to air. Figure 6.9A shows a HAADF STEM image of the cluster with the locations of the two point spectra acquisition points labelled. Figure 6.9B shows a point spectra taken in the core of the cluster (location 1) and C shows a point spectra taken in the shell of the particle (location 2). It should be noted that the point spectra acquired at location 1 also transverses the shell surrounding the core. In both cases silver M-edge and sulphur L-edge signals are present. However, the sulphur signal is much more prominent in the shell of the cluster than in the core. No oxygen K-edge signal is detected. This indicates that the core shell structure is formed of a Ag core and Ag_xS_x shell.

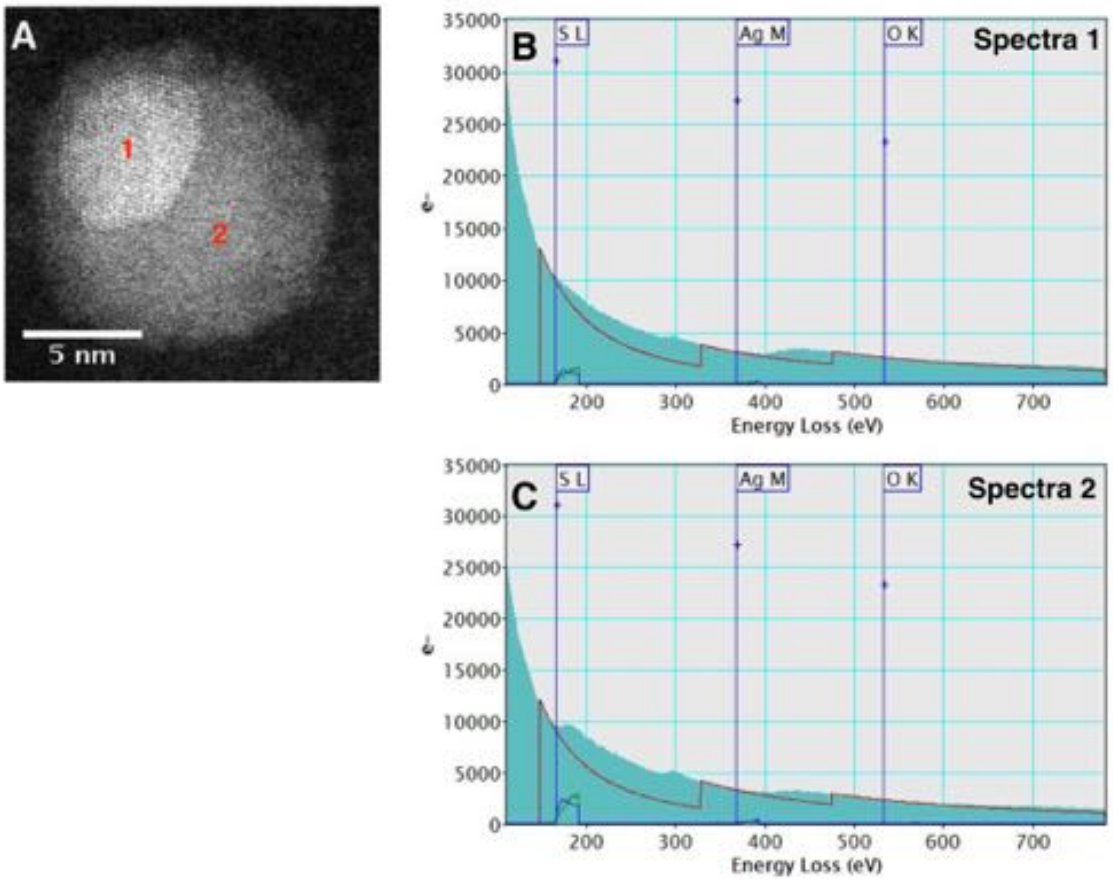

Figure 6.9: Point EELS spectra of a silver cluster exposed to air for 24 days. A) A HAADF STEM image of an Ag cluster after 24 days air exposure, the locations of two point EELS spectra acquisitions are indicated. B) A point EELS spectra taken at location 1, the cluster core. C) A point EELS spectra taken at location 2, the cluster shell.

Table 6.1 shows the ratio of the silver M-edge to the sulphur L-edge signal after inert gas transfer, and after 24 days air exposure. Respectively comparing the ratio before and after air exposure reveals the change in the sulphur content of the particles. For the sample transferred in inert gas, the core value represents measurements made of the Ag clusters, as they do not possess a core-shell structure. For the sample exposed to air for 24 days, core shell structures were formed and so the silver to sulphur ratio is shown for both the core and the shell (note that the core value also includes a contribution from the shell either side of the core). In the case of the inert gas transferred sample, the value given is an average over the value from 9 point spectra. For the sample exposed to air, the value for the core ratio is an average over 9 point spectra acquired from cluster cores and the shell value is an average over 8 point spectra acquired from cluster shells. The error on each individual quantified value is ≈10%, as calculated by the digital micrograph software and is largely composed of the error on the calculated partial scattering cross section (calculated using the Hartree-Slater model). The error shown in table 6.1 is the standard deviation of the data.

Table 6.1: Sulphur L-edge to Silver M-edge ratio before and after air exposure

	Inert gas transfer	24 days air exposure
Core	0.14±0.03	0.20±0.06
Shell	-	0.27±0.07

Overall, the results in table 6.1 show that there is an increase in the sulphur content of the clusters upon exposure to air (assuming the Ag content is constant). For the clusters exposed to air for 24 days there is a higher proportion of Ag in the core than in the shell. This supports the idea that upon exposure to air, an Ag-core, Ag_xS_x-shell structure is formed.

To further investigate the distribution of Ag and S in the clusters, several EELS maps of the air-exposed clusters were recorded. Figures 6.10 and 6.11 show EELS

maps of Ag, S and O for two different clusters. HAADF STEM images of the clusters before and after the mapping are also shown; it can be seen that in both cases the prolonged exposure to the electron beam damages the clusters, causing changes to the core and shell shapes.

The EELS mapping reveals that the Ag is concentrated in the core of the clusters. For the sulphur, there is a more even distribution over the cluster, with only slightly more present in the core. As before, no oxygen is detected in the particle. The fact that the sulphur signal is slightly more concentrated in the core of the clusters indicates that either sulphur has penetrated the core of the cluster to some extent or that the shell is thicker in this region.

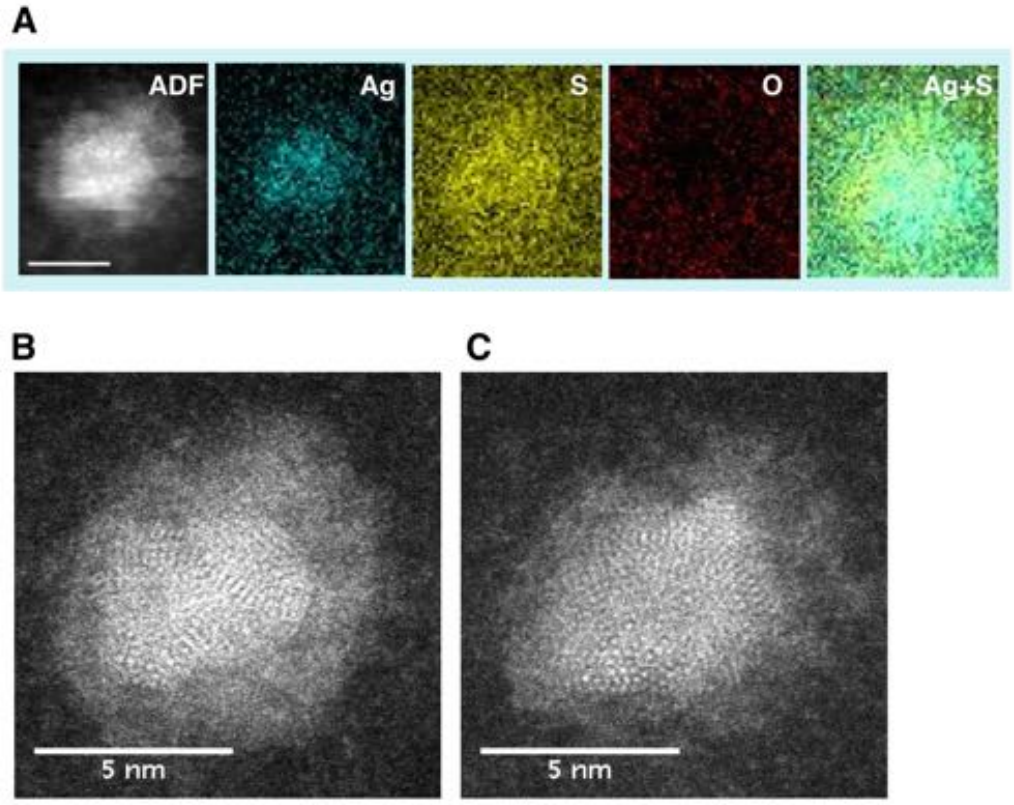

Figure 6.10: a) An EELS map of an Ag cluster exposed to air for 24 days. From left to right: HAADF STEM image of the mapped area, silver signal, sulphur signal, oxygen signal and combined sulphur and silver signals. b) A HAADF STEM image of the cluster mapped in a) before the mapping was performed. c) A HAADF STEM image of the cluster mapped in a) after the mapping was performed.

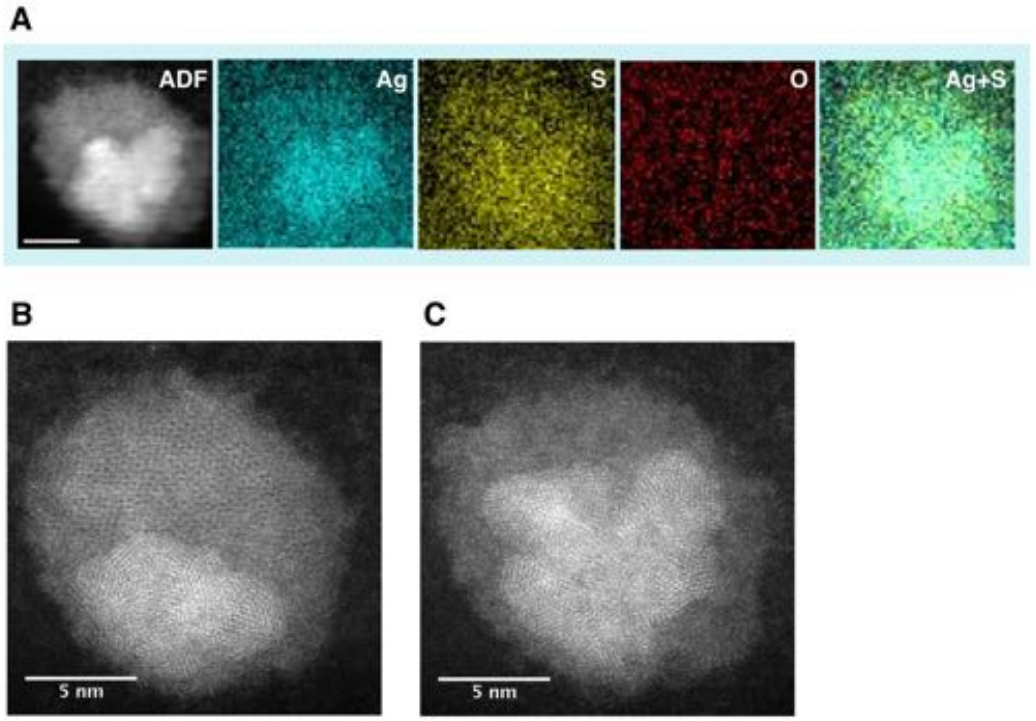

Figure 6.11: a) An EELS map of an Ag cluster exposed to air for 24 days. From left to right: HAADF STEM image of the mapped area, silver signal, sulphur signal, oxygen signal and combined sulphur and silver signals. b) A HAADF STEM image of the cluster mapped in a) before the mapping was performed. c) A HAADF STEM image of the cluster mapped in a) after the mapping was performed.

6.2.3 Discussion

The corrosion of silver has been the subject of many experimental studies due to its relevance to degredation in electronic systems [22]. Ag_2S is reported to be the main product of corrosion [14, 15, 16, 18, 19]. When exposed to air, several sulphur containing species have been identified as causing corrosion: H_2S, OCS, SO_2 and CS_2. H_2S and OCS are thought to be the main species responsible [16]. In the case of H_2S the reaction is reported to be either direct:

$$2Ag + H_2S \rightarrow Ag_2S + H_2. \tag{6.1}$$

or involving oxygen:

$$2Ag + H_2S + \frac{1}{2}O_2 \rightarrow Ag_2S + H_2O. \tag{6.2}$$

The humidity level (and oxygen level) has also been shown to enhance the sulphidation of silver because it allows the atmospheric gases to be dissolved at the surface of the metal [17, 19]. Water also enables the production of more H_2S from OCS by:

$$OCS + H_2O \rightarrow H_2S + CO_2. \tag{6.3}$$

Another species that has been found to be involved in the corrosion of Ag in air is NO_2. A combination of NO_2 and H_2S can lead to the formation of Ag_2S by:

$$2Ag + H_2S + 2NO_2 \rightarrow Ag_2S + 2HNO_2. \tag{6.4}$$

If NO_2 is present in air, this corrosion pathway is dominant [18]. Several other products of atmospheric silver corrosion have been reported [14, 15, 19], including Ag_2O, AgCl (in high chloride environments), $AgNO_3$ and Ag_2SO_4. However, the main species produced is expected to be Ag_2S.

The STEM EELS results presented in section 6.2.2 show that after air exposure, the clusters consist of silver and sulphur. This is in agreement with the literature on silver corrosion which states that silver sulphide is the main product of atmospheric silver corrosion. The ratio of suphur to silver for the shell of the air exposed clusters is 0.27, indicating that the shell has not completely sulphidised to form Ag_2S, for which a value of 0.50 would be expected. This could explain why many of the shell structures observed are amorphous rather than crystalline (acanthite, monoclinic), as would be expected for Ag_2S at room temperature.

The results of section 6.2.1 showed that exposure of Ag clusters to air results in a distinct structural change, namely there was a significant increase in the proportion of Ih and p-Ih structures after air exposure (see fig 6.5). In section 6.2.2 it was

found that upon air exposure, Ag clusters form a Ag core, Ag_xS_x shell. There are two possible mechanisms by which the formation of a core shell structure may lead to an increase in Ih structures. The first is by the reduction of the Ag core size as the shell thickness increases; at a smaller core size it is possible that the Ih is a stable structure (it is expected that the Ih is a stable structure at small sizes). However, the size of the cores formed in all cases are larger than an Ag_{309} cluster for which only 2% of structures were determined to be Ih (see results of section 6.1, fig6.2). This indicates that a reduction in core size is unlikely the reason for an increased proportion of Ih structures. Furthermore, this does not explain why many of the structures are partial Ih with off-centre cores.

The second explanation is that the formation of Ag-S bonds reduces the internal strain of the Ih structure. For Ag-Cu and Ag-Ni bimetallic core-shell particles it has been reported [23] that the polyicosahedral structure, consisting of several interlocking 13-atom Ih, is particularly stable. Generally, for pure clusters the structure is highly unstable (especially at larger sizes), due to the high internal strain caused by compressed nearest-neighbour distances. However, in the case of the core shell alloy clusters, the introduction of smaller sized atoms into the core affords optimal nearest-neighbour distances, resulting in a thermodynamically stable structure with low internal strain [23]. For the results presented here, it is possible that the formation of Ag-S bonds at the surface of the Ag cluster results in the nucleation of a polyicosahedral structure at the surface. The smaller sized sulphur atoms lowering the internal strain of Ih-like structures. This formation mechanism could explain the high proportion of clusters presenting local Ih features and also the observation of off-centre Ih cores.

6.3 Summary

The atomic structure of size-selected silver clusters containing 309, 561, 742 and 923 atoms has been investigated by HAADF STEM. In contradiction to the generally accepted stability of fcc at larger sizes, it was found that the Dh:fcc ratio increases

with size. It is suggested that kinetic trapping through solid-solid transitions during growth is responsible for the increase in Dh (and Ih) with size. By comparison, it was shown in chapter 3 that Au clusters produced under the same growth conditions, grow by template growth on small stable seed structures, with no solid-solid structural transitions. This result highlights the difference between growth mechanisms of Ag and Au clusters in gas aggregation sources.

The effect of air exposure on the atomic structure and chemical composition was studied by HAADF STEM and STEM-EELS. It was found that increased air exposure results in the formation of core shell clusters and an increase of Ih and partial-Ih structures. STEM-EELS measurements revealed that upon exposure to air, an Ag_xS_x shell is formed. Hence it is deduced that the increase in Ih/ partial-Ih is related to the formation of Ag-S bonds at the surface of the cluster. It is suggested that Ag-S bond formation may locally reduce the internal strain of the Ih structure; similarly to the case of bimetallic clusters in which the introduction of smaller sized atoms in the cluster core has been reported to reduce the internal strain of polyicosahedral structures.

References

[1] S Pratontep, S J Carroll, C Xirouchaki, M Streun, and R E Palmer. Size-selected cluster beam source based on radio frequency magnetron plasma sputtering and gas condensation. *Review of Scientific Instruments*, 76(4):045103, 2005.

[2] B von Issendorff and R E Palmer. A new high transmission infinite range mass selector for cluster and nanoparticle beams. *Review of Scientific Instruments*, 70(12):4497, 1999.

[3] S J Carroll, S Pratontep, M Streun, R E Palmer, S Hobday, and R Smith. Pinning of size-selected Ag clusters on graphite surfaces. *The Journal of Chemical Physics*, 113(18):7723, 2000.

[4] Z W Wang and R E Palmer. Determination of the ground-state atomic structures of size-selected Au nanoclusters by electron-beam-induced transformation. *Physical Review Letters*, 108(24):245502, 2012.

[5] C Koch. *Determination of core structure periodicity and point defect density along dislocations*. PhD thesis, Arizona State University, 2002.

[6] F Baletto, R Ferrando, A Fortunelli, F Montalenti, and C Mottet. Crossover among structural motifs in transition and noble-metal clusters. *The Journal of Chemical Physics*, 116(9):3856–3863, 2002.

[7] B Wang, M Liu, Y Wang, and X Chen. Structures and energetics of silver and gold nanoparticles. *The Journal of Physical Chemistry C*, 115(23):11374–11381, 2011.

[8] A M Angulo and C Noguez. Atomic structure of small and intermediate-size silver nanoclusters. *Journal of Physical Chemistry A*, 112:5834–5838, 2008.

[9] D Reinhard, B D Hall, D Ugarte, and R Monot. Size-independent fcc-to-icosahedral structural transition in unsupported silver clusters: An electron diffraction study of clusters produced by inert-gas aggregation. *Physical Review B*, 55(12):7868–7881, 1997.

[10] I Barke, H Hartmann, D Rupp, L Flückiger, M Sauppe, M Adolph, S Schorb, C Bostedt, R Treusch, C Peltz, S Bartling, T Fennel, K-H Meiwes-Broer, and T Möller. The 3D-architecture of individual free silver nanoparticles captured by X-ray scattering. *Nature Communications*, 6:6187, 2015.

[11] M A Gracia-pinilla, D Ferrer, S Mejia-Rosales, and E Perez-Tijerina. Size-selected Ag nanoparticles with five-fold symmetry. *Nano Express*, 4:896–902, 2009.

[12] F Baletto, C Mottet, and R Ferrando. Microscopic mechanisms of the growth of metastable silver icosahedra. *Physical Review B*, 63(15):155408, 2001.

[13] Birmingham Assay Office. Tarnishing.

[14] H Kim. Corrosion process of silver in environments containing 0.1 ppm H_2S and 1.2 ppm NO_2. *Materials and Corrosion*, 54(4):243–250, 2003.

[15] H Lin, G S Frankel, and W H Abbott. Analysis of Ag corrosion products. *Journal of the Electrochemical Society*, 160(8):C345–C355, 2013.

[16] J L Elechiguerra, L Larios-lopez, C Liu, D Garcia-gutierrez, A Camacho-bragado, and M J Yacaman. Corrosion at the nanoscale: the case of silver nanowires and nanoparticles. *Chemistry of Materials*, 17:6042–6052, 2005.

[17] Ch Kleber, R Wiesinger, J Schnöller, U Hilfrich, H Hutter, and M Schreiner. Initial oxidation of silver surfaces by S^{2-} and S^{4+} species. *Corrosion Science*, 50(4):1112–1121, 2008.

[18] L Volpe and P J Peterson. The atmospheric sulfidation of silver in a tubular corrosion reactor. *Corrosion Science*, 29(10):1179–1196, 1989.

[19] T E Graedel. Corrosion mechanisms for silver exposed to the atmosphere. *Advancing Solid State and Electrochemical Science and Technology*, 139(7):1963–1970, 1992.

[20] Gatan. EELS Atlas.

[21] H E Bennet, R L Peck, D K Burge, and J M Bennet. Formation and growth of tarnish on evaporated silver films. *Journal of Applied Physics*, 40(8):3351–3360, 1969.

[22] B Valdez Salas, M Schorr, G Lopez, M Carrillo, R Zlatev, M Stoycheva, J D Ocampo Diaz, L Vargas, and J Terrazas. H_2S pollution and its effect on corrosion of electronic components. In *Air Quality - New Perspective*, pages 263–286. 2012.

[23] G Rossi, A Rapallo, C Mottet, A Fortunelli, F Baletto, and R Ferrando. Magic polyicosahedral core-shell clusters. *Physical Review Letters*, 93(10):1–4, 2004.

Chapter 7

Conclusions and Outlook

In this thesis, aberration corrected HAADF STEM has been used to examine the atomic structure of size-selected Au and Ag nanoclusters produced by a magnetron sputtering gas aggregation cluster beam source. In this chapter, the major conclusions resulting from the work are summarised and prospective future studies considered.

7.1 Template Growth in Au Clusters

In the first part of chapter 3, the gas phase growth of Au clusters between 561 and 923 atoms was investigated. It was found that the proportion of structural isomers are essentially identical for sizes 561, 742 and 923 (produced under identical conditions). Electron beam manipulation experiments also revealed that the most abundant Dh structure is metastable, converting to fcc under electron beam irradiation, whilst fcc isomers are stable. It was concluded that Au clusters grow by template growth on smaller seed structures, resulting in kinetic trapping of metastable structures. This conclusion was supported by molecular dynamics simulations of cluster growth (performed by G. Rossi and R. Ferrando), which show that no solid-solid structural transitions occur during the growth of Au clusters within this size range.

7.2 Atomic Structure Control of Au_{309} Clusters

In the second part of chapter 3, atomic structure control of Au_{309} clusters was demonstrated. It was shown that decreasing the condensation length (effective growth time) results in a significant increase in the proportion of fcc isomers, and a decrease in Ih and UI/A isomers. To better understand the control mechanism, electron beam manipulation experiments were performed. It was found that the relative order of stability for Au_{309} is fcc→Dh→Ih. Based on these findings, two possible mechanisms for the atomic structure control were proposed. The first is that the higher average temperature associated with shorter condensation lengths results in a more equilibrated system (i.e. more fcc). The second explanation is that a coalescence growth mechanism becomes dominant at longer condensation lengths, resulting in more UI/A structures and fewer fcc structures. It should be noted that the control mechanism at this size is different from that previously reported at size 923.

Control of atomic structure, such as that presented here, opens up the possibility to study other properties as a function of atomic structure. In particular, it would be interesting to correlate the catalytic activity of Au clusters with their atomic structure. To better understand the control mechanism, further studies could be performed to investigate the effect of the temperature of the condensation zone during growth and a wider range of condensation lengths could be studied. Ultimately, this could lead to the production of single isomer samples.

7.3 Experimental Determination of the Energy Difference Between Isomers

In chapter 4, a heating stage was used to perform in-situ heating experiments on size-selected clusters in the ac-STEM. The proportion of structural isomers for Au_{561} was determined for a range of temperatures, and two distinct regions were identified. In the low temperature region (20°C-125°C) it was found that metastable Dh convert

to fcc structures, similarly to the electron beam manipulation experiments of chapter 3. In the high temperature region (125°C-500°C) it was found that the Dh isomer is repopulated. This is attributed to the higher thermal energy allowing 'excitation' of clusters to higher energy states (higher energy isomers), reflecting Boltzmann statistics.

Based on these observations, a method for determining the energy difference between isomers was presented and applied to the high temperature region of the data. The energy difference between Dh and fcc isomers (size 561), ΔE_{Dh-fcc}, was calculated to be 0.04±0.02 eV.

The method presented here allows for a quantitative comparison between theoretical and experimental studies, for the first time. In the future, this method could be applied to numerous cluster systems to experimentally map their potential energy surfaces. With further improvement to the structural identification from HAADF STEM (or by other methods), variations to the perfect Dh and fcc isomers could be accounted for, allowing a much more accurate understanding of the potential energy surface. Furthermore, in-situ STEM measurements could also be used to determine the barrier height between isomers by measurements of the transition rates between isomers at a range of temperatures.

7.4 Surface Melting in Au Clusters

In chapter 5, results on surface melting and melting point suppression in size-selected Au clusters on amorphous carbon were presented. In-situ heating in the ac-STEM allowed for direct, atomic resolution imaging of surface melting and elucidation of the melting mechanism. The formation of a solid-core liquid-shell structure was observed at high temperatures, with solid-liquid coexistence persisting over a range of temperatures. The data collected was compared with various melting models. It was found that results are in good qualitative agreement with the liquid nucleation and growth model. However, the core atomic structure persisted to much higher temperatures than predicted by this model (or Pawlow's triple point model and the

liquid shell model).

More generally, with precise control over cluster size and temperature, and atomic resolution imaging, size-selected clusters and ac-STEM are an ideal combination for determination of melting mechanisms at the nanoscale. In the future this combination could be applied to study nanoscale melting in a wide variety of (supported) materials. Ultimately, understanding of the surface structure in nanomaterials at high temperatures (and/or relevant reaction conditions) may be applied to future catalyst design.

7.5 The Atomic Structure and Ageing of Ag Clusters

In the first section of chapter 6, the proportion of structural isomers are determined for Ag clusters consisting of 309, 561, 742 and 923 atoms. In all cases clusters were produced with the same formation conditions. It was shown that there is a gradual increase in the Dh:fcc ratio with increasing size. This is attributed to kinetic trapping due to solid-solid transitions during growth. Conversely, in chapter 3 it was shown that Au clusters do not undergo solid-solid transitions during growth. This result is in agreement with growth simulations in the literature which show that Ag undergoes solid-solid transitions during growth resulting in trapping of metastable structures and Au does not. Both the experimental result, and the theory from literature, indicate a different growth mechanism for Au and Ag clusters in the gas phase.

In the second section of chapter 6, the effect of air exposure on atomic structure was investigated. For all sizes studied (561, 742 and 923), it was found that increased air exposure leads to and increase in the proportion of Ih and partial-Ih structures. Furthermore, prolonged exposure times resulted in core-shell structures in larger clusters and 'shell only' structures in smaller clusters. STEM-EELS measurements revealed that an Ag_xS_x shell is formed upon exposure to air. The correlation of the

Ag_xS_x shell formation with the increase in Ih/ partial-Ih structures was discussed and a potential mechanism for the structural change was suggested.

Ag nanoparticles are widely used as antibacterials so it is important to understand how they will evolve in the environment and to determine their toxicity. In the future it would be interesting to investigate how the toxicity of Ag nanoclusters evolves with increased exposure to air and to study the effects of longer term air exposure. Particle size and shape has been shown to have an effect on the uptake of nanoparticles by cells, a further extension would be to investigate the uptake of Ag nanoparticles as a function of both size and structure using size-selected clusters.

Appendix A

Calculation of the Electron Dose During STEM Imaging

The electron dose is calculated using the following equation:

$$\text{Electron dose}(e^{-}\text{Å}^{-2}\text{frame}^{-1}) = \frac{\text{Beam current } (A)\times\text{Frame time } (s)}{\text{Charge } e^{-}(C)\times\text{Frame area } (\text{Å}^{2})} \qquad \text{(A.1)}$$

The current in amps multiplied by the time in seconds gives the charge per frame in coulombs. Dividing by the charge of an electron and area of the frame gives the charge in terms of the number of electrons per unit of area.

An example dose calculation

Below are standard values used for 'video imaging' experiments performed in Chapter 3:

Beam Current density*=3.0 pA·cm^{-2}

Frame time=2.88s

Frame size=157.4Å×157.4Å

*The calibration of the fluorescent screen in the STEM requires that the current

density be multiplied by 10 (not by the area of the screen) to obtain the beam current.

The dose is then calculated by:

$$\text{Electron dose} = \frac{3.0\times10^{-12}\times10\times2.88}{1.602\times10^{-19}\times157.4\times157.4} = 21769e^{-}\text{Å}^{-2}\text{frame}^{-1}$$
$$\approx 2.2\times10^{4}e^{-}\text{Å}^{-2}\text{frame}^{-1} \quad \text{(A.2)}$$

Appendix B

Models of Melting Point Suppression

Below are the equations and constants used for plotting melting models in chapter 5.

Pawlow's triple point model

$$T_m = T_0 \left(1 - \frac{2V_s}{Lr}\left(\sigma_s - \sigma_l \left(\frac{\rho_s}{\rho_l}\right)^{2/3}\right)\right). \tag{B.1}$$

Equation from reference 1.

Liquid shell model

$$T_m = T_0 \left(1 - \frac{2V_s}{L}\left(\frac{\sigma_{sl}}{r-t} + \frac{\sigma_l}{r}\left(1 - \frac{\rho_s}{\rho_l}\right)\right)\right) \tag{B.2}$$

Equation from reference 1.

LNG model lower limit

$$T_m = T_0 \left(1 - \frac{3\sigma_{sl}V_s}{Lr}\right). \tag{B.3}$$

Equation from reference 2.

The upper limit is given by Pawlow's model, references 1 and 3.

LNG model critical radius

$$r_c = \frac{2\sigma_{sl} V_s T_0}{L(T_0 - T)}. \tag{B.4}$$

Equation from reference 3.

T_m=Melting temperature

T_0=Bulk melting temperature

V_s=Molar volume of the solid

L=Molar latent heat

r=Particle radius

σ_s=Surface tension of the solid

σ_l=Surface tension of the liquid

$\sigma_{sl} = \sigma_s - \sigma_l$

ρ_s=Mass density of the solid

ρ_l=Mass density of the liquid

t=Liquid shell thickness

r_c=Critical radius

Table B.1: Constants used for plotting the above models in chapter 5

Symbol	Value	Reference
T_0	1336 K	[1]
V_s	10.7109×10^{-6}m^3/mol	[3]
L	12362 J/mol	[1]
σ_s	1.4 J/m^2	[1]
σ_l	1.13 J/m^2	[1]
ρ_s	18400 kg/m^3	[1]
ρ_l	17280 kg/m^3	[1]

References

[1] Y G Chushak and L S Bartell. Melting and freezing of gold nanoclusters. *Journal of Physical Chemistry B*, 105:11605–11614, 2001.

[2] P R Couchman and W A Jesser. Thermodynamic theory of size dependence of melting temperature in metals. *Nature*, 269(5628):481–483, 1977.

[3] G Guenther and O Guillon. Models of size-dependent nanoparticle melting tested on gold. *Journal of Materials Science*, 49(23):7915–7932, 2014.